

**SHAPE CASTING HIGH STRENGTH Al-Zn-Mg-Cu ALLOYS: INTRODUCING
COMPOSITION-BEHAVIOR RELATIONSHIPS**

**SHAPE CASTING HIGH STRENGTH Al-Zn-Mg-Cu ALLOYS: INTRODUCING
COMPOSITION-BEHAVIOR RELATIONSHIPS**

BY ALI MAZAHERY, M. Sc.

A THESIS

SUBMITTED TO THE SCHOOL OF GRADUATE STUDIES

IN PARTIAL FULFILLMENT OF THE REQUIREMENTS

FOR THE DEGREE OF

MASTER OF SCIENCE

MCMASTER UNIVERSITY

© COPYRIGHT BY ALI MAZAHERY, JULY 2016

ALL RIGHT RESERVED

**McMaster University MASTER OF SCIENCE (2016) Hamilton, Ontario
(MECHANICAL ENGINEERING)**

**TITLE: SHAPE CASTING HIGH STRENGTH Al-Zn-Mg-Cu ALLOYS:
INTRODUCING COMPOSITION-BEHAVIOR RELATIONSHIPS, AUTHOR: Ali
Mazahery, M. Sc. (University of Tehran) SUPERVISORS: Professor Joey Kish,
Professor Joseph McDermid, Professor Sumanth Shankar NUMBER OF PAGES:
xiii, 123**

Abstract

High strength Al-Zn-Mg-Cu alloys have been increasingly employed in the transportation industry due to the increased demands for light structural components. However, their applications have been limited to relatively expensive wrought products. Application of the shape cast Al-Zn-Mg-Cu parts has never been the focus of attention due to their poor castability and mechanical properties. Improving the casting quality is expected to increase their utilization within the automotive industry. The poor castability and mechanical properties of some alloys in this family may be effectively improved through optimized chemistry control and melt treatment including grain refinement. The primary objective of this project is to optimize the chemistry and heat treatment of the Al-Zn-Mg-Cu alloy family that results in improved strength with acceptable level of ductility and casting quality relative to other shape cast Al alloys.

The Taguchi experimental design method was used to narrow down the number of required casting experiments required to meet the research objective. Three levels across four elements yielded a total of 9 Al-Zn-Mg-Cu alloys, which were cast using a tilt pour permanent mold process. The effect of each major alloying element on the microstructure, and mechanical properties was investigated. Tensile measurements were made on the 9 alloys subjected to two steps solution treatments. Mechanical properties such as yield strength (YS), ultimate tensile strength (UTS), and elongation at fracture (El.%) were experimentally measured and statistically analyzed.

An ANOVA analysis was employed to quantify the percentage contribution of the alloying elements on the material properties. Grain refinement was found to play a

significant role in improving the hot tearing resistance and, thereby ameliorating quality. The alloying element that affected the YS and UTS to the greatest extent was Cu, followed by Zn. In contrast, the effect of Mg and Ti on YS and UTS was insignificant. Moreover, a decrease in Mg content had the greatest effect in enhancing the El.%.

A regression analysis was used to obtain statistical relationships (models) correlating the material properties with the variations in the content of the major alloying elements. The R-square values of YS, UTS, and El.% were 99.7 %, 98 %, and 90 %, respectively, showing that the models replicated the experimental results. Verification measurements made on shape cast Al-6Zn-2Mg-2Cu alloy revealed that the material property model predictions were in agreement with the experimentally measured values.

The results show that secondary and over ageing treatments of the shape cast Al-Zn-Mg-Cu alloys lead to superior combination of YS and El.%. The ongoing advances in shape casting of Al-Zn-Mg-Cu alloys with high will make them suitable choices for commercial load-bearing automotive components, when it comes to the selection of a material meeting the minimum requirements for strength, damage tolerance, cost and weight.

Keywords: Al-Zn-Mg-Cu alloys, shape-casting, grain refinement, hot tearing, Taguchi design, tensile testing, ANOVA, regression

Table of contents

1	Introduction	1
2	Literature review	7
2.1	Microstructure of as-cast Al-Zn-Mg-Cu alloys	7
2.2	Solution treatment of Al-Zn-Mg-Cu alloys	9
2.3	Quench.....	17
2.4	Aging response of Al-Zn-Mg-Cu alloys.....	18
2.4.1	Natural aging response of Al-Zn-Mg-Cu alloys at room temperature.....	19
2.4.2	Artificial aging response of Al-Zn-Mg-Cu alloys	23
2.4.3	Artificial Aging response of Al-Zn-Mg-Cu alloys at 120 °C: Chemistry of precipitates	23
2.4.4	Artificial Aging response of Al-Zn-Mg-Cu alloys at 120 °C: Number density and size of precipitates.....	26
2.4.5	Strengthening mechanism in precipitation hardened Al-Zn-Mg-Cu alloys	27
2.4.6	Effect of temperature on the artificial aging response of Al-Zn-Mg-Cu alloys ..	29
2.4.7	Role of Cu in the artificial aging response of Al-Zn-Mg-Cu alloys.....	31
2.5	Design of experiment (DOE)	32
2.5.1	Factorial design	32
2.5.2	Taguchi method.....	33
2.5.3	Signal to noise ratio (S/N)	33
2.5.4	Performance of the Taguchi method to optimize the process parameters in research.....	34
3	Research hypothesis.....	37

4	Experimental procedure	39
4.1	Taguchi designed experiment	39
4.1.1	Materials	39
4.1.2	Casting process	40
4.1.3	Heat treatment	41
4.2	Characterization	42
4.2.1	Chemistry test and visual inspection	42
4.2.2	Solidification simulation	43
4.2.3	Light optical microscopy	43
4.2.4	Tensile test	44
4.3	Statistical analysis of Taguchi designed alloys properties	45
4.3.1	The S/N ratio	45
4.3.2	ANOVA and multiple regression	46
4.3.3	Verification of the models	46
4.4	Secondary aging (SA) of Al-Zn-Mg-Cu alloys	46
4.5	Artificial ageing (AA) of Al-Zn-Mg-Cu alloys	47
4.6	Camber link shape casting trial	48
5	Results and discussion	50
5.1	Characterization of the 9 Taguchi-designed Al-Zn-Mg-Cu alloys	50
5.1.1	Chemical composition	50
5.1.2	Visual inspection	51
5.1.3	As-cast microstructure	53
5.2	Statistical analysis of tensile properties	59
5.2.1	Main effect plots and percentage contribution	63
5.3	Study of Al-6Zn-2Mg-2Cu alloys	69

5.3.1	Shape casting a Camber link part using Al-6Zn-2Mg-2Cu alloys	79
6	Conclusion	81
7	Appendix A Visual inspection of castings	83
8	Appendix B Grain structure	92
9	Appendix C Thermal analysis	96
10	Appendix C Tensile properties of 9 alloys	102
11	Appendix D Tensile properties of validation alloys	111
12	References	114

List of Figures

<i>Figure 1-1 Schematic illustration of hot tearing. [1].....</i>	<i>2</i>
<i>Figure 1-2 Effect of grain refinement on grain structure and hot tearing susceptibility of A206: (a) Before grain refinement, (b) After grain refinement [2].....</i>	<i>3</i>
<i>Figure 1-3 Grain refined Al-6Zn-2.2Mg-2.2Cu: (a) OM of A type (5Ti-1B-remainder Al) added, (b) OM of B type (6Ti-remainder Al) added, (c) OM of C type (6Ti-remainder Al) added, (d) Hot crack lengths [4] ..</i>	<i>4</i>
<i>Figure 1-4 Length of crack in Al-6Zn-2.2Mg-2.2Cu as a function of Ti (wt.%) [4]</i>	<i>5</i>
<i>Figure 2-1 Microstructure of the as-cast Al-8.1Zn-2.05Mg-2.3Cu: (a) light optical microscopy image, (b) SEM image showing grain boundary decoration (spot A: Al₇Cu₂Fe; Spot B and C: T phase (Al₂Mg₃Zn₃)) [9]</i>	<i>9</i>
<i>Figure 2-2 Incipient melting of Al-Al₂Cu-Si particles during solution treatment at 525 °C, etched. Arrows indicated the regions where incipient melting has occurred [10].</i>	<i>11</i>
<i>Figure 2-3 Light optical micrographs of pores caused by incipient melting in a Al-Zn-Mg-Cu alloy [11].</i>	<i>12</i>
<i>Figure 2-4 Area fraction (%) of residual phase in AA7075 subjected to different solution treatments [14].....</i>	<i>14</i>
<i>Figure 2-5 Effect of solution treatment (homogenization) time on the volume fraction of particles in Al-4.37Zn-1.2Mg-0.19Cu alloys [17].....</i>	<i>15</i>
<i>Figure 2-6 Solvi of the S phase in Al-Zn-Mg-Cu alloys with Zn=6 wt% as a function of the alloy Cu content [6].</i>	<i>16</i>
<i>Figure 2-7 Formation of large precipitates in a slowly cooled Al-6.7Zn-2.6Mg-2.6Cu alloy. Alloy was solution at 480 °C for 24 h, and then slowly cooled. Needle-shape Zn-rich σ phase were formed [5].</i>	<i>18</i>
<i>Figure 2-8 Effect of natural aging time on the hardness of an Al-6Zn-2.2Mg-2.3Cu and Al-3.6-1.8Mg alloy: (a)early stages (48 h) and (b) later stages(480 h) [25].</i>	<i>21</i>
<i>Figure 2-9 Effect of natural aging time on the hardness of an Al-6.1Zn-2.3Mg-0.1Zr alloy after solution treatment followed by a water quench or an air quench [26].</i>	<i>22</i>
<i>Figure 2-10 DSC curves of a naturally-aged Al-6.1Zn-2.3Mg-0.1Zr alloy after solution treatment followed by a water quench or an air quench:(a) 0.5°C min⁻¹ and (b) 5°C min⁻¹ [26].....</i>	<i>22</i>

Figure 2-11 TEM image of Al-5.7Zn-2Mg-2Cu alloy after artificially aging for 15 min. at 130 °C [20]..... 24

Figure 2-12 Mg-Zn clusters formed in an Al-6.29Zn-2.2Mg-2.2Cu alloy artificially aged at 120 °C for different times up to 24 h.: (a) 30 min., (b) 1, (c) 4, (d) 8 and (e) 24 h [24]. 24

Figure 2-13 TEM image showing the nature of the precipitates that formed in an Al-6.29Zn-2.2Mg-2.2Cu alloy artificially aged at 120 °C for 24 h [24]. 25

Figure 2-14 Artificial aging response of an Al-6.29Zn-2.2Mg-2.2Cu alloy at 120 °C: (a) cluster density, (b) average cluster size, (c) maximum solute content in the matrix [24]..... 27

Figure 2-15 Schematic of precipitate hardening mechanisms: (a) shearing, (b) bowing, and (c) strengthening by small ($\sim\sqrt{r}$) and big ($\sim 1/r$) precipitates indicating transition from Friedel effect (particle shearing) to Orowan mechanism (bow-out between particles) at the critical particle radius []. 28

Figure 2-16 Artificially aging response of an Al-7.5Zn-2Mg-2Cu alloy: (a) hardness at both 120 °C and 160 °C, (b) electrical conductivity at both 120 °C and 160 °C [29]. 30

Figure 2-17 Artificial aging response of an Al-7.5Zn-2Mg-2Cu alloy: (a) tensile properties at 120 °C, (b) tensile properties at 160 °C [29]. 30

Figure 2-18 Artificial Aging response of an Al-6Zn-2.2Mg-2.3Cu and Al-3.6Zn-1.8Mg alloy [25]. 31

Figure 2-19 Main effect plots of S/N ratios showing the effects of each parameter level on: (a) microhardness, (b) electrical conductivity [31]. 36

Figure 4-1 Schematic representation of tilt-pour-casting process (a) pouring, (b) tilting, and (c) solidification position. 41

Figure 4-2 A typical permanent mould shape casting 42

Figure 4-3 Shape cast sample for composition analysis by GDOES. Red frame identifies location of sub-section extracted for the analysis. 43

Figure 4-4 Double step ageing response of Al-6Zn-2Mg-2Cu at 120 °C and 180 °C. The arrows indicate quenching the samples after different aging periods. 48

Figure 4-5 Sand mould shape casting of Al-6Zn-2Mg-2Cu alloy: camber link part. 49

Figure 4-6 Locations of the tensile samples cut from the camber link. 49

Figure 5-1 Image showing the typical appearance of the alloy castings (a) without the TiBor addition

(Alloy 7) and (b) with the TiBor addition (Alloy 7) Red frames document the locations of visible cracks.
 52

Figure 5-2 Typical grain structure of the as-cast Al-Zn-Mg-Cu alloys (a) without TiBor addition (Alloy 7) and (b) with TiBor addition (Alloy 7)..... 55

Figure 5-3 Effect of TiBor addition on the grain size of the 9 Taguchi alloys. Error bars represent 95% confidence interval..... 55

Figure 5-4 Typical morphology of the eutectic phases in the as-cast Alloy 2 (Al-3.5Zn-2Mg-1.2Cu): (a) 200x, (b) 500x. 57

Figure 5-5 Typical light optical micrographs of the un-etched as-cast Al-Zn-Mg-Cu alloys: (a) without TiBor addition (Alloy 2: Al-3.5 Zn-2 Mg-1.2 Cu), (b) with TiBor addition (Alloy 2: Al-3.5 Zn-2 Mg-1.2 Cu alloy), (c) without TiBor addition (Alloy 1: Al-3.5 Zn-1.5 Mg), (d) with TiBor addition (Alloy 6:Al-5 Zn-2.5 Mg Cu). 58

Figure 5-6 A set of replicate Engineering stress-strain curves for alloy 2..... 59

Figure 5-7 Mean, predicted mean and weighted mean values of YS, UTS, and El.% of the 9 Taguchi-designed alloys with TiBor addition in the NA condition. 62

Figure 5-8 Main effect plots showing the effect of alloying elements on S/N and Mean values: (a) S/N ratios for YS, (b) Mean for YS. 64

Figure 5-9 Main effect plots showing the effect of alloying elements on S/N and Mean values: (a) S/N ratio for UTS, (b) Mean for UTS. 65

Figure 5-10 Main effect plots showing the effect of alloying elements on S/N and Mean values: (a) S/N ratio for El.%, (b) Mean for El.%. 66

Figure 5-11 Typical tensile curve of the shape-cast Al-6Zn-2Mg-2Cu-0.25Ti alloy in the as-cast condition. 71

Figure 5-12 Typical tensile curve of the shap-cast Al-6Zn-2Mg-2Cu-0.25Ti alloy in the NA condition..... 71

Figure 5-13 Artificially ageing response of the shape-cast Al-6Zn-2Mg-2Cu alloy at 120 °C and 180 °C: (a) Strength (YS & UTS), (b) El.%. 72

Figure 5-14 Typical tensile curves of cast Al-6Zn-2Mg-2Cu alloy during the AA treatment: (a) under-aged and peak-aged conditions and (b) peak-aged and over-aged conditions. 76

Figure 5-15 El.% versus YS plots for shape cast Al-6Zn-2Mg-2Cu alloys, subjected to different ageing conditions: (a) 24 h at 120 °C plus 30 h. at 180 °C, (b) 1 h. at 120 °C plus 73 h. at 180 °C..... 79

Figure 7-1 Image showing the appearance of the alloy castings (a) without the TiBor addition (Alloy 1) and (b) with the TiBor addition (Alloy 1). Red frames document the locations of visible cracks..... 84

7- 2 Image showing the appearance of the alloy castings (a) without the TiBor addition (Alloy 2) and (b) with the TiBor addition (Alloy 2). Red frames document the locations of visible cracks. 85

Figure 7-3 Image showing the appearance of the alloy castings (a) without the TiBor addition (Alloy 3) and (b) with the TiBor addition (Alloy 3). Red frames document the locations of visible cracks..... 86

Figure 7-4 Image showing the appearance of the alloy castings (a) without the TiBor addition (Alloy 4) and (b) with the TiBor addition (Alloy 4). Red frames document the locations of visible cracks..... 87

Figure 7-5 Image showing the appearance of the alloy castings (a) without the TiBor addition (Alloy 5) and (b) with the TiBor addition (Alloy 5). Red frames document the locations of visible cracks..... 88

Figure 7-6 Image showing the appearance of the alloy castings (a) without the TiBor addition (Alloy 6) and (b) with the TiBor addition (Alloy 6). Red frames document the locations of visible cracks..... 89

Figure 7-7 Image showing the appearance of the alloy castings (a) without the TiBor addition (Alloy 7) and (b) with the TiBor addition (Alloy 7). Red frames document the locations of visible cracks..... 90

Figure 7-8 Image showing the appearance of the alloy castings (a) without the TiBor addition (Alloy 8) and (b) with the TiBor addition (Alloy 8). Red frames document the locations of visible cracks..... 91

Figure 7-9 Image showing the appearance of the alloy castings (a) without the TiBor addition (Alloy 9) and (b) with the TiBor addition (Alloy 9). Red frames document the locations of visible cracks..... 92

Figure 8-1 Typical grain structure of as-cast Al-Zn-Mg-Cu alloys before (images on the left) and after (images on the right) grain refinement: (a) and (b) alloy 1, (c) and (d) alloy 2, (e) and (f) alloy 3, (g) and (h) alloy 4, (i) and (j) alloy 5, (k) and (l) alloy 6, (m) and (n) alloy 7, (o) and (p) alloy 8, (q) and (r) alloy 9..... 95

Figure 9-1 Typical heating (T-t) and first derivative (dT/dt) curves for the Al-3.5Zn-2Mg-1.2Cu alloy. T_m denotes the melting temperature of the sample..... 96

Figure 9-2 Thermal analysis of the 9 Taguchi designed alloys (Heating curves and their first derivative): (a) Alloy 1, (b) Alloy 2, (c) Alloy 3, (d) Alloy 4, (e) Alloy 5, (f) Alloy 6, (g) Alloy 7, (h) Alloy 8, (i) Alloy 9.

..... 101

Figure 10-1 Tensile curves of the 9 Taguchi designed alloys: (a) Alloy 1, (b) Alloy 2, (c) Alloy 3, (d) Alloy 4, (e) Alloy 5, (f) Alloy 6, (g) Alloy 7, (h) Alloy 8, (i) Alloy 9. 106

Figure 11-1 Tensile curves of the validation alloys: 15 min. at 120 °C + NA..... 111

Figure 11-2 Tensile curves of the validation alloys: 1 h. at 120 °C + NA..... 112

Figure 11-3 Tensile curves of the validation alloys: 12 h. at 120 °C + NA..... 112

Figure 11-4 Tensile curves of the validation alloys: 24 h. at 120 °C + 5 h. at 180 °C + NA..... 113

Figure 11-5 Tensile curves of the validation alloys: 24 h. at 120 °C + 30 h. at 180 °C + NA..... 113

List of tables

<i>Table 2-1 Chemical compositions of studied Al-Zn-Mg-Cu alloys (wt%) [6].....</i>	<i>16</i>
<i>Table 2-2 Design of experiment using the Taguchi method. The *Hv and *Ec denote the results of S/N ratio for micro hardness and electrical conductivity, respectively [31].....</i>	<i>34</i>
<i>Table 4-1 Factor-level matrix for Taguchi-designed alloys.....</i>	<i>39</i>
<i>Table 4-2 Chemical compositions of the 9 Taguchi-designed alloys.....</i>	<i>40</i>
<i>Table 4-3 Solution treatments of the 9 Taguchi-designed alloys.....</i>	<i>42</i>
<i>Table 5-1 Composition (wt.%) of the 9 alloy castings determined using GDOES.....</i>	<i>50</i>
<i>Table 5-2 Pandat predictions of the type and amount of formed phases during non-equilibrium solidification of the 9 Taguchi-designed alloys.....</i>	<i>56</i>
<i>Table 5-3 R-square and Adjusted R-square values of the models.....</i>	<i>67</i>
<i>Table 5-4 Experimentally measured YS (MPa), UTS (MPa), El.% for Al-6Zn-2Mg-2Cu Alloy.....</i>	<i>67</i>
<i>Table 5-5 Predicted properties of the verification alloy.....</i>	<i>68</i>
<i>Table 5-6 Tensile results of sand mold shape cast Al-6Zn-2Mg-2Cu alloys (part 1 and 2).....</i>	<i>80</i>
<i>Table 10-1 List of tensile properties data for the Taguchi designed 9 alloys.....</i>	<i>107</i>
<i>Table 10-2 Experimental and predicted means and S/N ratios of YS, UTS, El.%.....</i>	<i>110</i>

1 Introduction

The government mandated fuel efficiency standards for automobile manufacturers reinforce the incentives to reduce the fuel consumption of their vehicles and minimize CO₂ greenhouse emissions. One of the effective means to address this challenge has been the design and application of lightweight materials including cast Al alloys for automotive parts. Most of the shape cast Al components currently utilized are produced using Al-Si alloys. Despite their excellent castability, these alloys possess moderate strength and toughness. In contrast, the Al-Zn-Mg-Cu alloys have considerably higher strength and toughness. Therefore, employing such high strength Al alloys for casting structural components is expected to improve their performance and reduce their weight.

Application of the Al-Zn-Mg-Cu alloys as shape cast parts has been limited due to technological obstacles related to their poor castability (fluidity & feedability) and susceptibility to hot tearing, both of which being consequences of the wide mush zone inherent to these compositions. Hot tearing is a result of plastic strain generated during solidification (liquid-to-solid phase transformation) due to the accompanying volumetric shrinkage. Figure 1-1 (a) shows schematic illustration of stresses that are formed during solidification as a result which metal either deforms without hot tears (Figure 1-1 (b)) or fails to resist the stresses and ends up in hot tears (Figure 1-1 (c)) [1].

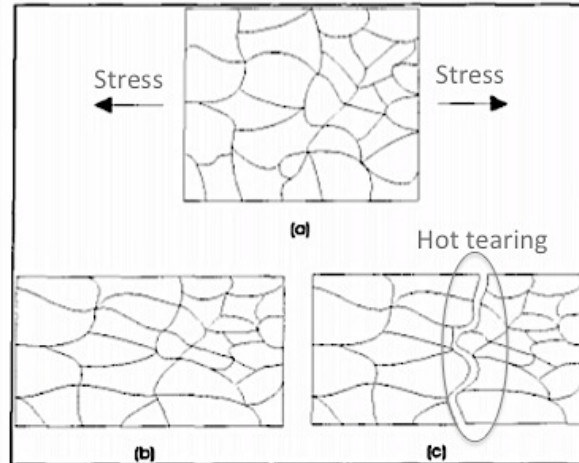


Figure 1-1 Schematic illustration of hot tearing. [1]

Metallurgical factors including the solidification range, eutectic percentage and eutectic type have been shown to have a significant impact on the hot tearing susceptibility of cast aluminum alloys: all of which are essentially controlled by the alloy composition [2]. Along a similar vein, grain refinement has been a common practice to reduce the hot tearing susceptibility of Al alloys through the delay in coherency point and enhancement in strength and ductility of semi-solid material (figure 1-2) [2, 3].

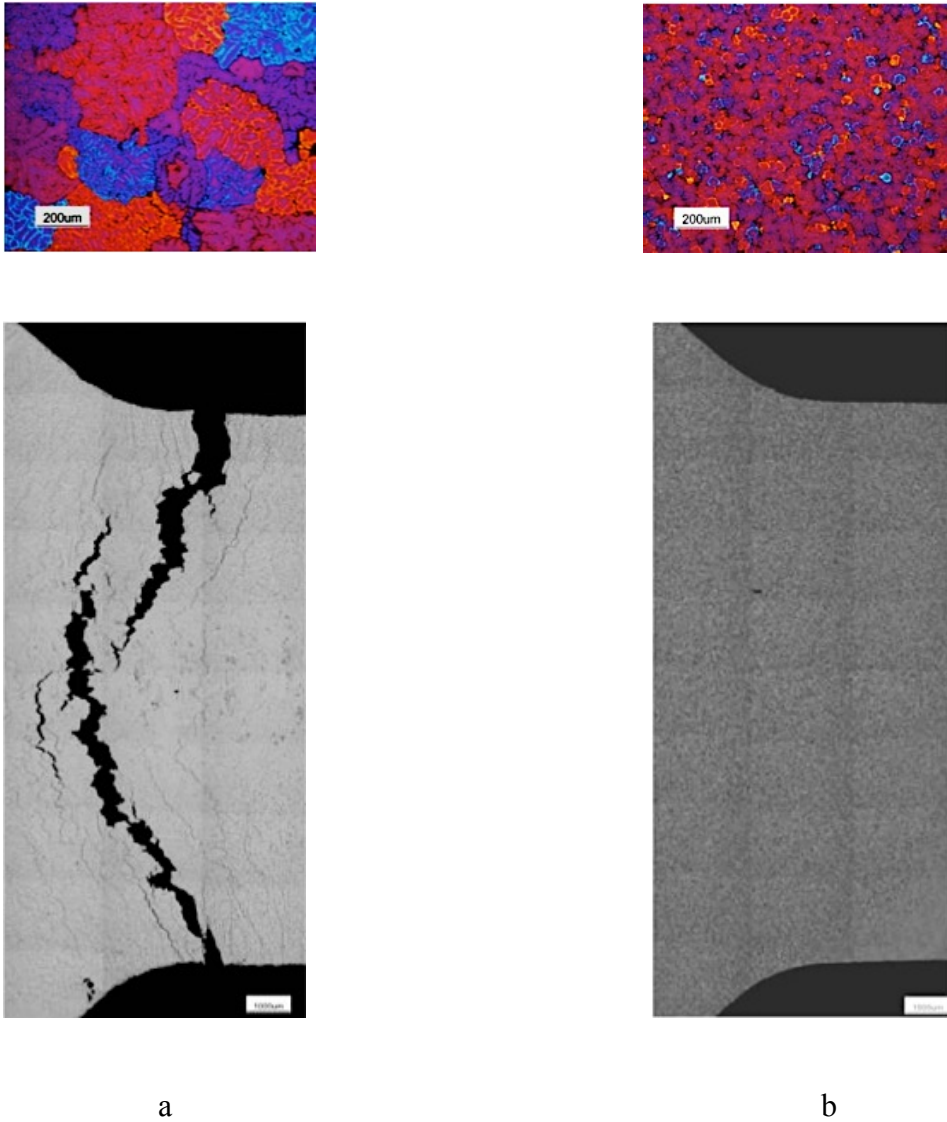


Figure 1-2 Effect of grain refinement on grain structure and hot tearing susceptibility of A206: (a) Before grain refinement, (b) After grain refinement [2].

Warrington [4] studied the role of grain refinement as a means to reduce the hot tearing susceptibility of Al-Zn-Mg-Cu alloys during casting. The type of grain refiner has been found to significantly affect the resultant microstructure and, thus castability and hot tearing susceptibility. Figure 1-3 shows optical micrographs (OM) of an Al-6Zn-2.2Mg-

2.2Cu (0.05 wt.% Ti) alloy cast with three different types of commercial master grain refining alloys A, B and C, which resulted in an equiaxed-cellular, equiaxed-dendritic and the mixed equiaxed-columnar microstructures, respectively [4]. It was noted that the hot tearing crack length was smallest within the equiaxed-dendritic microstructure (Figure 1-3d). It was observed that there was an optimum level Ti for minimum hot tearing susceptibility (Figure 1-4). The optimum level of Ti depended on the alloy composition itself. Low levels of Ti resulted in an equiaxed-dendritic microstructure, whereas higher Ti levels resulted in an equiaxed-cellular microstructure.

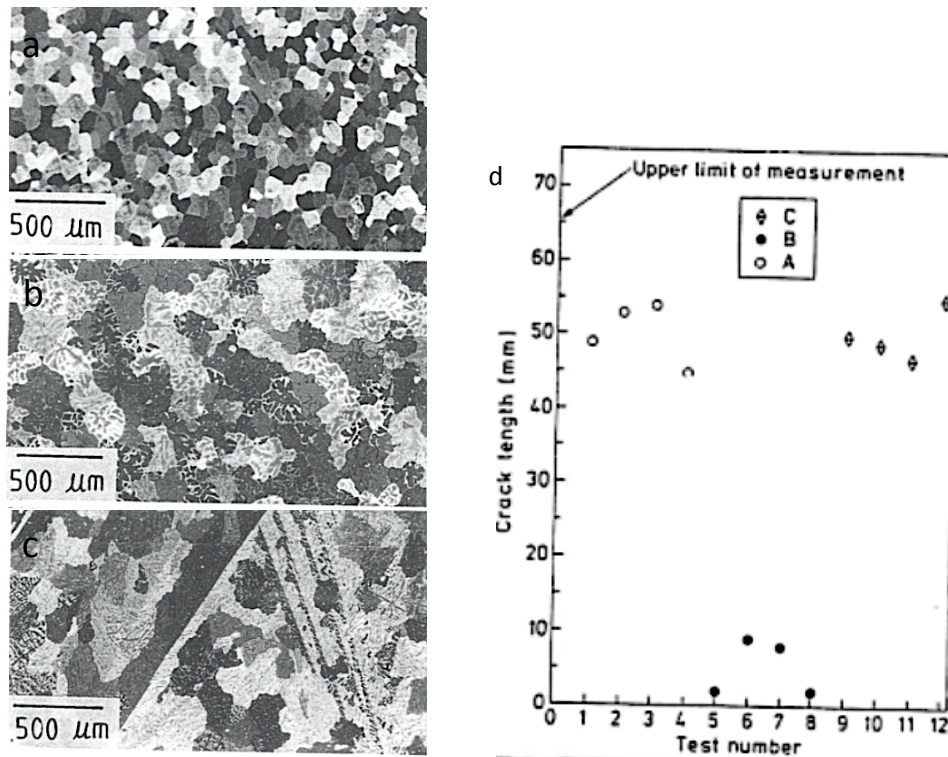


Figure 1-3 Grain refined Al-6Zn-2.2Mg-2.2Cu: (a) OM of A type (5Ti-1B-remainder Al) added, (b) OM of B type (6Ti-remainder Al) added, (c) OM of C type (6Ti-remainder Al) added, (d) Hot crack lengths [4]

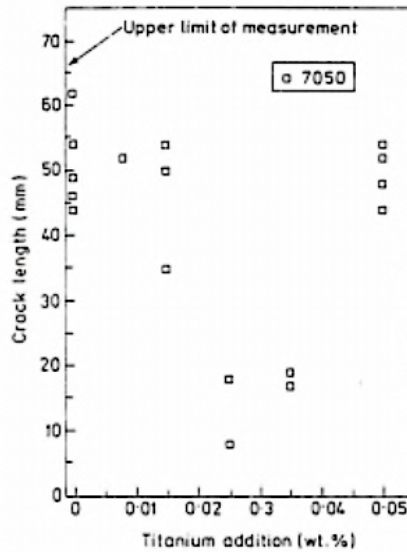


Figure 1-4 Length of crack in Al-6Zn-2.2Mg-2.2Cu as a function of Ti (wt.%) [4]

The reported literature lacks information on the shape casting of Al-Zn-Mg-Cu alloys and their heat treatment response. There has been no comprehensive study to date that depicts the influence of the alloy composition on the solidification characteristics, microstructure, mechanical properties of Al-Zn-Mg-Cu alloys. A fundamental baseline understanding of the structure–property relationships in shape cast Al-Zn-Mg-Cu alloys is required to identify an appropriate alloy composition that will meet the performance demands. This research project addresses the interest of automotive industry by examining the castability of these alloys, characterizing their microstructure and mechanical properties, finding the relationship between mechanical properties and chemistry and introducing the alloys with highest casting quality. A total of 9 alloys in Al-Zn-Mg-Cu system alloys have been cast and studied in accordance with Taguchi experimental design by means of tilt pour permanent mold process, which enables evaluating the effect of different levels of Zn,

Mg, Cu and Ti on tensile properties.

The remainder of the thesis consists of four chapters. Chapter 2 presents and discusses a concise review of the published literature on Al-Zn-Mg-Cu alloys with an emphasis placed on the casting quality and the influence of heat treatment on the microstructure and associated mechanical properties. Chapter 3 presents the research hypothesis distilled from the literature review, and presents Al-Zn-Mg-Cu alloys that are predicted to improve the mechanical properties. Chapter 4 documents the experimental procedure and the design of experiments used for alloy design in accordance with the Taguchi method. Chapter 5 presents and discusses the results of microstructure, mechanical properties and property models developed through the statistical analysis applied. The results and discussion of the property measurements made on the validation alloy are also included in this chapter. Chapter 7 then presents the conclusions extracted from the study and outlines the directions future research should follow.

2 Literature review

In this chapter, a review of published work on cast Al-Zn-Mg-Cu alloys is provided. In order to make shape cast Al-Zn-Mg-Cu parts both physically and structurally suited for specific application in the automotive industry, a post-cast heat treatment is essential, which necessitate a comprehensive review of the literature related to heat treatment parameters.

2.1 Microstructure of as-cast Al-Zn-Mg-Cu alloys

A thorough understanding of the morphology, stability and chemistry of the constituent phases in the as-cast condition is required to better understand the solid-state phase transformation that occur during the aging. Establishing such links is considered essential in the attempt to optimizing the heat treatment response of the Al-Zn-Mg-Cu alloys. Four major intermetallic phases can be expected to form below the solidus temperature of Al-Zn-Mg-Cu systems [5, 6]:

1. Hexagonal η (MgZn_2), also called as M phase in the literature
2. Cubic T ($\text{Al}_2\text{Mg}_3\text{Zn}_3$)
3. Orthorhombic S (Al_2CuMg)
4. Tetragonal θ (Al_2Cu)

The S, T and η are solid solutions with a range of compositions. The ternary S ternary phase in the Al-Cu-Mg system dissolves Zn up to 30 wt.%, whilst the T phase dissolves

Cu up to 28 wt.%. The MgZn_2 phase dissolves both Cu and Al to form a $\text{Mg}(\text{Zn,Cu,Al})_2$ phase. The θ phase is a binary phase in the Al-Cu system, which dissolves neither Zn nor Mg [7, 8]. The parallel solidification of three quasi-binary eutectic reactions determine the predominant eutectic structure of the alloy: [7]

1. α -Al and η [MgZn_2]
2. α -Al and T [$\text{Al}_2\text{Mg}_3\text{Zn}_3$]
3. α -Al and S [Al_2CuMg]

Other phases such as $\text{Al}_7\text{Cu}_2\text{Fe}$ and Mg_2Si can be found in the microstructure of the as-cast alloy, depending on the alloy composition. Bin et. al. [9] cast an ingot of Al-8.1Zn-2.05Mg-2.3Cu alloy into a Cu plate-shape mold. Their major findings are reproduced in Figure 2-1. They observed a large number of residual phases on the grain boundaries of the as-cast microstructure with the composition close to $\text{Al}_7\text{Cu}_2\text{Fe}$ and T ($\text{Al}_2\text{Mg}_3\text{Zn}_3$) phases.

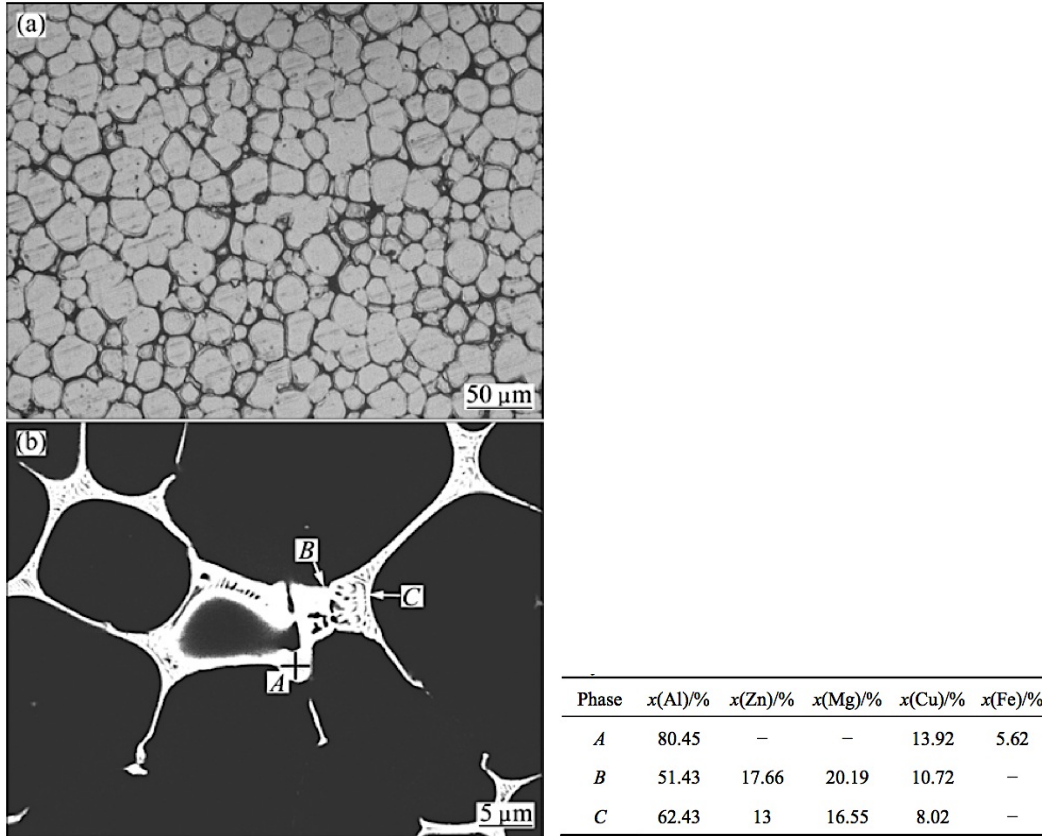


Figure 2-1 Microstructure of the as-cast Al-8.1Zn-2.05Mg-2.3Cu: (a) light optical microscopy image, (b) SEM image showing grain boundary decoration (spot A: $\text{Al}_7\text{Cu}_2\text{Fe}$; Spot B and C: T phase ($\text{Al}_2\text{Mg}_3\text{Zn}_3$)) [9].

2.2 Solution treatment of Al-Zn-Mg-Cu alloys

Solution treatment is the first step in the precipitation hardening process where in theory the material is heated to an elevated temperature to homogenize the microstructure: changing the morphology of the interdendritic phases, and dissolving soluble constituents. After a prescribe time (deemed sufficient to dissolve the soluble consistent), the alloy is rapidly cooled to room temperature to prohibit the dissolved constituents from

precipitation [10].

There are two important parameters in the solution treatment step: temperature and time. With respect to the temperature, solution treatment is carried out at a temperature just below the eutectic temperature in order to dissolve the majority of the hardening precipitates into solid solution. Care must be exercised to ensure avoidance of the partial/incipient melting of the non-equilibrium eutectic phases on the grain boundaries, which is very common in Cu containing Al alloys (Figure 2-1) [10].

The incipient melting occurs when the temperature of the solid solution treatment exceeds the melting point of the Cu containing non-equilibrium eutectic phases, as shown in Figure 2-2 and 2-3 [11]. This type of melting results in the formation of shrinkage cavities after the quench to room temperature, which adversely affect mechanical properties.

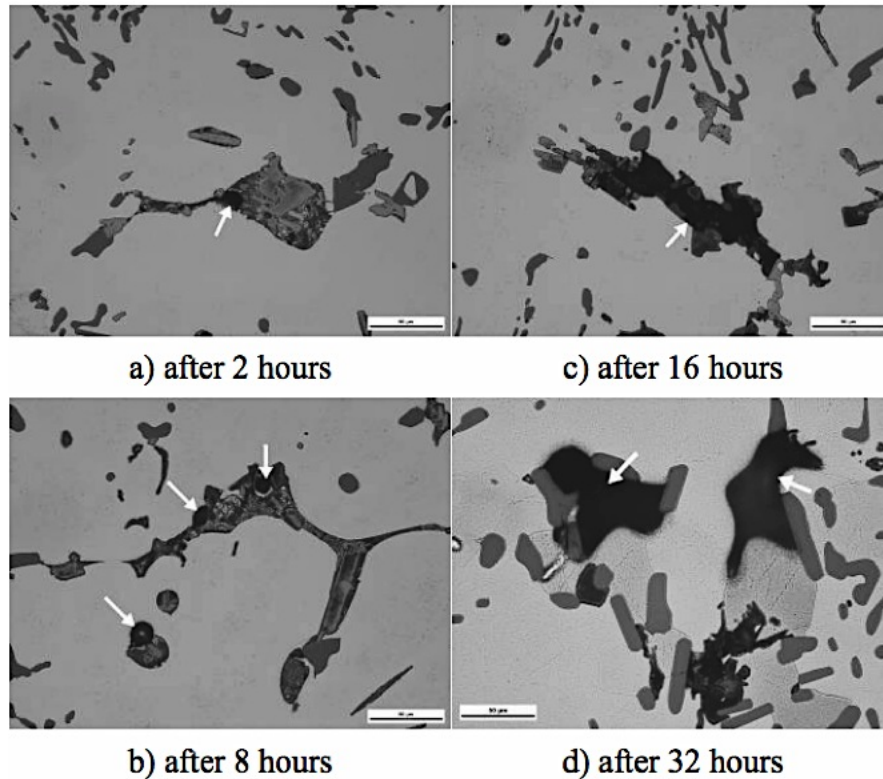


Figure 2-2 Incipient melting of Al-Al₂Cu-Si particles during solution treatment at 525 °C, etched. Arrows indicated the regions where incipient melting has occurred [10].

The precipitate dissolution rate is to a great extent sensitive to temperature and even a 10 °C variation might give significant alteration to the optimum solution treatment time. There have been a number of investigations on the solution treatment of Al alloys in recent years [12, 13, 5]. Some works have focused on the nature and evolution of the Al₂Mg₃Zn₃ (T), Al₂CuMg (S), (CuZnAl)₂Mg, and MgZn₂ (η) phases, while some other on the formation and distribution of dispersoids. Comparing the solution treatment of single and multiple steps has also received attention. A single step solution treatment of Al-Zn-Mg-Cu alloys is normally carried out at 470-480 °C. A multiple step solution treatment

consists of a conventional solution treatment followed by second step at a higher temperature. An increase in temperature results in a more severe atomic thermal vibration, larger atomic spacing, and a lower energy requirement for crystal atoms to move away from a balanced position to a new balanced or non-balanced site. Thus, the required activation energy decreases. Furthermore, a second step solution temperature results in a larger self-diffusion coefficient D . Therefore, the capability for atoms to conquer the activation energy barrier increases and dissolution of the precipitate phases becomes easier.

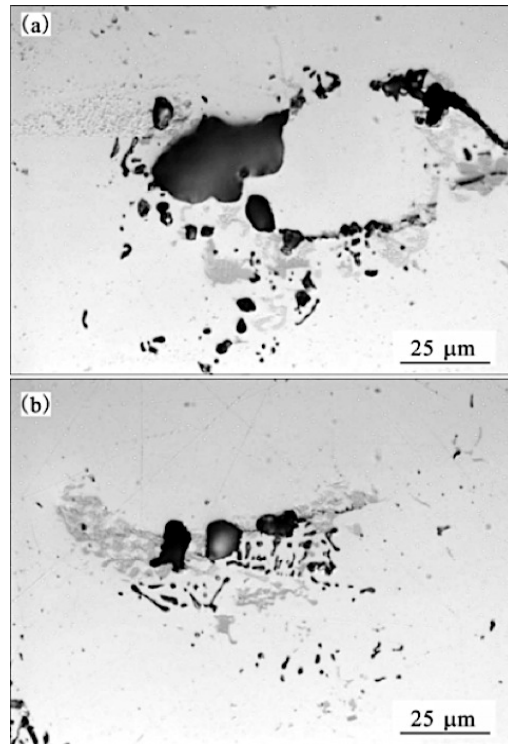


Figure 2-3 Light optical micrographs of pores caused by incipient melting in a Al-Zn-Mg-Cu alloy [11].

Gaosong et. al. [14] reported that the three-step solution treatment (200 °C for 2 h, 460 °C for 6 h, and then 480 °C for 12 h) was more effective for AA7075 than a single-step treatment (465 °C for 24 h). It was shown that the non-equilibrium eutectic phases in the ingot dissolve continuously into the matrix as the holding time of single-step solution treatment increased. However, the three-step solution treatment showed an improved capability to dissolve the non-equilibrium eutectic phases (Figure 2-4). The three-step solution treatment was also observed to completely eliminate the endothermic peak associated with the non-equilibrium eutectic phases.

According to Mei et. al. [15], any step-wise solution treatment should begin at a temperature below the first melting temperature with sufficient time to ensure the low melting eutectic phases are dissolved. They showed that an initial solution treatment step of 430 °C for 18 h followed by gradual heating to 467 °C for an additional 4 h was successful in dissolving the precipitate phases in an Al-7.8Zn-1.8Mg-1.5Cu and Al-6Zn-2Mg-2Cu alloy with the thinning of the grain boundary. It was noted that after a double-step solution treatment, the microstructure still contained a small quantity of un-dissolved Al_2CuMg particles. Lim et. al. [16] found that a multiple-step solution treatment was required in order to ensure the uniformity of the microstructure in AA7175 and AA7050 alloys.

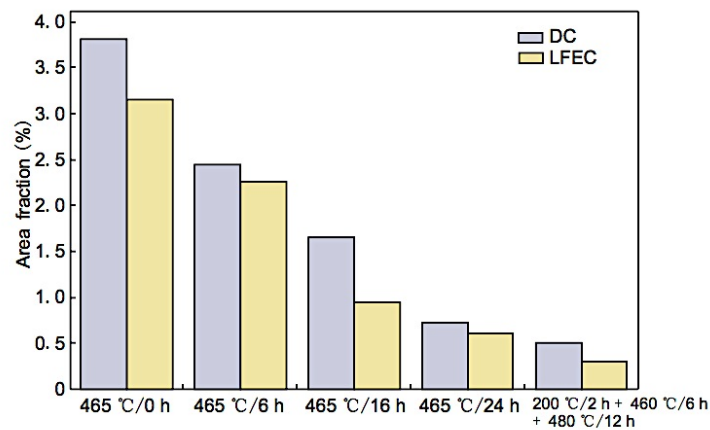


Figure 2-4 Area fraction (%) of residual phase in AA7075 subjected to different solution treatments [14].

Eivani et. al. [17] performed extensive research on solution treatments of DC cast AA7020 alloys (Al-4.37Zn-1.2Mg-0.19Cu) at 390 °C, 430 °C, 470 °C, 510 °C, and 550 °C for 2, 4, 8, 16, 24, and 48 h each. As shown in Figure 2-5, a solution treatment at 390 °C and 430 °C increased the volume fraction of particles (formation of $MgZn_2$ and Mg_2Si precipitates). The formation of these precipitates (particles) was attributed to the supersaturation of the solid solution matrix phase with alloying elements due to the microsegregation that occurred during solidification with the high cooling rates applied during DC casting. Solution treating the as-cast alloy at a temperature < 470 °C increased the particle (precipitate) volume fraction, whereas increasing the temperature > 470 °C had the opposite effect.

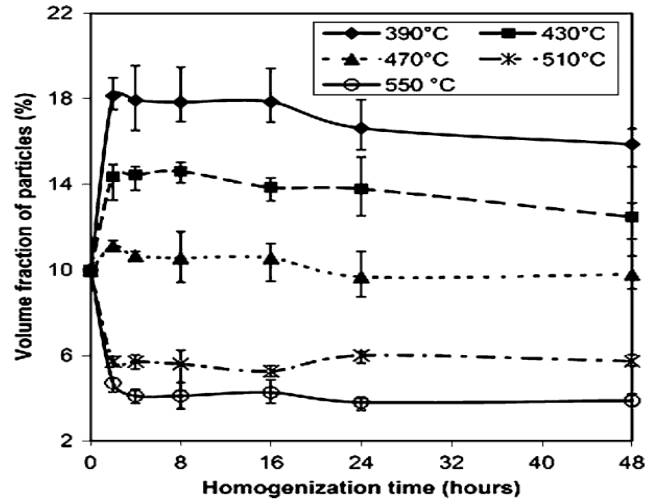


Figure 2-5 Effect of solution treatment (homogenization) time on the volume fraction of particles in Al-4.37Zn-1.2Mg-0.19Cu alloys [17].

Li et. al. [6] investigated the effect of composition on the solvi of the S phase of the wrought AA7010, AA7050 and AA7075 commercial alloys using differential scanning calorimetry (DSC) (Table 2-1). The S phase solvus indicated that a solution treatment temperature of 475 °C for alloys B and C was within the (α +S) phase field, thus the S phase could not be dissolved in these alloys at this temperature (Figure 2-6). Alloy A was practically on the S phase solvus, and given a sufficient solution treatment time, the S phase would be expected to dissolve. Therefore, dissolution of S phase was possible for alloy C through increasing the solution treatment temperature to just below 490 °C, whilst complete dissolution of S phase is impossible for alloy B.

Table 2-1 Chemical compositions of studied Al-Zn-Mg-Cu alloys (wt%) [6]

Alloy	Zn	Mg	Cu	Al, Zr, Ti, Cr & impurities
A	5.94	2.34	1.79	Remainder
B	6.12	2.34	2.58	
C	6.51	2.96	1.91	
7010	5.7-6.7	2.1-2.6	1.5-2.0	
7050	5.7-6.7	1.9-2.6	2.0-2.6	
7075	5.1-6.1	2.1-2.9	1.2-2.0	

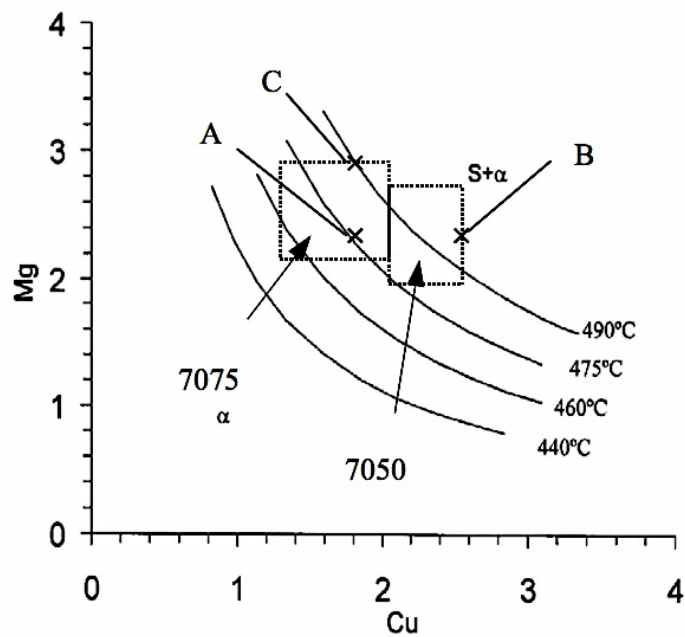


Figure 2-6 Solvi of the S phase in Al-Zn-Mg-Cu alloys with Zn=6 wt% as a function of the alloy Cu content [6].

2.3 Quench

Quenching is the next step after solution treatment and is necessary to preserve the solid solution formed at the elevated temperature. The solution treated material is subsequently cooled at a sufficient rate to avoid precipitation during cooling, which otherwise, would result in formation of coarse precipitates within the matrix (Figure 2-7) [5, 18]. Quenching to room temperature keeps the solute atoms and vacancies in the solid solution. The vacancies are essential in promoting the low temperature diffusion required for formation GP zone (first phase (nm scale) to nucleate during the precipitation reaction sequence).

A variety of quenching environments are available: air, water (either at room or higher temperature), polyalkylene glycol and forced mist. Slower cooling rates are adopted for components with complex shapes and ones with different thicknesses, to avoid distortion and excessive residual stresses. Quench sensitivity refers to the extent to which slower cooler rates can be tolerated without formation of any precipitate during cooling. The quench sensitivity of an alloy is best understood by inspecting the Continuous Cooling Transformation (CCT) diagram, which shows the allowable delay between solution treatment and quenching. Quench sensitivity increases with the increase in solute levels, which makes it easier for precipitates to form during cooling. Moreover, quench sensitivity is affected by presence of the coarse constituent intermetallic particles in the matrix, which can provide interfaces for heterogeneous nucleation of large precipitates. Quench sensitivity is especially important for thick components where the center may turn weaker due to slower cooling [19].

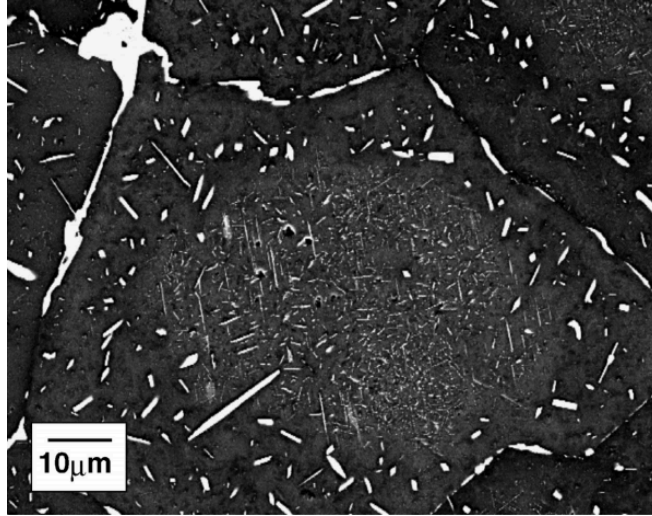


Figure 2-7 Formation of large precipitates in a slowly cooled Al-6.7Zn-2.6Mg-2.6Cu alloy. Alloy was solution at 480 °C for 24 h, and then slowly cooled. Needle-shape Zn-rich σ phase were formed [5].

2.4 Aging response of Al-Zn-Mg-Cu alloys

Aging is the last step in the heat treating of Al-Zn-Mg-Cu alloys. After solution treatment and quenching, the material is aged either at room temperature or higher. During aging, the supersaturated solid solution (SSSS) is decomposed in a controlled manner to form the finely dispersed precipitates necessary to increase the strength (precipitation hardening). The precipitation sequence during aging includes:

SSSS, vacancy-rich clusters (VRC), GP zones, metastable η' , stable η (MgZn_2) [20, 21].

The driving force for precipitation during aging treatment is the decrease in the energy of the system. The aging treatments at room temperature and higher are termed natural and artificial aging, respectively.

2.4.1 Natural aging response of Al-Zn-Mg-Cu alloys at room temperature

Quenching after solution treatment is one of the processes that introduces point defects into the system. During subsequent heat treatment at lower temperatures, grain boundaries act as sinks for the vacancies nearby, which reduce their concentration in the immediate vicinity. This resulting concentration gradient is the driving force for vacancies to diffuse towards the grain boundaries. Vacancies tend to couple with solutes during their diffusion towards the grain boundaries, producing vacancy-solute clusters [22].

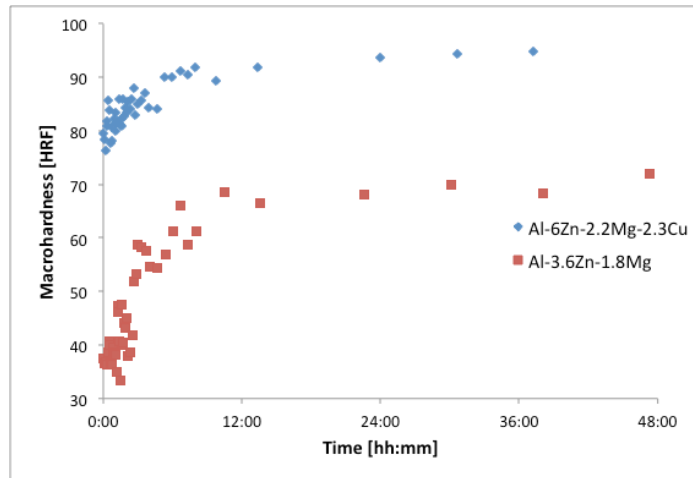
During natural aging of Al-Zn-Mg-Cu alloys the supersaturated solutes (specifically Mg) and vacancies join together to decrease the energy of the system, forming the clusters that are the precursors to the GP zones. Since the diffusion rate is low during natural aging (room temperature), the precipitation sequence stops at GP [21]. Therefore, the microstructure of naturally aged Al-Zn-Mg-Cu alloys features the distribution of coherent GP precipitates within the matrix, which are primarily responsible for the alloy's strength in this condition. [23].

GP zone formation is linked to the relative solute-vacancy interaction. Sha [24] studied the early stages of precipitation in an Al-6.29Zn-2.2Mg-2.2Cu alloy and found that fine clusters of solutes formed within the first 1.5 h of natural aging, which eventually transformed into GP zones. It was suggested that Mg diffusion controlled the nucleation of GP zones, whereas Zn diffusion controlled the growth of GP zones. During the GP zone growth, Zn atoms diffused to blocky shape clusters and increased the Zn/Mg ratio to 1, which corresponds to the composition of GP zones. Furthermore, “young” GP zones

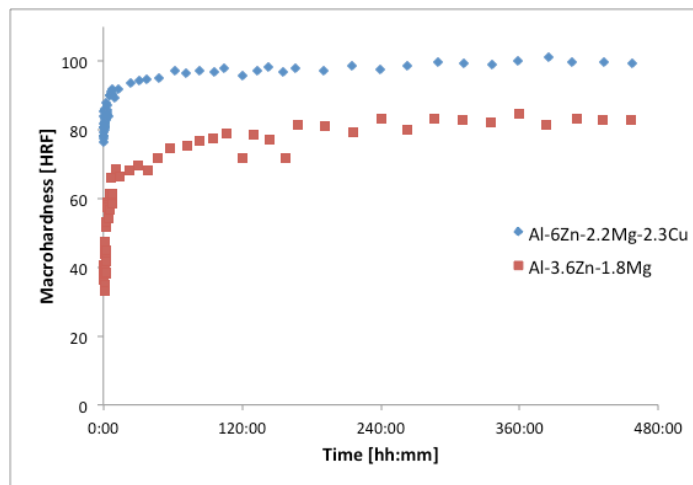
contained more Cu (close to 12 at. %), whereas “mature” GP zones contained less Cu (close to 5 at. %) indicating a significant role played by Cu in the early stages of GP zone growth.

Berg [21] reported that GP zones formed in the temperature range from room temperature up to 140 °C, were fully coherent with the Al matrix and featured a spherical shape. Luca [25] studied the effect of natural aging on the hardness of an Al-6Zn-2.2Mg-2.3Cu and Al-3.6-1.8Mg alloy (Figure 2-8). Hardness values increased rapidly in the first 12 h of natural aging before reaching a plateau after a specific time for each alloy (100 h for Al-6Zn-2.2Mg-2.3Cu and 240 h for Al-3.6-1.8Mg) remaining nearly unchanged until 480 h.

Deschamps [26] investigated on the effect of quench rates (air and water) on the kinetics of precipitation hardening of an Al-6.1Zn-2.3Mg-0.1Zr alloy during natural aging (Figure 2-9). It was observed that the air quench resulted in a slower rate of precipitation at room temperature, which was caused by the relative loss of average solutes and vacancies supersaturation during the air quench. DSC curves were also acquired after natural aging for 3 days [26]. During the heating of naturally-aged samples, a fraction of the GP zones dissolved and the remainder acted as precursor for formation of the η' and η phases. Figure 2-10 shows multiple peaks in the DSC curves acquired. The endothermic peak A was attributed to the dissolution of GP zones, while the exothermic peaks B, C and D were attributed to the formation of η' , η and T phases, respectively. The endothermic Peak A was relatively small as the slow heating employed enabled the growth of a larger number of GP zones up to the temperature where the η' phase precipitated. In contrast, Figure 2-10-b shows the endothermic Peak A was relatively large with a more rapid heating as a result of GP zones dissolution.



a



b

Figure 2-8 Effect of natural aging time on the hardness of an Al-6Zn-2.2Mg-2.3Cu and Al-3.6-1.8Mg alloy: (a)early stages (48 h) and (b) later stages(480 h) [25].

Moreover, the peak corresponding to formation of the η' phase precipitates was small when for the water-quenched alloy and essentially non-existent for the air-quenched

alloy. This difference was attributed to the large number of GP zones that were previously dissolved at the lower temperatures, which in turn reduced the number of nucleation sites for formation of the η' phase precipitates.

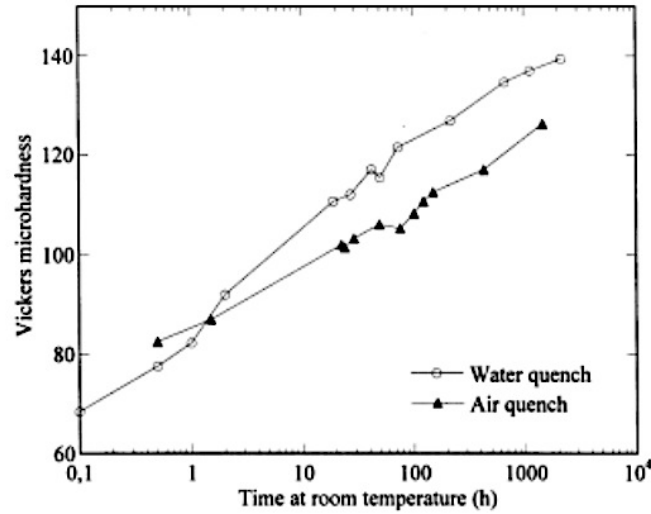


Figure 2-9 Effect of natural aging time on the hardness of an Al-6.1Zn-2.3Mg-0.1Zr alloy after solution treatment followed by a water quench or an air quench [26].

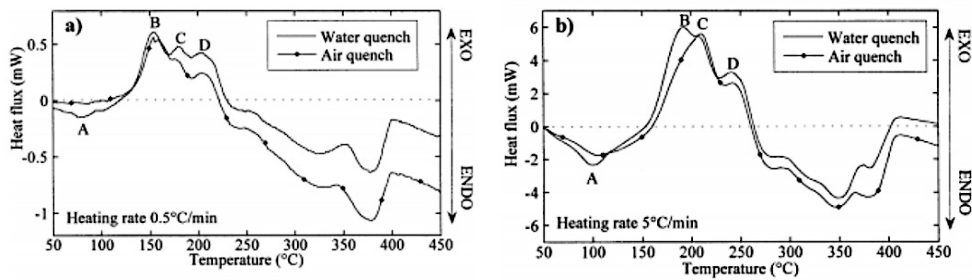


Figure 2-10 DSC curves of a naturally-aged Al-6.1Zn-2.3Mg-0.1Zr alloy after solution treatment followed by a water quench or an air quench:(a) $0.5^{\circ}\text{C min}^{-1}$ and (b) $5^{\circ}\text{C min}^{-1}$ [26].

2.4.2 Artificial aging response of Al-Zn-Mg-Cu alloys

Diffusion during artificially aging is faster than during natural aging due to a higher temperature. Both treatments typically start with decomposition, i.e. nucleation of precipitate from the SSSS. However, the nucleation occurs at a faster rate during artificially aging.

2.4.3 Artificial Aging response of Al-Zn-Mg-Cu alloys at 120 °C: Chemistry of precipitates

Buha et. al. [20] showed that densely dispersed precipitates of spherical GP zones formed very early in an Al-5.7Zn-2Mg-2Cu alloy after 15 min. of artificially aging at 130 °C (Figure 2-11). Sha et. al. [24] suggested that it takes a day (24 h) for the precipitation of GP zones to reach a steady state in an Al-6.29Zn-2.2Mg-2.2Cu alloy when naturally aged at room temperature, whereas steady state was achieved after just 60 min. (1 h) when artificially aged at 121 °C (Figure 2-12).

A higher diffusion rate at 120 °C (during artificially aging) allows the GP zones to attract more Zn atoms than they attract during natural aging. In this case, the spherical-shaped GP zones grow in one direction and transform to elongated-shaped η' with increased Zn/Mg ratio from 1 to 1.2. Alternatively spherical-shape GP zones have been observed to grow into coarse blocky clusters with a Zn/Mg ratio of 1 after 24 h of artificially aging at 120 °C [24].

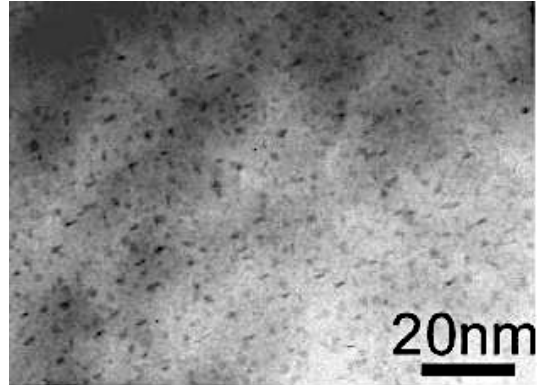


Figure 2-11 TEM image of Al-5.7Zn-2Mg-2Cu alloy after artificially aging for 15 min. at 130 °C [20].

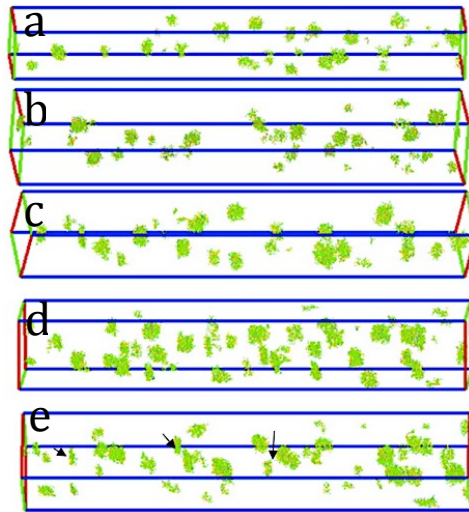


Figure 2-12 Mg-Zn clusters formed in an Al-6.29Zn-2.2Mg-2.2Cu alloy artificially aged at 120 °C for different times up to 24 h.: (a) 30 min., (b) 1, (c) 4, (d) 8 and (e) 24 h [24].

Wu et. al. [27] also reported that small GP zones can grow into stable blocky clusters, evolve into η' or dissolve in the Al matrix. A negligible presence of η' precipitates was observed in an Al-5.7Zn-2Mg-2Cu alloy after artificial aging at 130 °C for 15 min.

[20]. Sha [24] reported that for an Al-6.29Zn-2.2Mg-2.2Cu alloy, the η' phase first precipitates with a Zn/Mg ratio of 1.07 after artificially aged at 121 °C for 1 h. These precipitates were then observed to attract Zn atoms and grow in size with increased aging time up to 24 h, with the concomitant increase in the Zn/Mg ratio to 1.26. Figure 2-13 shows a TEM image of the Al-6.29Zn-2.2Mg-2.2Cu alloy indicating the co-existence of both spherical GP zones and rod-like η' precipitates after artificially aging at 120 °C for 24 h. In general, Zn plays an important role in the growth and stability of both GP zones and η' precipitates [24]. Despite spherical GP zones that can form both during natural aging and artificial aging (at 120-130 °C), plate-like GP zones nucleate from the SSSS only above ~ 70 °C and, therefore only during artificial aging. Vacancy concentration is crucial for formation of GP zones as they only appear in the microstructure of the samples that have been solution treated at temperatures higher than 450 °C [20].

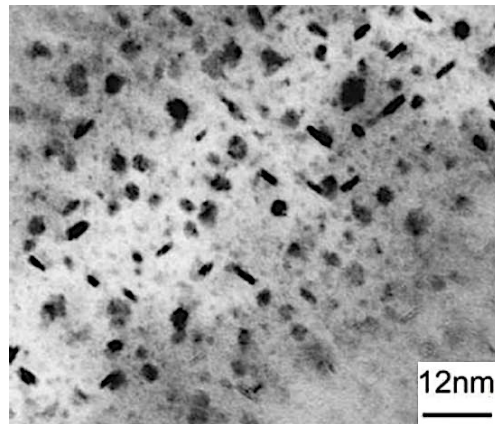


Figure 2-13 TEM image showing the nature of the precipitates that formed in an Al-6.29Zn-2.2Mg-2.2Cu alloy artificially aged at 120 °C for 24 h [24].

2.4.4 Artificial Aging response of Al-Zn-Mg-Cu alloys at 120 °C: Number density and size of precipitates

Figure 2-14 shows the evolution of cluster (precipitate) density, average cluster (precipitate) size and matrix composition of an Al-6.29Zn-2.2Mg-2.2Cu alloy as a function of aging time at 120 °C. The cluster density increased sharply during the first 30 min. of aging, after which it increased more slowly during subsequent aging to 480 min. A rapid growth in the average cluster size was noted during aging between 30 and 240 min., after which it increased much more slowly. According to Sha [24], the density of GP zones reached a peak at approximately 30 min. or earlier. Moreover, η' precipitation became significant after aging for 60 min., and become the dominant phase after aging for 240 min. and beyond. The concentrations of Zn, Mg and Cu in the matrix decreased with an increase in aging time, with the concentration of Zn decreasing much faster than that Mg, especially between 30 and 240 min. The Cu content of matrix remained almost unchanged with aging to 24 h.

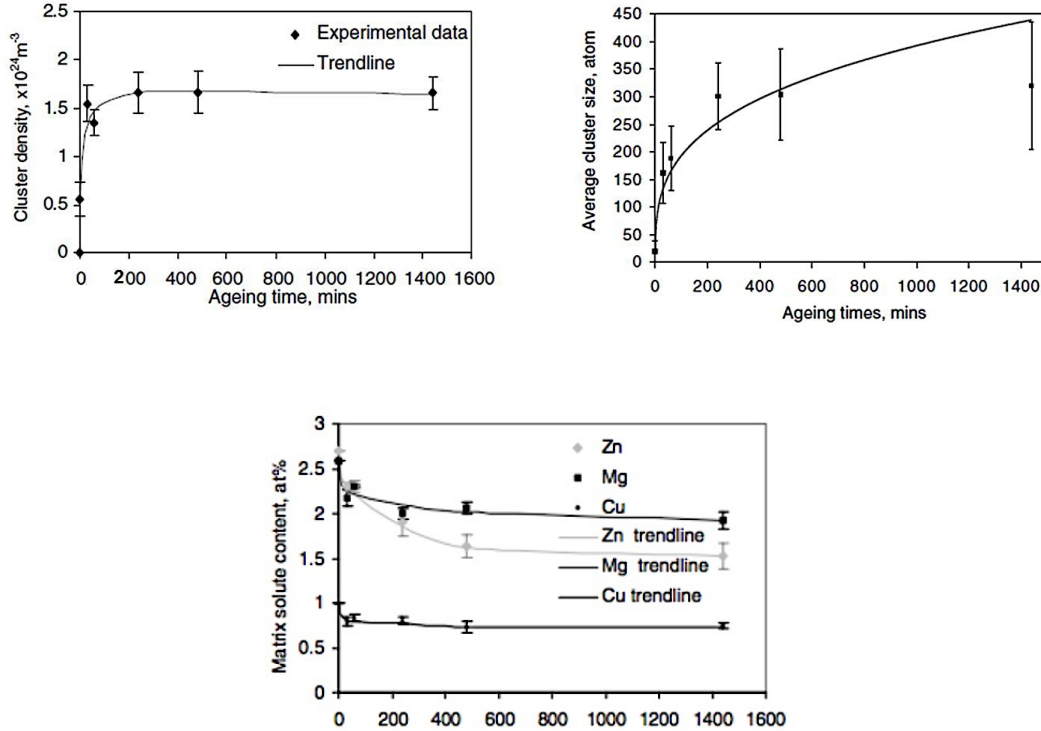


Figure 2-14 Artificial aging response of an Al-6.29Zn-2.2Mg-2.2Cu alloy at 120 °C: (a) cluster density, (b) average cluster size, (c) maximum solute content in the matrix [24].

2.4.5 Strengthening mechanism in precipitation hardened Al-Zn-Mg-Cu alloys

The strengthening mechanism deriving from the interaction between precipitates and dislocations is illustrated in Figure 2-15. Precipitates act as obstacles to dislocations motion and increase the strength of the alloy. Depending on the size of the precipitate, the encounter of dislocations with these obstacles varies. A small precipitate is sheared by the dislocation as per the Friedel effect to form an antiphase boundary (Figure 2-15-a). In contrast, the encounter of dislocation line with large and hard precipitate results in bending the dislocation around the particle. According to the Orowan mechanism,

dislocation can move on, leaving a dislocation ring around the bypassed particle (Figure 2-15-b).

Coherent GP zones and semi-coherent η' precipitates are smaller than the critical particle radius and are mainly sheared by the dislocation, whereas incoherent η precipitates are subjected to bow-out by the Orowan mechanism, leaving behind dislocation rings as it is difficult for a dislocation to move across the incoherent phase boundary. The hardening response reaches a peak when η' and GP zones dominate the microstructure. Afterwards, the number of η precipitates increases and the strength decreases. The strength of the alloy is controlled by adjusting the relative size of precipitate to critical particle size r_c (Figure 2-15-c).

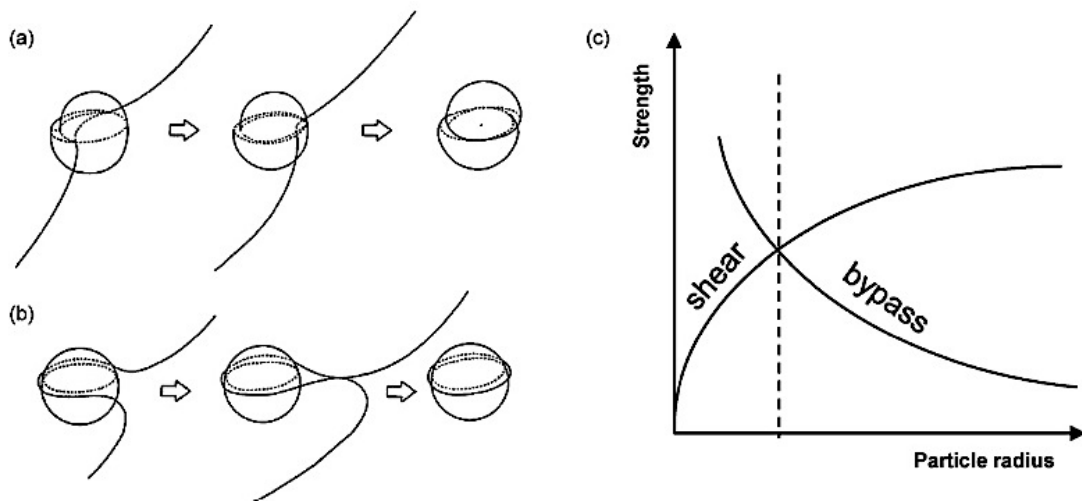


Figure 2-15 Schematic of precipitate hardening mechanisms: (a) shearing, (b) bowing, and (c) strengthening by small ($\sim\sqrt{r}$) and big ($\sim 1/r$) precipitates indicating transition from Friedel effect (particle shearing) to Orowan mechanism (bow-out between particles) at the critical particle radius [28].

2.4.6 Effect of temperature on the artificial aging response of Al-Zn-Mg-Cu alloys

Jin [29] studied the tensile properties, Brinell hardness and the electrical conductivity of an Al-7.5Zn-2Mg-2Cu alloy during artificially aging at 120 °C and 160 °C for different times (Figure 2-16). Aging at 120 °C increased the hardness relatively fast, reaching a maximum plateau during the early stage. Aging at 160 °C produced a significantly different hardness response. A hardness peak was observed by 2 h. after which the alloy over aged as indicated by the continued decrease in hardness with increasing aging time. It was observed that the electrical conductivity increased with the aging time at both 120 °C and 160 °C. The rate of increase was higher for 160 °C. The strength results show similar trend to hardness (Figure 2-17). During aging at 120 °C, the clusters nucleated immediately after the quench and begin to grow. Meanwhile, new clusters also formed and grew as aging progressed, which resulted in a size distribution of GP zones within the microstructure after 24 h. Moreover, small GP zones with higher surface energy likely acted as precursor to the formation of elongated η' precipitates, while the large GP zones continued to grow [24]. Therefore there was a co-existence of GP zones and metastable η' precipitates in the microstructure after 24 h. The rate of precipitation hardening increased with an increase in aging temperature. Aging at 160 °C resulted in the disappearance of diffraction spots associated with GP zones, which indicated that GP zones dissolved into the matrix or transformed into η' precipitates. Therefore, η' and η were the dominant precipitates formed during aging at 160 °C. After aging for 1 h, the dominant precipitate was the metastable η' phase. In contrast, the dominant precipitate after aging for 24 h was the stable η phase, which indicated that the transformation of η' to η was feasible at 160 °C.

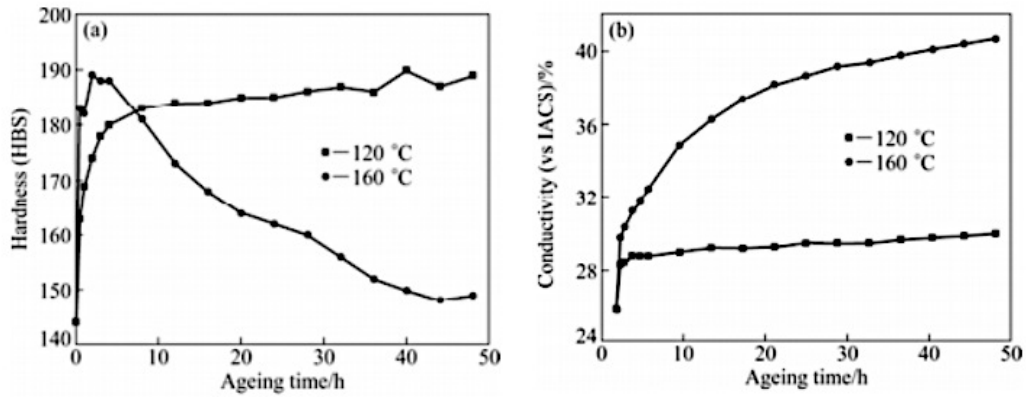


Figure 2-16 Artificially aging response of an Al-7.5Zn-2Mg-2Cu alloy: (a) hardness at both 120 °C and 160 °C, (b) electrical conductivity at both 120 °C and 160 °C [29].

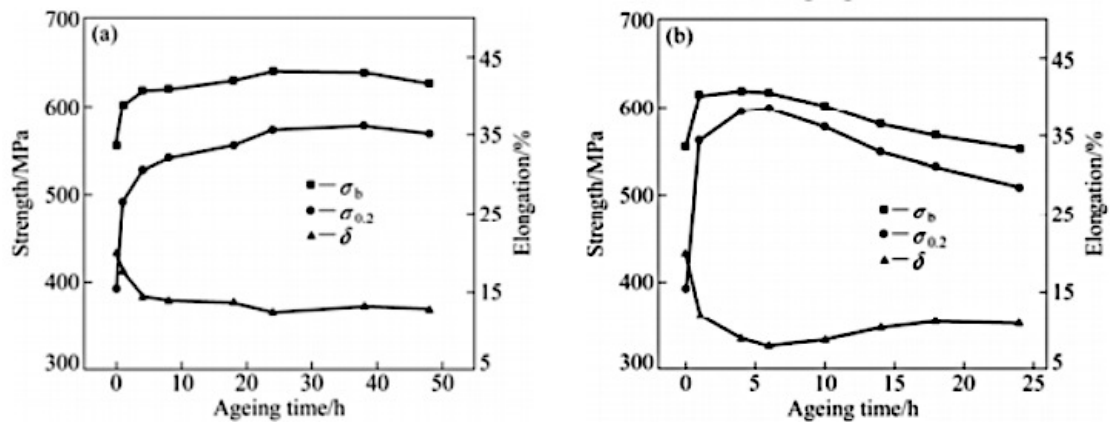


Figure 2-17 Artificial aging response of an Al-7.5Zn-2Mg-2Cu alloy: (a) tensile properties at 120 °C, (b) tensile properties at 160 °C [29].

2.4.7 Role of Cu in the artificial aging response of Al-Zn-Mg-Cu alloys

Adding Cu does not change the precipitation sequence of Al-Zn-Mg alloys. However, Cu does affect the precipitation hardening response, as it stimulates the formation of GP zones and η' phases, increases the number density of precipitates (a finer and denser population of intermediate precipitates) and improves their thermal stability. Consequently, the strengthening rate increases during the early stages of aging. Moreover, increasing the number density of precipitates improves the strength of Cu containing Al-Zn-Mg alloys [30]. Luca [25] studied the artificial aging hardening of an Al-6Zn-2.2Mg-2.3Cu and Al-3.6Zn-1.8Mg alloy (Figure 2-18). The hardness response as a function of aging versus time showed that the hardness of the Al-6Zn-2.2Mg-2.3Cu alloy increased more rapidly in the early stages of aging and reached a significantly higher hardness relative to that exhibited by the Al-3.6Zn-1.8Mg alloy.

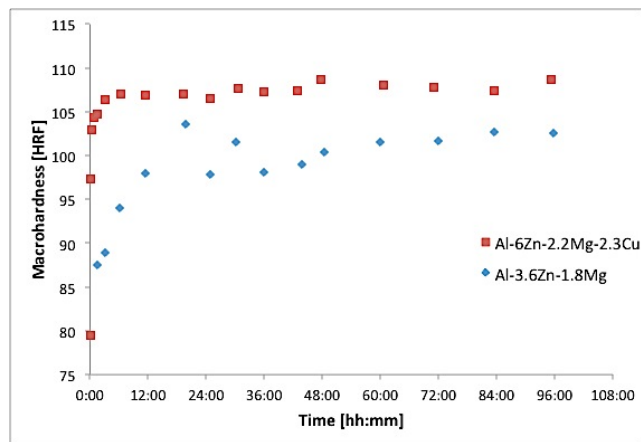


Figure 2-18 Artificial Aging response of an Al-6Zn-2.2Mg-2.3Cu and Al-3.6Zn-1.8Mg alloy

[25].

2.5 Design of experiment (DOE)

A design of experiments was required to evaluate the effect of independent variables (e. g., alloying elements) on dependent variables (e. g., mechanical properties) in this study. One of the common approaches to planning experiments is the one-factor-at-a-time method (or OFAT), which involves testing the effect of a single factor at a time. This method is undoubtedly a very time consuming and expensive approach due to multitude numbers of the required trials for high precision. It does not estimate the interaction effect of factors on the dependent variables. Furthermore, an experiment based on this method might miss the optimal settings of factors with respect to desired response (e.g., higher strength and elongation).

2.5.1 Factorial design

Factorial design is another common method to determine the effects of multiple factors with different levels on dependent variables. Factorial design can reduce the number of required runs by studying multiple factors simultaneously. The reason that one might favour the use of factorial design over OFAT is such an experiment allows the study of the effect of each factor, as well as the effects of interactions between factors on the dependent variables. Nevertheless, factorial design can be considered the best approach to experimental design when the interest lies on a small number of factors with few levels. Otherwise, since it takes on all possible combinations of levels across all factors, it can lead to a large number of trials, which can become expensive and time-consuming.

2.5.2 Taguchi method

Orthogonal arrays are special experimental designs suggested by Taguchi [31], which requires only a small number of experimental trials to discover the main and interaction effects of variables. Orthogonal arrays are fractional factorial designs, i.e. symmetrical subsets of all combinations of treatments in the corresponding full factorial designs. An experimental design based on the Taguchi method involves using orthogonal arrays to organize the independent variables affecting the dependent variables and the levels at which they should be varied. This method allows for the collection of the necessary data to determine which factors most affect the dependent variables, thus saving time and lowering the cost of experiment. Taguchi method is suggested as best experimental design when an intermediate number of variables are under investigation, few interactions exist between elements, and when only a few elements have significant contribution on the properties of interest.

2.5.3 Signal to noise ratio (S/N)

In the Taguchi method, control factors are those that can be controlled, while noise factors are that cannot be controlled during experimentation. Taguchi recommends using the S/N ratio. Higher values of the S/N ratio identify control factor settings that minimize the effects of the noise factors. Depending on the goal of the experiment, one of the following signal-to-noise ratios may be adopted:

“Larger is better” is chosen when experiment is aim at maximizing the response

“Nominal is best” is employed when the signal-to-noise ratio is based on standard deviations only

“Smaller is better” is for the experiment with the interest in minimizing the response

2.5.4 Performance of the Taguchi method to optimize the process parameters in research

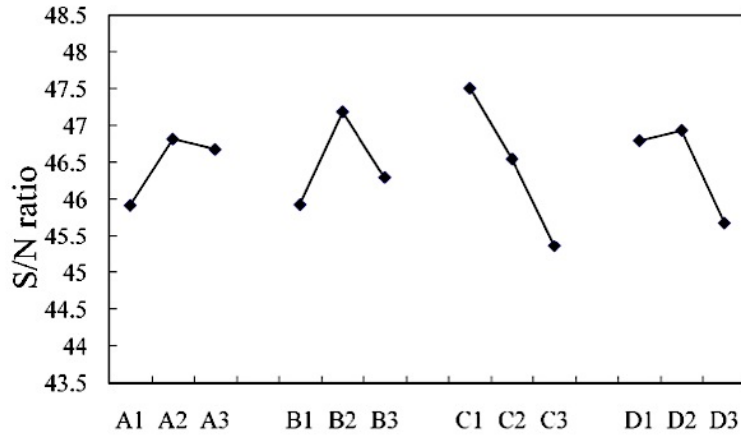
Chang [31] used the Taguchi method to optimize heat treatment process parameters for the AA7050 alloy (Table 2-2).

Table 2-2 Design of experiment using the Taguchi method. The *Hv and *Ec denote the results of S/N ratio for micro hardness and electrical conductivity, respectively [31].

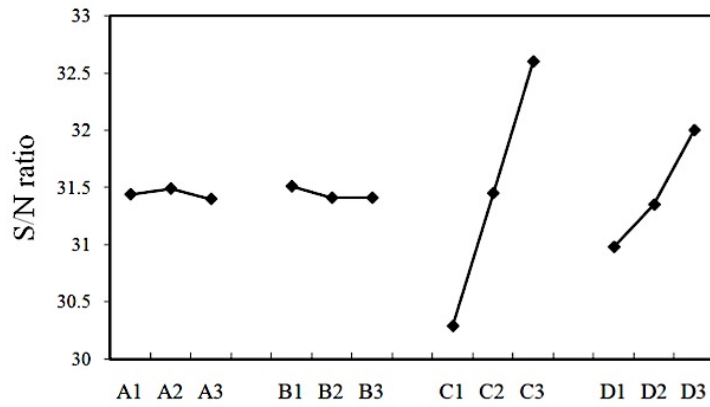
Trial No.	Heat treatment parameters				Hardness (Hv)	*Hv	EC (%IACS)	*EC
	A	B	C	D				
1	100	4	140	4	217.2	46.74	31.18	29.88
2	100	12	160	8	228.6	47.18	36.82	31.32
3	100	24	180	24	155.6	43.84	45.32	33.12
4	120	4	160	24	189.6	45.56	40.38	32.12
5	120	12	180	4	217.2	46.75	40.5	32.14
6	120	24	140	8	255.6	48.15	32.38	30.20
7	130	4	180	8	188.4	45.50	42.32	32.53
8	130	12	140	24	240.6	47.63	34.62	30.78
9	130	24	160	4	221.6	46.91	35.12	30.91

The microhardness and electrical conductivity were considered as dependent variables affected by four factors including pre-aging temperature (A), pre-aging time (B), re-aging temperature (C), and re-aging time (D).

The “larger the better” was selected to calculate the S/N ratios for hardness and electrical conductivity, since maximizing the microhardness and the electrical conductivity values was desirable. Figure 2-19 shows the main effect of each parameter level on hardness and electrical conductivity. It is observed that optimal conditions for hardness and electrical conductivity are obtained by A2B2C1D2 and A2B1C3D3, respectively. ANOVA was used to determine the percentage contribution of each factor on the microhardness and electrical conductivity [31]. It was observed that pre-aging time had the most significant contribution on the hardness, which accounted for 33.5% of the total effect. In contrast, the most influencing factor on electrical conductivity was the re-aging temperature, which accounted for 82.8% of total effect.



a



b

Figure 2-19 Main effect plots of S/N ratios showing the effects of each parameter level on:
(a) microhardness, (b) electrical conductivity [31].

3 Research hypothesis

Application of Al-Zn-Mg-Cu alloys for cast products have been limited due to casting defects such as hot tearing, which are formed during solidification especially for large size castings. Information surrounding microstructure, mechanical properties of shape cast Al-Zn-Mg-Cu alloys is scarce in the open literature.

This project focuses on the shape casting of Al-Zn-Mg-Cu alloys to address the need within the automotive industry for lightweight high strength structural cast products. The research addresses two main hypotheses:

1. Grain refinement might enable the shape casting of Al-Zn-Mg-Cu alloys by reducing their hot tearing susceptibility. Improvement of the hot tearing resistance can be achieved by delaying in the solidification coherency point. Grain refinement has been reported to effectively delay the coherency point in cast Al alloys. Moreover, grain refinement has also been reported to improve the hot tearing susceptibility by increasing the strength and ductility of semi-solid material.
2. The chemistry of Al-Zn-Mg-Cu alloys can be tailored to optimize the mechanical properties.

These two main hypotheses was tested by applying the Taguchi experimental design methodology to create nine Al-Zn-Mg-Cu alloy compositions that were shaped cast with and without the addition of the grain refiner TiBor. The specific research objectives:

1. Address the interest of automotive industry by examining the castability of Al-Zn-Mg-Cu alloys

2. Characterize the microstructure of cast Al-Zn-Mg-Cu alloys
3. Evaluate the mechanical properties of cast Al-Zn-Mg-Cu alloys
4. Finding the relationship between tensile properties and chemistry
5. Finding the relationship between mechanical properties and chemistry and introducing the alloys with highest casting quality
6. Provide information on the heat treatment response of shape cast Al-Zn-Mg-Cu alloys
7. Shape cast an automotive part using Al-Zn-Mg-Cu alloys

4 Experimental procedure

4.1 Taguchi designed experiment

4.1.1 Materials

Table 4-1 lists the factors (alloying elements) and their levels (content), which were used to design the set of alloys by the Taguchi method. The alloying elements, namely Zn, Mg, Cu and Ti were considered as the independent variables. Knowing the number of alloying elements and their contents allowed the proper selection of the orthogonal array (OA) by the Taguchi method. L₉ was the suitable orthogonal array to permit a study of the 4 alloying elements and the 3 contents, which required the casting of 9 alloys. Table 4-2 shows the chemical compositions of these 9 alloys. The Mg content range was narrower relative to Zn and Cu.

Table 4-1 Factor-level matrix for Taguchi-designed alloys

Factors	Factors levels		
	1	2	3
Zn	3.5	5	6.5
Mg	1.5	2	2.5
Cu	0	1.2	2.4
Ti	0.06	0.15	0.24

Table 4-2 Chemical compositions of the 9 Taguchi-designed alloys

Alloy No.	Zn	Mg	Cu	Ti
1	3.5	1.5	0	0.06
2	3.5	2	1.2	0.15
3	3.5	2.5	2.4	0.24
4	5	1.5	1.2	0.24
5	5	2	2.4	0.06
6	5	2.5	0	0.15
7	6.5	1.5	2.4	0.15
8	6.5	2	0	0.24
9	6.5	2.5	1.2	0.06

4.1.2 Casting process

The 9 Taguchi-designed alloys were prepared via a tilt-pour permanent mold casting process within the Light Metal Casting Research Centre (LMCRC) at McMaster University. Master alloys of Al-68Mg, Al-33Cu combined with Zn alloy (alloy#3 provided by Purity Zinc Metals) were mixed in appropriate ratios to achieve the targeted composition and melted in an electric furnace. The Al-5Ti-1B (TiBor) was also added to the mixture in an appropriate ratio as a grain refiner. TiB₂ dispersoids in addition to TiAl₃ dispersoids enhances the grain refining effect relative to TiAl₃ dispersoids alone. The melt was degassed with Ar gas for 30 min. before pouring the molten metal into the mold. The melt and mold temperatures were kept constant at 720 °C and 350 °C respectively throughout the process. Figure 4-1 shows a schematic representation of tilt-pour casting process. The molten metal is poured into the cup. The mold then rotates 90° to deliver the molten metal from the pouring cup to the casting cavity. The mold in this

case was specially designed to shape-cast two standard tensile specimens based on the ASTM B557-06 standard. All 9 Taguchi-designed alloys were cast both with and without TiBor additions (grain refinement).

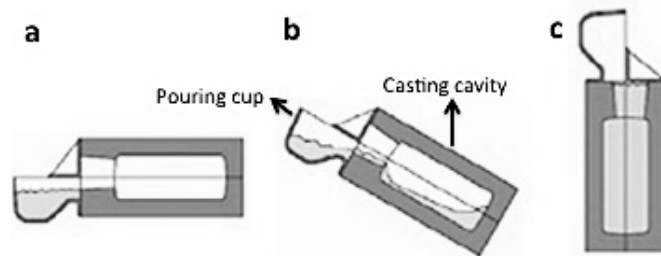


Figure 4-1 Schematic representation of tilt-pour-casting process (a) pouring, (b) tilting, and (c) solidification position.

4.1.3 Heat treatment

A double step solution treatment was used on the 9 Taguchi-designed alloys. Twelve samples of each alloy were solution treated at 450 °C for 24 h to dissolve the non-equilibrium eutectic phases as the first step. The second step involved a higher temperature that was defined by the results of thermal analysis. Table 4-3 lists solution treatment parameters for the 9 alloys. All tensile samples were naturally aged at room temperature for at least 7 days prior to tensile testing. The duration of 7 days was required to ensure the completion of the natural ageing process [25].

Table 4-3 Solution treatments of the 9 Taguchi-designed alloys

Experiments	Composition	Heat treat procedure
Alloy 1	3.5Zn-1.5Mg-0Cu-0.06Ti	450 °C (24 h.) + 475 °C (24 h.)
Alloy 2	3.5Zn-2Mg-1.2Cu-0.15Ti	450 °C (24 h.) + 485 °C (2 h.)
Alloy 3	3.5Zn-2.5Mg-2.4Cu-0.24Ti	450 °C (24 h.) + 485 °C (2 h.)
Alloy 4	5Zn-1.5Mg-1.2Cu-0.24Ti	450 °C (24 h.) + 550 °C (2 h.)
Alloy 5	5Zn-2Mg-2.4Cu-0.06Ti	450 °C (24 h.) + 470 °C (2 h.)
Alloy 6	5Zn-2.5Mg-0Cu-0.15Ti	450 °C (24 h.) + 550 °C (2 h.)
Alloy 7	6.5Zn-1.5Mg-2.4Cu-0.15Ti	450 °C (24 h.) + 470 °C (2 h.)
Alloy 8	6.5Zn-2Mg-0Cu-0.24Ti	450 °C (24 h.) + 550 °C (2 h.)
Alloy 9	6.5Zn-2.5Mg-1.2Cu-0.06Ti	450 °C (24 h.) + 475 °C (24 h.)

4.2 Characterization

4.2.1 Chemistry test and visual inspection

Each casting was visually inspected in order to ascertain the casting quality, specifically the integrity of the casting and presence of any hot tearing defects. Figure 4-2 shows a typical casting, which contains two standard tensile bars. Separate shape casting samples for composition analysis were prepared using a Cu mold (Figure 4-3). The composition analysis was conducted using the Glow Discharge Optical Emission Spectroscopy (GDOES) method. The calibration was carried out before measuring the composition.

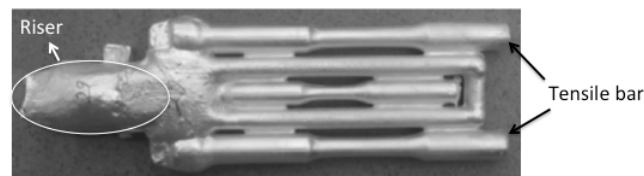


Figure 4-2 A typical permanent mould shape casting

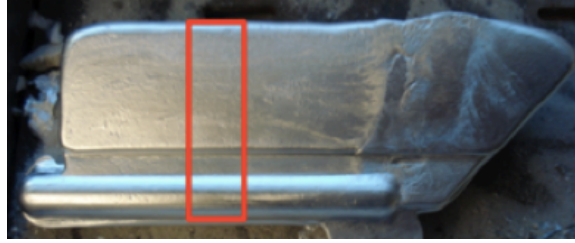


Figure 4-3 Shape cast sample for composition analysis by GDOES. Red frame identifies location of sub-section extracted for the analysis.

4.2.2 Solidification simulation

Pandat software is an integrated computational environment for phase diagram calculation based on CALPHAD (CALculation of PHase Diagram) approach. In this study, Pandat is used for simulation of the solidification characteristics. It provides information on the nature and volume fraction of the phases formed during solidification of each alloy.

4.2.3 Light optical microscopy

The as-cast microstructure of each Taguchi-designed alloy, with and without TiBor addition, was examined in cross-section using light optical microscopy. Samples were cut from a gauge section of one of the set of tensile bars cast of each alloy for this purpose. Each sample was mounted in cross-section and the surface was step-wise abraded using 240, 600 and 1200 grit SiC paper with water as a lubricant at 240 rpm with 20 N (5 lbs.) force applied. The surface was then fine polished using the following procedure:

9- μm diamond suspension on an Ultra-Pol (silk) cloth at 150 rpm under a 20 N, 5 min.

3- μm diamond suspension on a Trident cloth at 150 rpm under a 20 N loads for 4 min.

1- μm diamond suspension on a Trident cloth at 150 rpm under a 20 N loads for 3 min.

0.05- μm colloidal silica suspension on a micro cloth pad at 120 rpm under a 20 N load for 3 min..

The microstructure in each case was first examined in the as-polished condition to study the intermetallic phases that formed during the solidification. The microstructure was then examined in the as-etched condition to study the grain size and morphology. Etching was achieved electrochemically by contacting the polished surface with aqueous 1.8% fluoboric acid (Barker's Reagent) at an applied voltage of 20-45 V dc for a maximum of 2 min.. Crossed polarized light in combination with a sensitive tint (first order red plate, or λ plate) to reveal the microstructure in color. Some samples were chemically etched using Keller's reagent, which is a mixture of 1 ml. HF, 1.5 ml. HCL, 2.5 ml. HNO₃ and remainder H₂O. The linear intercept method was employed to measure the grain size in accordance to the ASTM test method E112.

4.2.4 Tensile test

Tensile testing was done using an Instron 8800 Machine (Model 312 MTS). A 50 mm gauge length extensometer coupled with an on-line data acquisition system was employed to measure the extension and strain. The crosshead speed was kept constant for all the

samples at 1 mm/min. A stress–strain curve was obtained for each replicate set of alloy samples. Average mechanical properties including the yield strength (YS), ultimate tensile strength (UTS) and elongation (El.%) were extracted from the replicate set of curves.

4.3 Statistical analysis of Taguchi designed alloys properties

Minitab 17 was employed to assist with the statistical analysis of the tensile testing results and determining the S/N ratios.

4.3.1 The S/N ratio

The S/N ratio was used to gauge the deviation between the experimental and desired value of the YS, UTS, and (EL.%) and determine the optimum combination of alloying. There are three scenarios for S/N ratio analysis: (i) larger the better, (ii) nominal the better and (iii) smaller the better. In this work larger (higher) values are desirable for the aforementioned properties, thus scenario (i) larger the better was implemented. The S/N ratio for larger the better is given by:

$$S/N \text{ ratio} = \eta = -10 \log \left(\frac{1}{n} \left(\sum_{i=1}^n \frac{1}{y_i^2} \right) \right) \quad \text{Equation 3. 1}$$

In this equation, y is the material property of interest (YS, UTS, El.% and Q) and i is the trial number.

4.3.2 ANOVA and multiple regression

Analysis of Variance (ANOVA) was used to quantitatively estimate the relative contribution that a specific alloying element has on the measured property, and expressing it as a percentage. Multiple regressions was employed on the measured data to predict the mean and weighted mean values of the YS, UTS, El.% and Q based on linear combinations of alloying elements considered. More specifically, multiple regressions was employed to learn more about the relationship between Zn, Mg, Cu and Ti (alloying elements under consideration) and the corresponding mechanical properties of the Al alloy. The multiple regression equation takes the following general form:

$$y = b_1x_1 + b_2x_2 + \dots + b_nx_n + c. \quad \text{Equation 3. 2}$$

Where $b_1, b_2 \dots b_n$ are the regression coefficients, c is a constant and x_1, x_2, x_3 and x_4 are weight percentage of Zn, Mg, Cu and Ti, respectively.

4.3.3 Verification of the models

The material property models were validated against experimentally measured values of Al-6Zn-2Mg-2Cu alloy. The validation alloy was cast into ASTM B557-06 tensile specimens using the tilt pour permanent mold process described above.

4.4 Secondary aging (SA) of Al-Zn-Mg-Cu alloys

A sub-set of the Taguchi-designed alloys with a relatively high (Alloys 2, 5 and 7) was selected to study the secondary aging (SA) response of Al-Zn-Mg-Cu alloys. The samples

were given the two-step solution treatment described earlier. All samples were then subjected to a SA treatment at 120 °C for 90 min. and then quenched to room temperature.

4.5 Artificial ageing (AA) of Al-Zn-Mg-Cu alloys

An experiment was designed in order to obtain more information on the artificial ageing response of shape cast Al-6Zn-2Mg-2Cu alloy. Figure 4-4 summarizes the artificial ageing treatment employed for this purpose. Samples were solution treated first at 450 °C for 12 h. then at 475 °C for 24 h. The samples were then quenched to room temperature and natural aged at room temperature for 24 h. before artificial ageing. Artificial ageing was carried out first at 120 °C for 24 h and then at 180 °C for another 24 h. A set of four samples was taken out of the furnace after different artificially aging times, as indicated by arrows superimposed onto Figure 4-4.

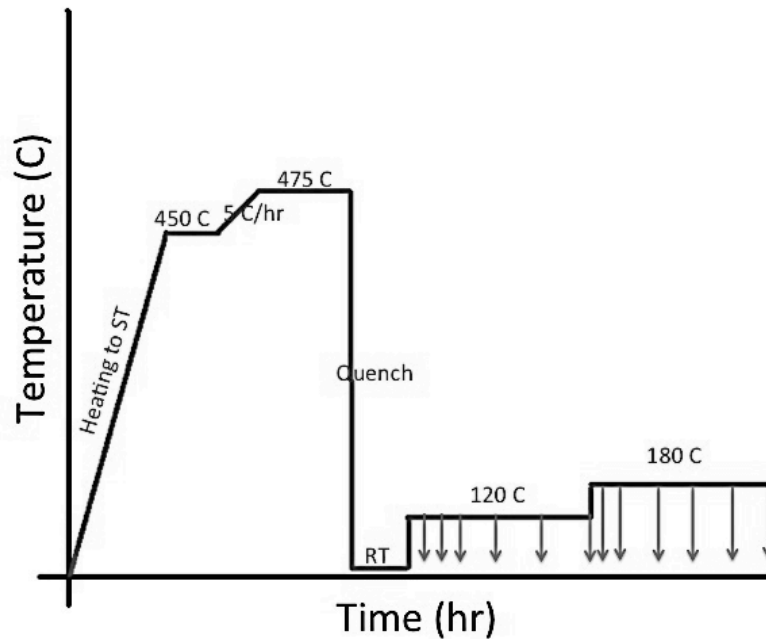


Figure 4-4 Double step ageing response of Al-6Zn-2Mg-2Cu at 120 °C and 180 °C. The arrows indicate quenching the samples after different ageing periods.

4.6 Camber link shape casting trial

A camber link pattern was used to evaluate the feasibility of shape casting an automotive part via the conventional sand mold process. Figure 4-5 shows the camber link part after the casting in the sand mold. The camber link casting was comprised of two main parts. ASTM B557-06 tensile samples were cut from each part, solution treated at 475 °C for 24 h and tested after 7 days (168 h) of natural ageing at room temperature. Typical locations of the tensile samples are shown in Figure 4-6. A number was assigned for each tensile sample to monitor the degree to which the casting location affected the tensile properties.

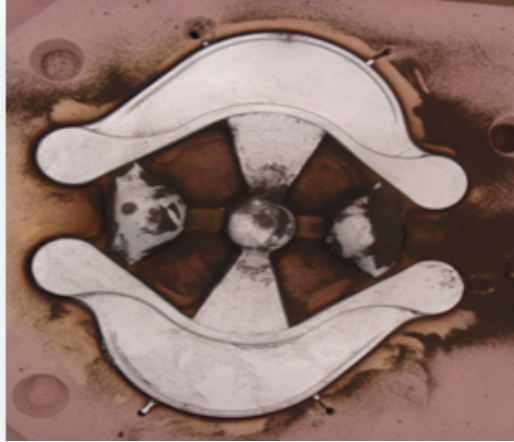


Figure 4-5 Sand mould shape casting of Al-6Zn-2Mg-2Cu alloy: camber link part.



Figure 4-6 Locations of the tensile samples cut from the camber link.

5 Results and discussion

5.1 Characterization of the 9 Taguchi-designed Al-Zn-Mg-Cu alloys

5.1.1 Chemical composition

The results of the chemical composition analysis of the 9 Taguchi-designed alloy castings with and without the TiBor addition are presented in Table 5-1. Inspection of Table 5-1 reveals that the alloying content was within the desired range for each all (c.f. Table 4-2). The Si content in each alloy was limited to below 0.025 % and the Fe content in each alloy was varied between 0.03 and 0.08 %.

Table 5-1 Composition (wt.%) of the 9 alloy castings determined using GDOES

<i>Alloy</i>	<i>Zn</i>	<i>Mg</i>	<i>Cu</i>	<i>Ti</i>	<i>Fe</i>	<i>Si</i>
Alloy 1 No Ti	3.12	1.35	0.02	–	0.04	0.01
Alloy 1 + Ti	3.21	1.41	0.02	0.05	0.06	0.02
Alloy 2 No Ti	3.41	1.94	1.26	–	0.04	0.02
Alloy 2 + Ti	3.16	1.82	1.16	0.18	0.05	0.02
Alloy 3 No Ti	3.55	2.46	2.71	–	0.06	0.02
Alloy 3 + Ti	3.40	2.35	2.69	0.22	0.07	0.02
Alloy 4 No Ti	5.10	1.59	1.31	–	0.05	0.02
Alloy 4 + Ti	4.82	1.52	1.27	0.18	0.06	0.02
Alloy 5 No Ti	5.18	2.01	2.67	–	0.06	0.02
Alloy 5 + Ti	4.81	2.00	2.66	0.09	0.07	0.02
Alloy 6 No Ti	5.03	2.33	0.02	–	0.05	0.02
Alloy 6 + Ti	4.66	2.11	0.02	0.12	0.04	0.02
Alloy 7 No Ti	6.61	1.52	2.61	–	0.06	0.02
Alloy 7 + Ti	6.02	1.38	2.12	0.57	0.05	0.02
Alloy 8 No Ti	6.35	1.86	0.02	–	0.04	0.01
Alloy 8 + Ti	6.00	1.78	0.02	0.26	0.05	0.02
Alloy 9 No Ti	6.57	2.33	1.26	–	0.05	0.02
Alloy 9 + Ti	6.42	2.32	1.27	0.06	0.05	0.02

5.1.2 Visual inspection

All the castings were subjected to a visual inspection prior to further examination in order to qualitatively ascertain the casting quality, specifically the integrity of the casting and presence of any visible defects. Selected images showing the typical appearance of the alloy castings after ejection from the mould are presented in Figure 5-1. Visual inspection of the alloys without the TiBor addition (grain refinement) revealed hairline cracks in the runners and the gauge section of fatigue bar (middle bar), as shown in Figure 5-1-a. Similar cracking was observed in the vicinity of grip section of the tensile bar. Similar visible defects were not observed by visual inspection of the alloys with the TiBor addition (grain refinement), as shown in Figure 5-1-b. In general, the TiBor addition (grain refinement) improved the casting quality in this regard.

The presence of hairline cracks was likely due to the occurrence of hot tearing during the last stages of solidification. The interdendritic regions were the last regions of the microstructure to solidify, thus they likely contained traces of low melting temperature eutectic phases on the grain boundaries [32, 33]. These eutectic phases, along with already present shrinkage pores, likely assisted hot tearing crack propagation. Cracks likely initiated when the thermal stress (due to solidification contraction) exceeded the semi-solid strength of the alloy and then propagated towards damaged regions within the casting: regions with high interdendritic porosity for example. Nevertheless, hairline cracks could have formed during subsequent thermal contraction upon cooling to room temperature due to presence of weak sub-surface regions such as pores and blisters [32, 33].



Figure 5-1 Image showing the typical appearance of the alloy castings (a) without the TiBor addition (Alloy 7) and (b) with the TiBor addition (Alloy 7) Red frames document the locations of visible cracks.

The improved casting quality associated with the addition of TiBor (grain refinement) is consistent with reported studies. Warrington et al. [4] reported that moderate addition of a grain refiner (TiBor) improved the hot tearing resistance of Al-Zn-Mg-Cu (AA7010 and AA7050) alloys. It was suggested that the grain refinement improves the feeding by delaying the coherency point, thereby reducing the hot tearing resistance. Sufficient liquid feeding reduces the extent of tension on the critical regions in the last stages of

solidification [32, 33].

In the alloys without the TiBor addition, the dendrite growth rate was likely high, the volume fraction of dendrites likely increased quickly and the time required to reach the coherency point was likely shorter. The addition of TiBor likely decreased the dendrite growth rate, decreased the volume fraction of dendrites and increased the time required to reach the coherency point. In the other words, the fraction of the solid at the coherency point likely increased in the alloys with the TiBor addition, which served to reduce the hot tearing resistance.

5.1.3 As-cast microstructure

Figure 5-2 shows the typical microstructure of the as-cast Al-Zn-Mg-Cu alloys. Figure 5-2-a reveals that the alloys without the TiBor addition exhibited a large equiaxed-dendritic structure. The formation of an equiaxed dendritic structure can be achieved through different methods including: (i) rapid cooling, (ii) melt agitation, (iii) solute concentration and (iv) grain refining [34]. During solidification of the cast alloys without the TiBor addition, the rejection of the solutes ahead of the solid-liquid interface likely caused constitutional undercooling, which in turn increased the number of nuclei. The growth of numerous equiaxed dendrites then suppressed columnar growth. The solute concentration also could have reduced dendrite growth by affecting the growth restriction factor [34]. The pre-heated mold during the casting process (slow cooling) likely affected the size of the grains. In general, the number of nuclei was likely reduced in the slowly cooled melt because of the small degree of undercooling. Therefore, dendritic growth of the produced

nuclei resulted in a large grain size. A rapid cooling cycle (cold mold) with a large degree of undercooling could have increased the number of nuclei and, thus reduced the size of the resulting dendrites

As can be seen in Figure 5-2-b, the addition of TiBor to the alloy resulted in significant grain refinement and changed the microstructure from an equiaxed-dendritic one to an equiaxed granular one. This observation is not entirely consistent with the observations reported by Warrington et. al. [4] in which the small addition of Ti grain refiner (0.02%) led to a rosette-like or cellular-like granular structure [4]. This disagreement in grain morphology might be due to differences in casting processes and/or cooling rates employed. For a given Ti content, an increase in the cooling rate serves to decrease the secondary dendrite arm spacing (SDAS), which causes a change in the grain morphology from spherical to equiaxed-cellular [35]. It is assumed that the low cooling rate employed in this study (pre-heated mold) had a significant effect on the resultant grain structure in addition to the grain refining effect.

Figure 5-3 shows the effect of the TiBor addition on the grain size of the cast alloys. It is clear that the addition had a significant influence on the grain size, inducing a marked reduction in each case.

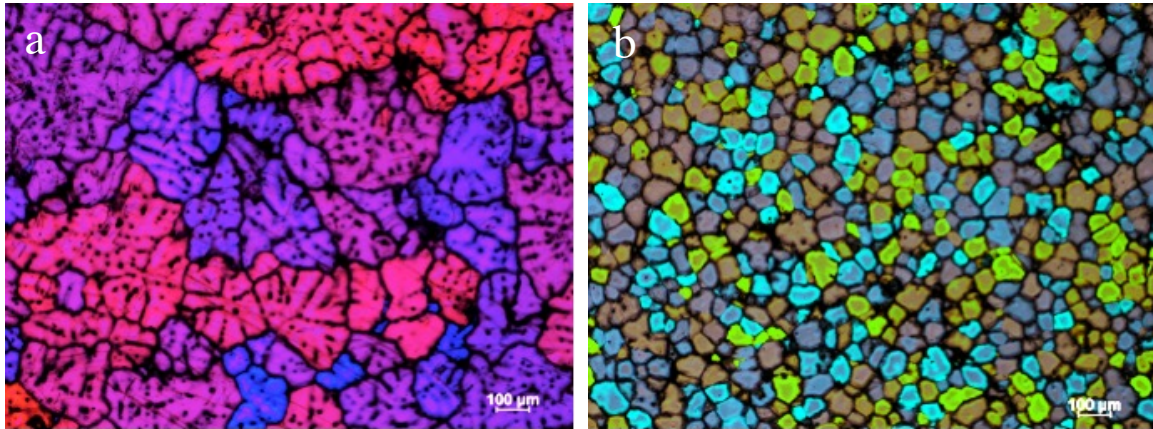


Figure 5-2 Typical grain structure of the as-cast Al-Zn-Mg-Cu alloys (a) without TiBor addition (Alloy 7) and (b) with TiBor addition (Alloy 7).

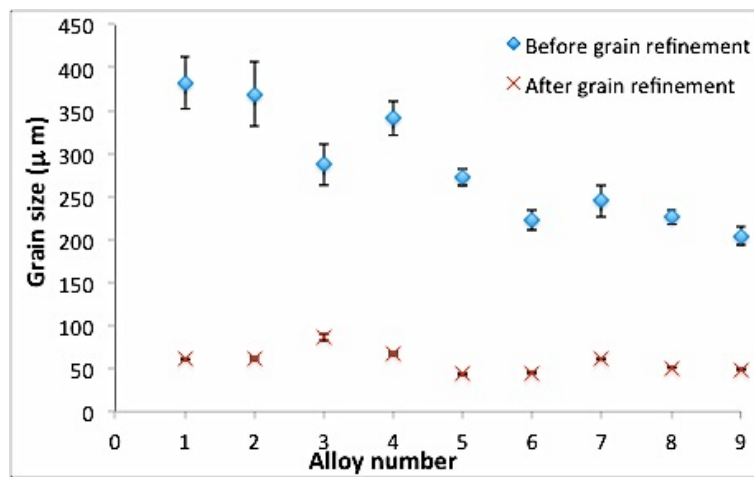


Figure 5-3 Effect of TiBor addition on the grain size of the 9 Taguchi alloys. Error bars represent 95% confidence interval.

In order to understand the solid-state phase transformation during the solution treatment, information is required on the morphology, stability and chemistry of the constituent

phases present in the as-cast condition. Pandat predictions of the type and amount of phases formed during non-equilibrium solidification of 9 Taguchi alloys are presented in Table 5-2. It is observed that Mg (ZnCuAl)₂, Al₇Cu₂Fe, Al₂Cu, Al₂CuMg and Mg₂Si are the main grain boundary phases formed during non-equilibrium solidification of these alloys. According to the Pandat predictions, the Cu-containing Mg (ZnCuAl)₂ with 1.4% is the dominant eutectic phase expected in the as-cast Al-3.5Zn-2Mg-1.2Cu alloy. The Fe-containing Al₁₃Fe₄ phase is also predicted by Pandat. This is consistent with literature where four major eutectic phases are reported in the as-cast microstructure of the Al-Zn-Mg-Cu system alloys [7, 8], hexagonal η (MgZn₂), cubic T (Al₂Mg₃Zn₃), orthorhombic S (Al₂CuMg), tetragonal Θ (Al₂Cu). Figure 5-4 shows the typical microstructure of the Al-3.5Zn-2Mg-1.2Cu alloy, which consists of Cu and Fe containing phases in Al matrix.

Table 5-2 Pandat predictions of the type and amount of formed phases during non-equilibrium solidification of the 9 Taguchi-designed alloys

Expts	Eut.	Sigm	Al ₂ Cu	T	Mg ₂ Si	Al ₁₃ Fe ₄	S	Al ₃ Ti	Al ₇ Cu ₂ Fe	Al ₅ Cu ₂ Mg ₈ Si ₆
Alloy 1	1.3	0.1	0	0.9	0.12	0.08	0	0	0	0
Alloy 2	2.6	1.4	0	0.3	0.1	0.1	0.3	0.15	0	0
Alloy 3	9	4	3.8	0	0	0.2	0	0.7	0.02	0.03
Alloy 4	2.7	1.8	0.16	0	0.02	0.09	0	0.3	0	0.1
Alloy 5	3.7	2.8	0.6	0	0.1	0.09	0.03	0	0	0
Alloy 6	0.5	0	0	0	0	0.2	0	0.3	0	0
Alloy 7	4	2.7	0.6	0	0.03	0.09	0	0.2	0	0.9
Alloy 8	1.1	0	0	0	0	0.17	0	0.8	0	0
Alloy 9	3.6	2.5	0	0.5	0.1	0.09	0.2	0	0	0

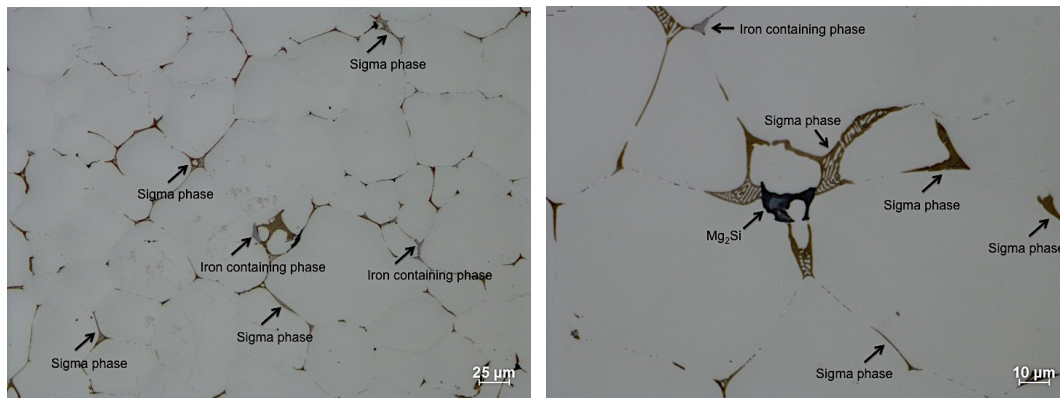


Figure 5-4 Typical morphology of the eutectic phases in the as-cast Alloy 2 (Al-3.5Zn-2Mg-1.2Cu): (a) 200x, (b) 500x.

Light optical micrographs of un-etched as-cast alloy samples show a distribution of porosity in addition to the eutectic phases (Figure 5-5). Grain boundary phases were found to reside within the interdendritic region of the as-cast alloys without the addition of TiBor. Figures 5-5-a and 5-5-c show isolated clusters of interconnected shrinkage porosity. Figures 5-5-b and 5-5-d show that the refining the grain size through the addition of TiBor resulted in the dispersion and refinement of the porosity. The presence of relatively smaller porosity in the grain-refined microstructure suggests an improved feeding, which would compensate for the volumetric contraction thereby preventing formation of large hot pores. However, in some regions of grain-refined alloys, interdendritic feeding remained difficult and isolated shrinkage pores were formed (Figure 5-5-d). The formation of porosity is closely related to the extent of the freezing range and, thus to the alloy composition. In general, Al-Zn-Mg-Cu alloys with long solidification ranges tend to form dispersed, interdendritic or intergranular micropores, compared to alloys with short freezing ranges such as Al-Si alloys, which show

propensity for formation of more localized macro-shrinkage or larger intergranular pores [32, 33].

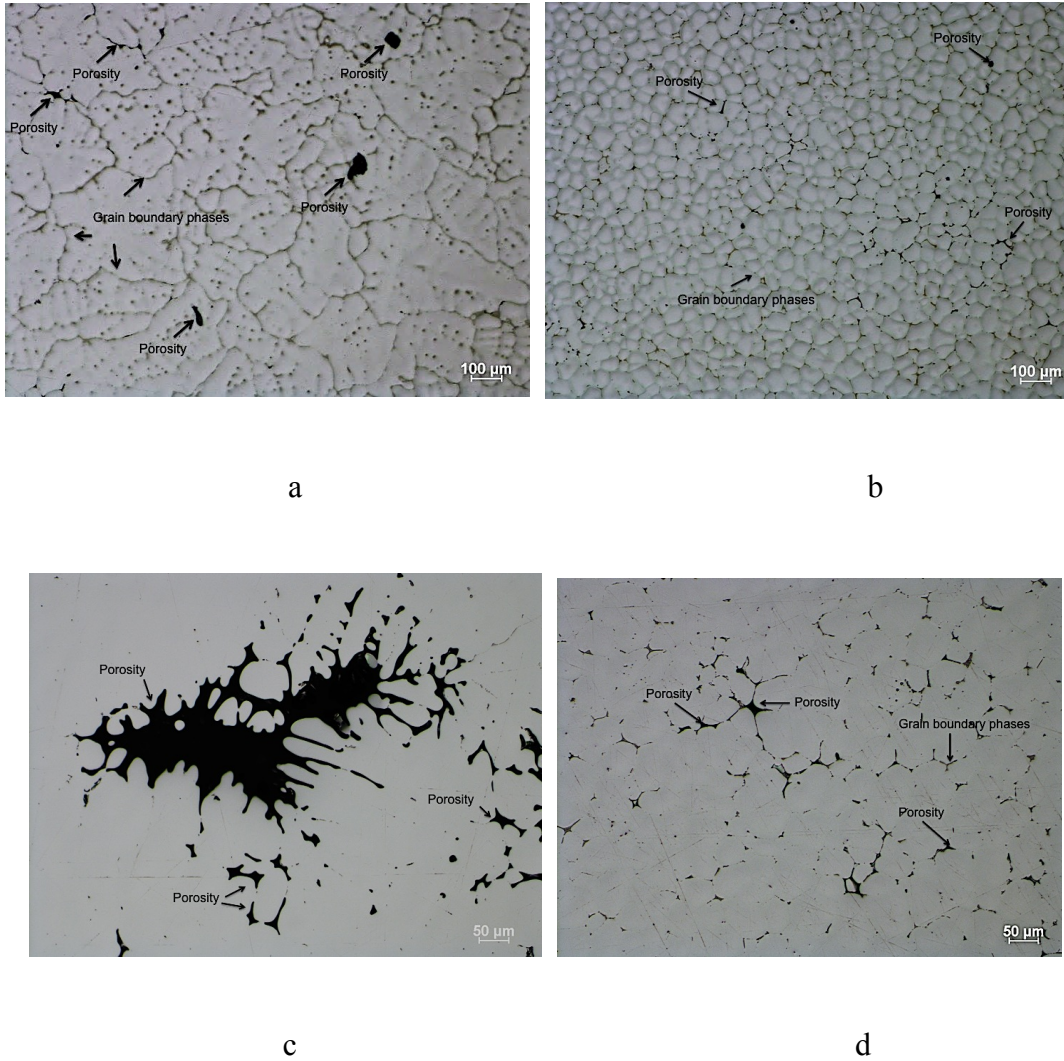


Figure 5-5 Typical light optical micrographs of the un-etched as-cast Al-Zn-Mg-Cu alloys: (a) without TiBor addition (Alloy 2: Al-3.5 Zn-2 Mg-1.2 Cu), (b) with TiBor addition (Alloy 2: Al-3.5 Zn-2 Mg-1.2 Cu alloy), (c) without TiBor addition (Alloy 1: Al-3.5 Zn-1.5 Mg), (d) with TiBor addition (Alloy 6:Al-5 Zn-2.5 Mg Cu).

5.2 Statistical analysis of tensile properties

The mechanical properties of Taguchi designed alloys were studied in the naturally-aged (NA) condition. This section presents the results obtained after applying a two-step solution treatment to each alloy. Figure 5-6 shows a set of replicate curves for alloy 2.

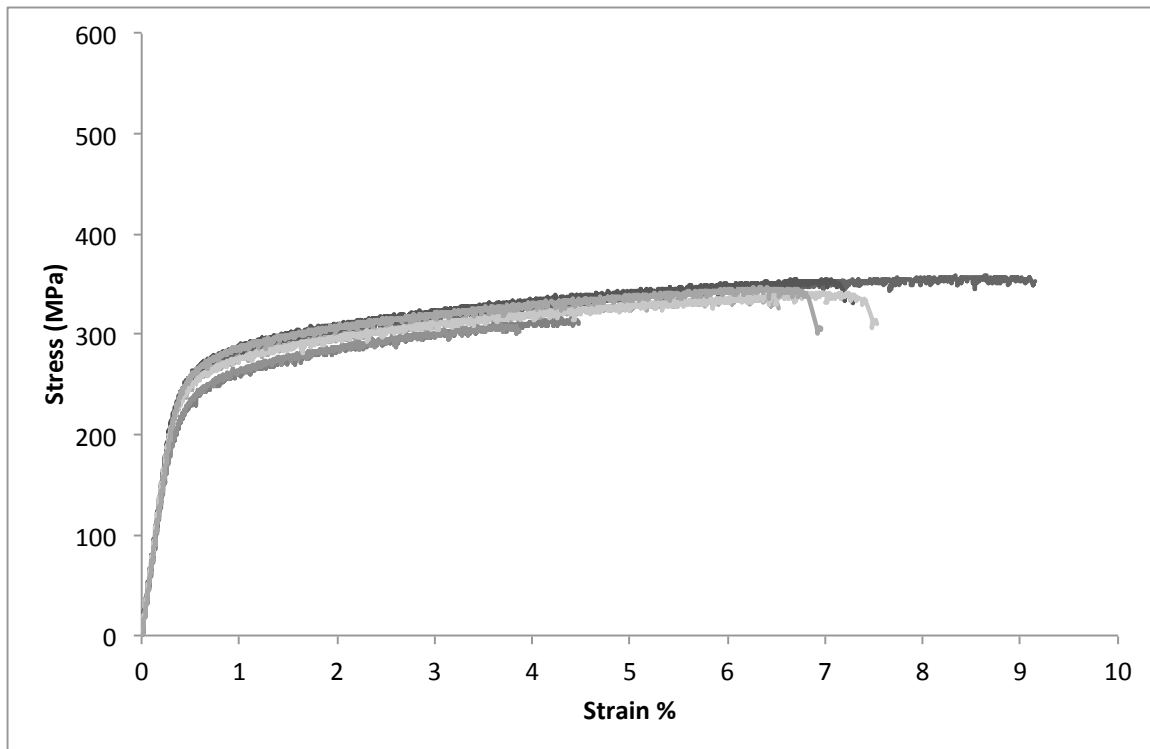


Figure 5-6 A set of replicate Engineering stress-strain curves for alloy 2

These curves are plotted for each alloy and tensile properties are measured. The mean values of the YS, UTS, El.% are presented in the appendix. Multiple linear regression analysis was used to derive equations that relate the chemical composition of the alloys to their mechanical properties. Using multiple linear regression analysis, the discrete experimental data was fit to a curve and a model was derived, which represents the

general trend of the data. The multiple regression models developed to predict mean El.%, UTS, and YS are given below:

$$\text{Mean El.\%} = 26.6 - 1.01 (\text{Zn \%}) - 7.48 (\text{Mg \%}) + 2.4 (\text{Cu \%}) - 11.9 (\text{Ti \%}) \quad (1)$$

$$\text{Mean UTS} = 134 + 22.6 (\text{Zn \%}) - 4.7 (\text{Mg \%}) + 82 (\text{Cu \%}) - 136 (\text{Ti \%}) \quad (2)$$

$$\text{Mean YS} = -86.9 + 32.2 (\text{Zn \%}) + 47.5 (\text{Mg \%}) + 45.5 (\text{Cu \%}) - 31.7 (\text{Ti \%}) \quad (3)$$

Minitab was used to calculate the S/N ratios for the tensile properties (YS, UTS, El.%). Similar equations were obtained for the prediction of the S/N ratios. Standard deviation was taken into account in order to place more emphasis on the observation with small variance and model the weighted mean values of YS, UTS, and El.%. Statistical models were used to predict the mean and weighted mean values of YS, UTS, and El.%.

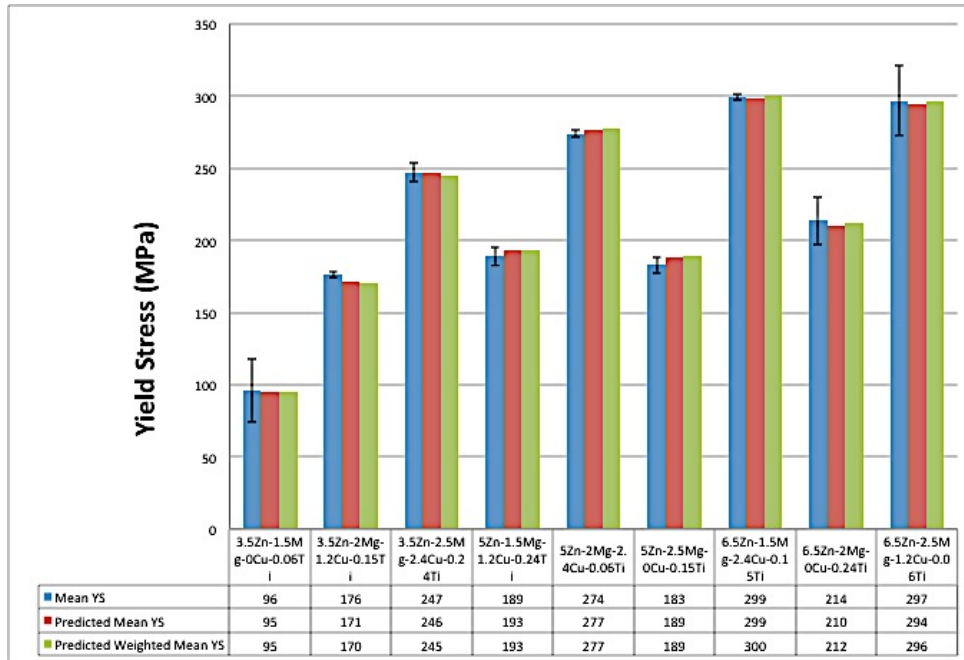
$$\text{Weighted Mean El.\%} = 26.3 - 0.89 (\text{Zn \%}) - 7.5 (\text{Mg \%}) + 2.09 (\text{Cu \%}) - 9.6 (\text{Ti \%}) \quad (5)$$

$$\text{Weighted Mean UTS} = 137 + 24.2 (\text{Zn \%}) - 10.23 (\text{Mg \%}) + 83.86 (\text{Cu \%}) - 153 (\text{Ti \%}) \quad (6)$$

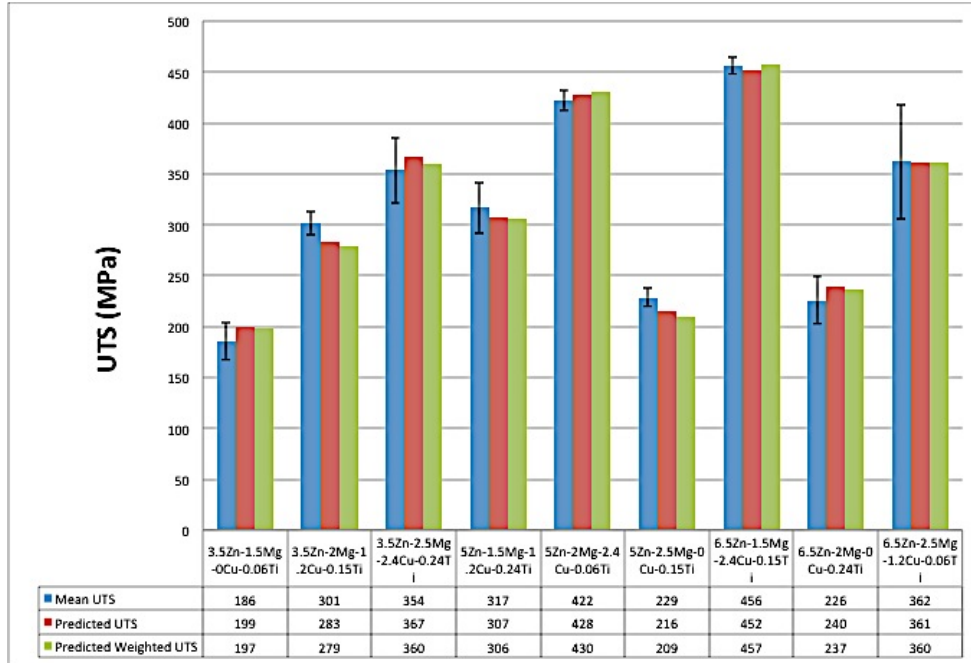
$$\text{Weighted Mean YS} = -89.43 + 33.05 (\text{Zn \%}) + 47.5 (\text{Mg \%}) + 45.5 (\text{Cu \%}) - 35.2 (\text{Ti \%}) \quad (7)$$

The experimental and predicted values of the properties for the 9 Taguchi alloys are compared in Figure 5-7. Considering the YS values, Alloy 7 (299 MPa), Alloy 9 (297 MPa), Alloy 5 (274 MPa) and Alloy 3 (247 MPa) showed the highest strength. The El.% values of Alloy 7 (14%) and Alloy 5 (11%) were promising. However, Alloy 9 and Alloy 3 showed poor performance during plastic deformation and failed at low strain values of 3% and 6%, respectively. Among the alloys with 1.2% Cu, Alloys 2 and 4 possessed high El.% values of 12% and 11%, respectively. However, their YS values were relatively low. The Cu-free alloys exhibited inferior properties. It is noted that Alloy 7 (6.5Zn-

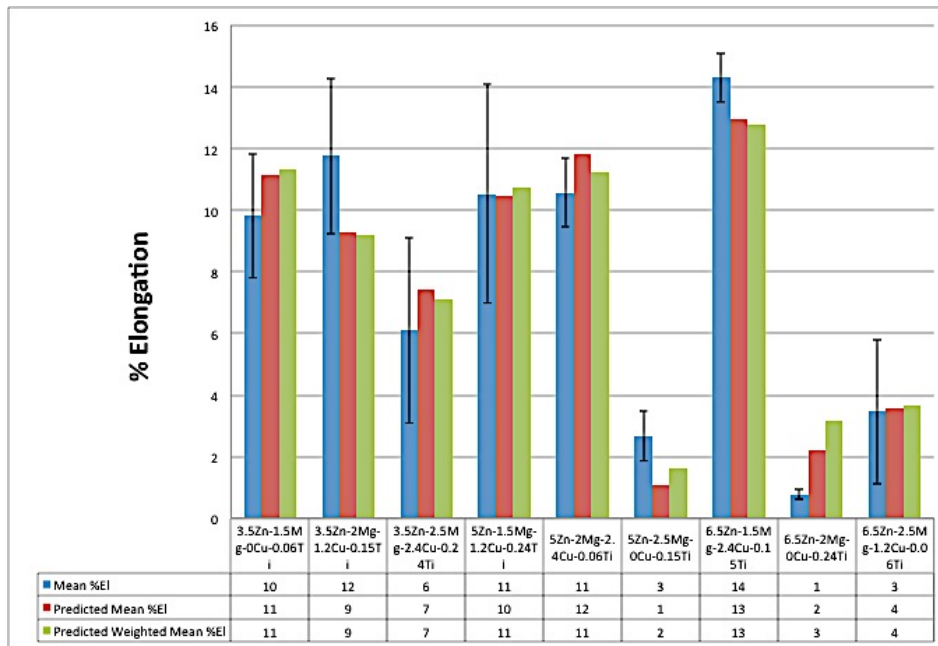
1.5Mg-2.4Cu-0.15Ti) exhibited the highest YS (299 MPa), UTS (456 MPa), and El.% (14%) values among the set of Taguchi-designed alloys. The next best alloy in terms of quality was the Cu-containing Alloy 5.



a



b



c

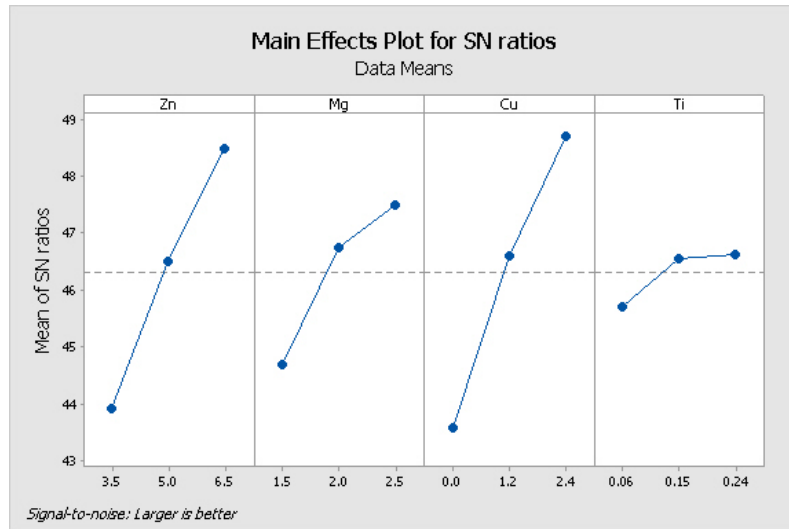
Figure 5-7 Mean, predicted mean and weighted mean values of YS, UTS, and El.% of the 9

Taguchi-designed alloys with TiBor addition in the NA condition.

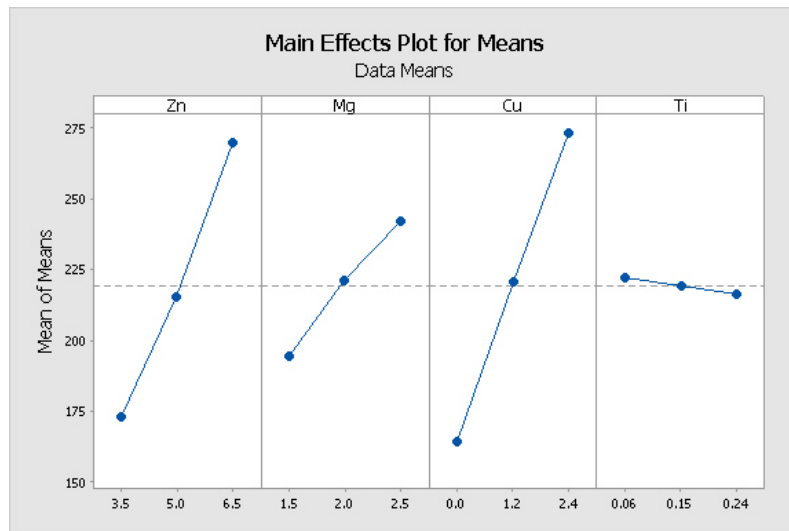
5.2.1 Main effect plots and percentage contribution

The main effect plots for YS show that it was significantly affected by the Cu content (46% of the total effect), followed by the Zn content (36 % of total effect) and then the Mg content (9.8% of the total effect) (Figure 5-8). A greater S/N value corresponds to a better performance. Based on the analysis, the alloy with the maximum YS (predicted value of 343 MPa) would require 6.5% Zn (level 3), 2.5% Mg (level 3), 2.4% Cu (level 3), and 0.24%Ti (level 3). For the UTS, Cu showed the highest percentage contribution with 89% of the total effect, followed by Zn with 8.9% (Figure 5-9). The influence of the Mg and Ti levels on the UTS was relatively insignificant. Based on the analysis, the alloy with the maximum UTS (predicted value of 449 MPa) would require 6.5% Zn (level 3), 2.0% Mg (level 2), 2.4% Cu (level 3) and 0.15% Ti (level 2).

Mg (35% of total effect) had the most significant effect on the variation of El.%, followed by Cu (26% of total effect), then Zn (23% of total effect) and then Ti (15% of total effect), as shown in Figure 5-10. Unlike the case for YS and UTS, all four main elements studied significantly influenced the El.% value. The alloy with the maximum El.% would require 3.5 % Zn (level 1), 1.5 % Mg (level 1), 2.4 % Cu (level 3) and 0.24 % Ti (level 2). The predicted value of the El.% is 14.9%.

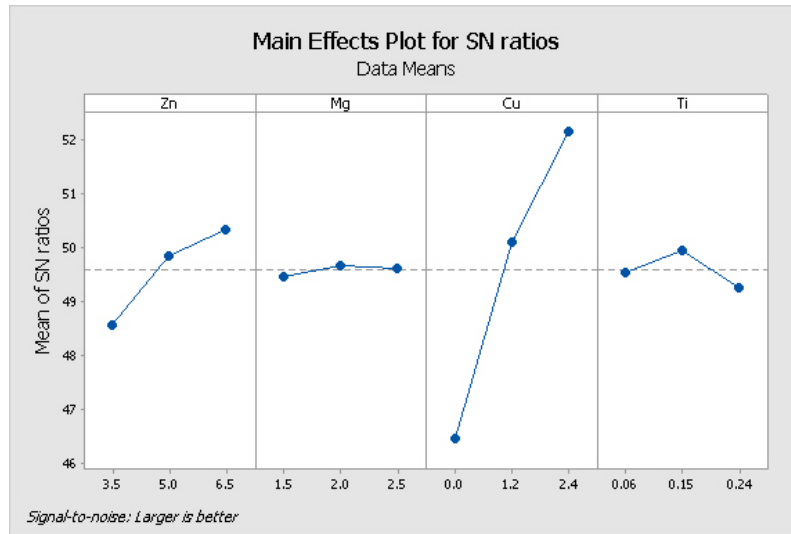


a

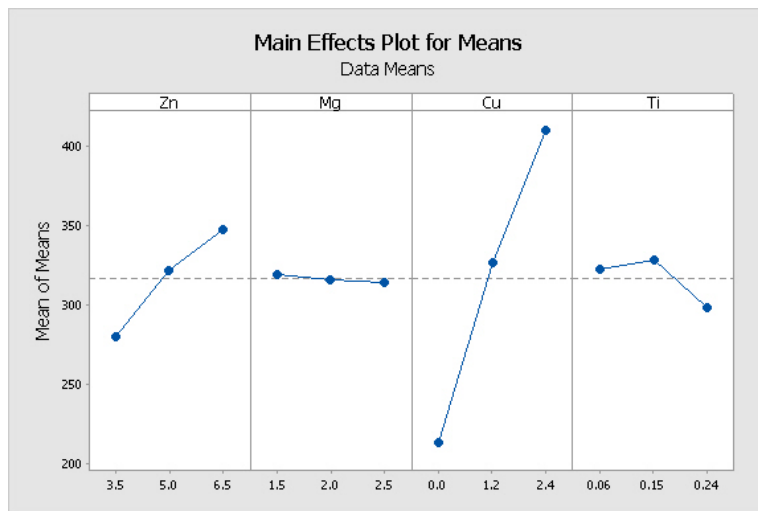


b

Figure 5-8 Main effect plots showing the effect of alloying elements on S/N and Mean values: (a) S/N ratios for YS, (b) Mean for YS.

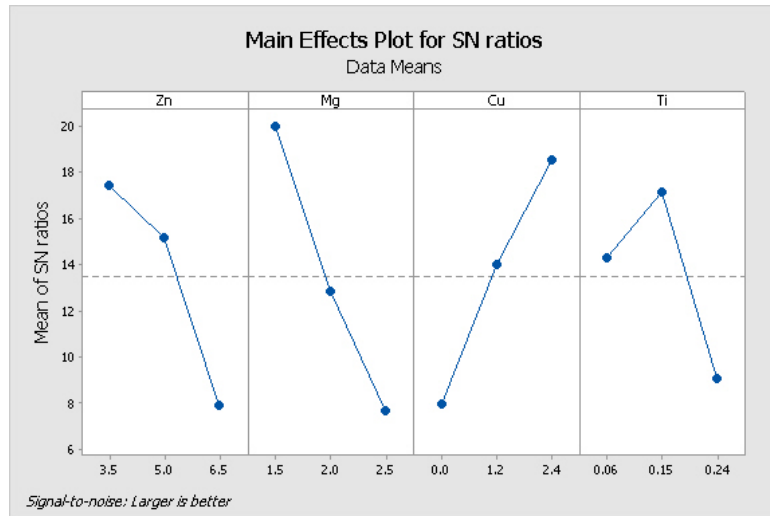


a

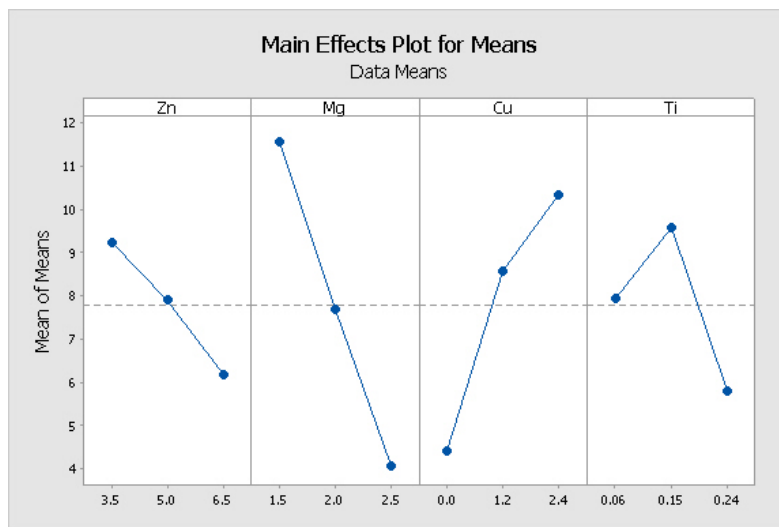


b

Figure 5-9 Main effect plots showing the effect of alloying elements on S/N and Mean values: (a) S/N ratio for UTS, (b) Mean for UTS.



a



b

Figure 5-10 Main effect plots showing the effect of alloying elements on S/N and Mean values: (a) S/N ratio for El.%, (b) Mean for El.%.

Table 5-3 lists the R square values, which reflect the performance of the models in accurate prediction of the properties. Collectively, the high R-square values show that these models estimated the mean and weighted mean values of the YS, UTS, El.% and Q with a relatively high degree of fit for the set of alloying elements and composition ranges under study.

Table 5-3 R-square and Adjusted R-square values of the models

	R Sq.	Adj. R Sq.
Mean YS	99.7%	99.4%
Mean weighted YS	99.9%	99.8%
Mean UTS	98.0%	96.0%
Mean weighted UTS	98.0%	96.0%
Mean El.%	90.0%	80.0%
Mean weighted El.%	85.0%	70.0%

The experimentally-determined tensile properties of the Al-6Zn-2Mg-2Cu validation alloy are presented in Table 5-4. The actual chemistry of the alloy, as measured using GDOES, was Al-6.1Zn-2.0Mg-2.3Cu-0.06Ti. Table 5-5 compares the experimentally-determined tensile properties with those predicted using the models. The predicted mean values of YS (308 MPa) and predicted weighted mean values of YS (310 MPa) are very close to the experimentally-determined YS.

Table 5-4 Experimentally measured YS (MPa), UTS (MPa), El.% and Q

(MPa) for Al-6Zn-2Mg-2Cu Alloy

Experimental performance characteristics		
Mean YS (MPa)	Mean UTS (MPa)	Mean El.%
303	443	12.6

Table 5-5 Predicted properties of the verification alloy.

Prediction of Performance Characteristics								
UTS(MPa)			YS(MPa)			El. (%)		
S/N	Mean	w.	S/N	Mean	w.	S/N	Mean	w.
53.0	447.0	451.0	50.0	308.0	310.0	18.0	10.7	10.3

In order to study the role of the Cu content on the final properties of cast Al-Zn-Mg-Cu alloys, its contributions on both casting quality and ageing response needs to be taken into account. In terms of its role on the ageing response, it is reported that increasing the Cu stimulates a finer and denser population of GP precipitates and thereby improves the precipitation strengthening of Al-Zn-Mg-Cu alloys [30]. The role of Cu on strength and elongation of cast Al-Zn-Mg-Cu alloys has been studied by ALCOA [36]. It is reported that increasing the Cu content has improved the strength of pressure riserless cast Al-Zn-Mg-Cu alloys which is consistent with our results. However, the elongation values in pressure riserless cast Al-Zn-Mg-Cu alloys do not show much change in the Cu range of 0.4-0.9 %, while our results shows the significant contribution of Cu on increasing the elongation values (26%). The noted difference with respect to the effect of Cu on elongation can be attributed to the difference in casting processes. Increasing the Cu content to greater than about 1.2 wt. % is reported to decrease the alloy's ductility due to an excess of constituent particles of AlFeCu at the grain boundary. Despite this, It has

been observed in our study that Cu has a huge role on improvement of the casting quality and elongation in the permanent mould cast Al-Zn-Mg-Cu alloys which its thorough understanding requires further investigation on effect of Cu on the solidification characteristics of these alloys.

5.3 Study of Al-6Zn-2Mg-2Cu alloys

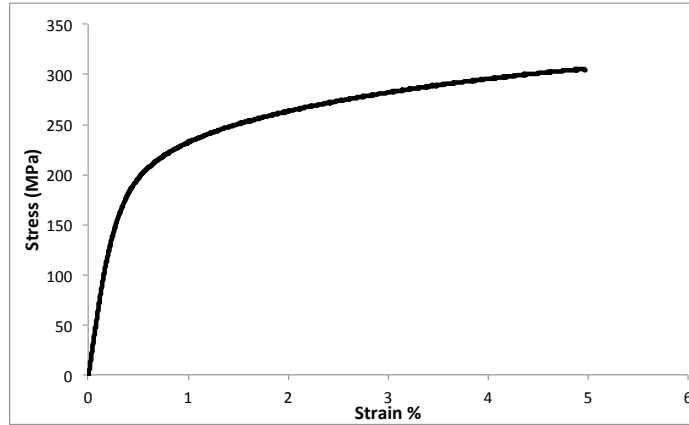
Optimized alloy Al-6.5Zn-1.5Mg-2.4Cu-0.06Ti was problematic to the industrial partner because of the relatively Cu content and the anticipated increased localized corrosion susceptibility. To address this concern, the validation alloy was selected for the study of heat treatment effects on mechanical properties.

The effect of heat treatment on the mechanical properties of a AA7xxx shape casting was conducted using an Al-6Zn-2Mg-2Cu-0.25Ti alloy composition. Heat-treated conditions under consideration included the as-cast, naturally-aged and artificially-aged conditions. A typical tensile curve of the shape-cast alloy in the as-cast condition is shown in Figure 5-12. The as-cast YS was 194 MPa, the fracture stress was 305 MPa and the fracture strain was 5 %. Figure 5-13 shows typical stress-strain curve of NA alloy. It is observed that the tensile properties have improved significantly compared to the as-cast alloy. The YS, UTS and El.% are 320 MPa, 437 MPa and 10.6%, respectively.

The microstructure of natural aged Al-Zn-Mg-Cu alloys features the distribution of coherent GP precipitates within the matrix with a spherical shape, which is the main contributor for the increase in strength of the material. Following solution treatment at elevated temperature and quenching, the material is unstable and decomposes at room

temperature, i. e. GP zones form within the Al matrix during a relatively short-time exposure. Berg [21] reported that spherical shape GP zones in Al–Zn–Mg–Cu alloys form in the temperature range of from room temperature up to 140 °C, are fully coherent with the Al matrix. Prior study of precipitation in Al-6.29Zn-2.2Mg-2.2Cu shows formation of the small clusters of solutes in the first 1.5 h. of natural ageing, which eventually evolves into GP [24].

The main alloying elements Zn, Mg, Cu play significant role during formation and growth of GP precipitates in Al–Zn–Mg–Cu alloys. It is suggested that migration of Mg is the limiting factor in formation of GP, while migration of Zn controls the GP growth. The presence of Cu promotes a higher hardening rate of the material in the first stages of precipitation [24].



b

Figure 5-11 Typical tensile curve of the shape-cast Al-6Zn-2Mg-2Cu-0.25Ti alloy in the as-cast condition.

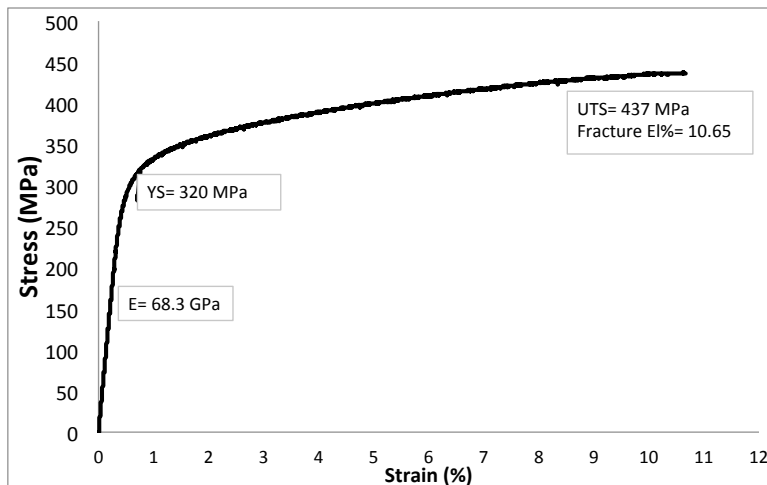
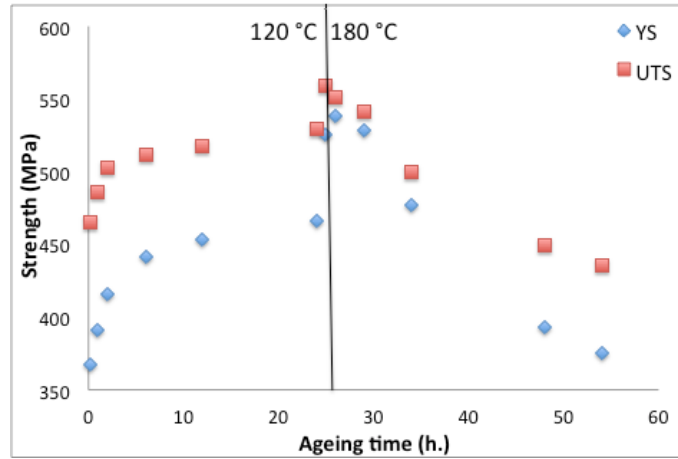


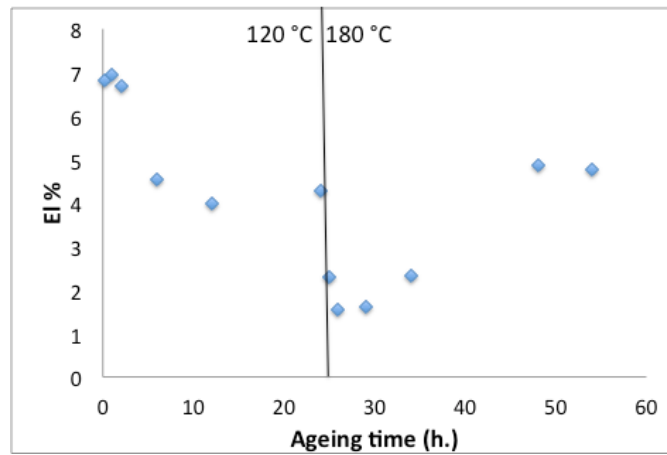
Figure 5-12 Typical tensile curve of the shape-cast Al-6Zn-2Mg-2Cu-0.25Ti alloy in the NA condition.

Figure 5-14 shows the artificially ageing response of the shape-cast Al-6Zn-2Mg-2Cu-

0.25Ti alloy at 120 °C and 180 °C. Samples were tested after different ageing time 15 min., 1 h., 2 h., 6 h., 12 h. and 24 h. at 120 °C.



a



b

Figure 5-13 Artificially ageing response of the shape-cast Al-6Zn-2Mg-2Cu alloy at 120 °C and 180 °C: (a) Strength (YS & UTS), (b) El.%.

The temperature of the furnace was then raised to 180 °C, which resulted in peak strength after an additional 2 h. As the ageing time increase further, the YS and UTS decreases and the El% increases: representative of an over-aged condition.

Diffusion rate increases with increasing the temperature. Therefore, the ageing response at room and elevated temperatures differ. Comparing the NA and AA conditions show that the mean YS and El.% values change from 314 MPa and 9.5 %, respectively, for the NA condition to 366 MPa and 6.8 %, respectively, after 15 min. of ageing at 120 °C. Ageing at 120 °C resulted in a significant increase in the strength (YS & UTS) during the first 2 h, thereafter a much less significant increase in the strength occurred during the next 22 h. The cause of the precipitation strengthening of this shape cast Al-6Zn-2Mg-2Cu-0.25Ti alloy is expected to be the same as that for wrought AA7xxx alloys: the initial precipitation of GP zones and the subsequent transformation of these zones into the η' phase. Clusters form subsequent to quenching from the solution treatment temperature, which are technically regions of Mg-vacancy segregation. This cluster formation produces local strain, thereby increasing the strength of alloy. With additional ageing time, the strength increases further as the clusters grow by absorbing Zn atoms to create an internal ordering of Zn and Al/Mg on the $\{001\}_{Al}$ planes. This structure is known as a GP zone, which is a coherent precipitate. The coherent GP zone produces an increased strain field in the matrix and causes a further increase in strength. The microstructure of the alloy in the early stages of ageing (precipitation) features the distribution of coherent GP zones with a spherical shape, which act as barriers through which dislocations can pass, provided the stress rises to the levels higher than those required to move dislocations through the matrix phase [30].

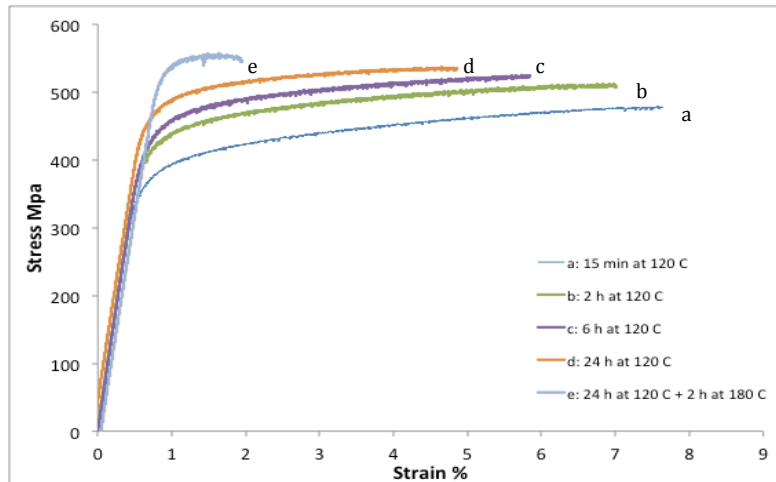
The η' phase gives the highest strengthening effect to AA7xxx alloys. The semi-coherent η' phase is reported to be tiny discs of only a few nanometer thickness with a hexagonal lattice ($a=0.496$ nm and $c=1.402$ nm) and a structure closely related to the equilibrium η phase (MgZn_2). The chemistry of the η' phase was reported to be Zn-rich with a Zn/Mg ratio of about 1.2, which is different with the composition of the η phase [30]. Typical peak ageing for the wrought Al-6Zn-2Mg-2Cu alloys occurs after 24 h. at 120 °C. It is observed that after 24 h. ageing of the shape cast Al-6Zn-2Mg-2Cu-0.25Ti alloys at 120 °C, the YS and El.% are 393 and 4.9 % respectively. Increasing the aging temperature to 180 °C raised the strength, indicating that ageing for 24 hr. at 120 °C does not correspond to the peak strengthening condition. The YS reached a peak value of 550 MPa by additional ageing at 180 °C for 2 h. Meanwhile, a minimum El.% value of 1.5% was experienced by the cast alloys at the peak age condition. It is noted that El.% was recovered after 24 h. at 180 °C where the recorded mean YS and El.% values were 393 MPa and 4.9%, respectively. When the alloy was aged to 30 h., no significant change were observed in El.% values (4.8 %), but the YS dropped to 375 MPa.

By increasing the aging temperature to 180 °C, the equilibrium η phase likely formed in the Al matrix: with an expected hexagonal lattice ($a=0.521$ nm and $c=0.860$ nm) and the chemical composition of MgZn_2 [29]. Plate-like η phase is a stable and fully incoherent precipitate that can either evolve from the η' phase or directly from decomposition of the SSSS. These particles are no longer coherent with the matrix, and their contribution to strength is lower than that of the semi-coherent η' precipitate.

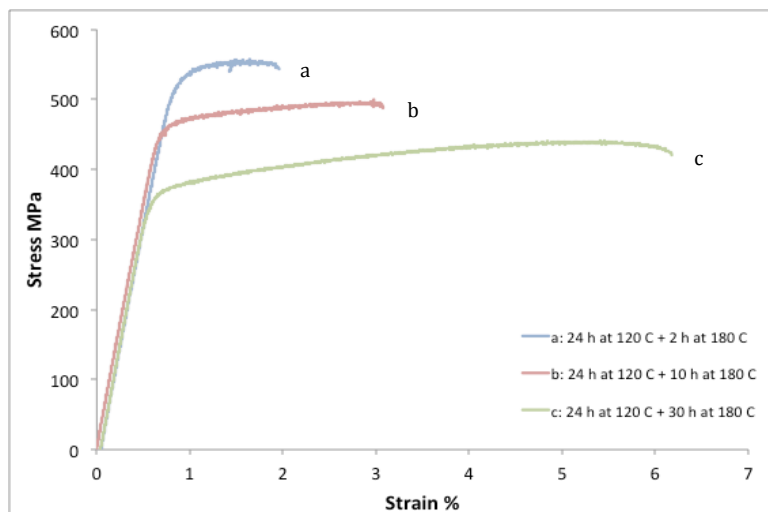
Consequently, it is quite common for a coherent GP zone precipitate to form and then

lose coherency as the particle grows to a critical size and undergoes the subsequent precipitation sequence transformations of η' and η . Continued aging beyond this stage produces particle growth and further decrease in strength. Ageing at 180 °C likely resulted in the dissolution of GP zones. Therefore, the η' phase likely became the dominant precipitate very early during ageing at 180 °C and was responsible for the peak strength. This hypothesis is consistent with the work reported by Jin [29] who studied the difference in the precipitation sequence of an Al-7.5Zn-2Mg-2Cu alloy aged at 120 °C and 160 °C. He reported that the ageing response was faster at higher temperature due to the increased precipitation driving force.

Figure 5-15 compares the stress-strain curves of under-aged, peak-aged and over-aged Al-6Zn-2Mg-2Cu alloy samples. Curves a and b in Figure 5-15-a show the tensile behavior of the samples that were under-aged for 15 min. and 2 h., respectively. Increasing the ageing time increased the stress and decreased strain at fracture. The maximum stress and minimum fracture strain was exhibited by the sample aged for 24 h. at 120 °C plus 2 h. at 180 °C. This is the peak ageing condition for the cast alloy (Al-6Zn-2Mg-2Cu). Further increase in the ageing time, reduced the stress and recovered some of the loss in fracture strain. The slope of stress-strain curve in the plastic zone is relatively low; i. e. rate of strain hardening is low. This is an implication of broad slip bands and, therefore easy glide. When the alloy is aged further, the number density of coherent GP zones likely increased, which raised the YS significantly (curve b in Figure 5-15-a). In addition, there was a simultaneous formation of the η' as the main strengthening phase and its contribution on strength increased with ageing time.



a



b

Figure 5-14 Typical tensile curves of cast Al-6Zn-2Mg-2Cu alloy during the AA treatment: (a) under-aged and peak-aged conditions and (b) peak-aged and over-aged conditions.

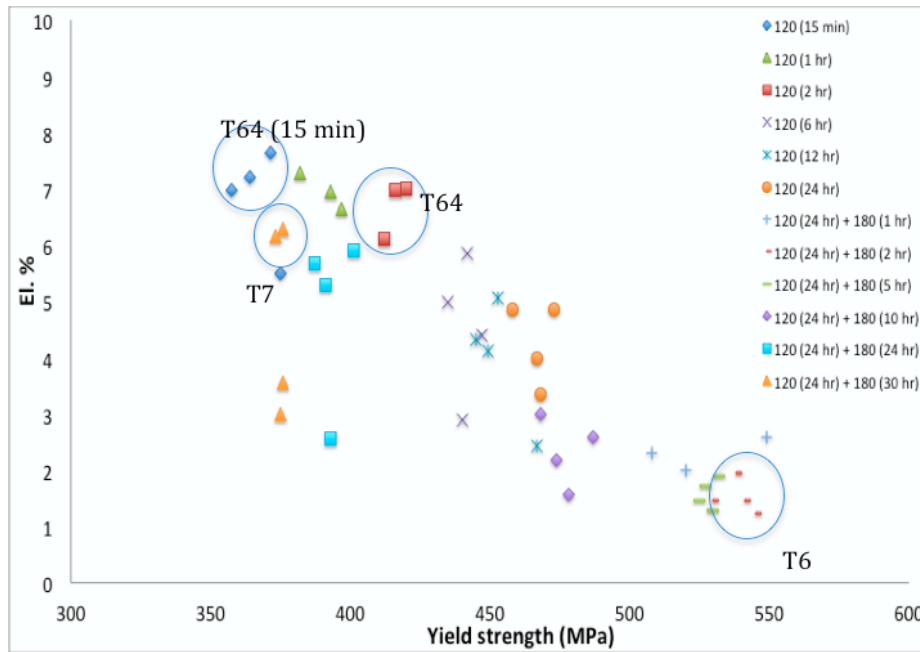
The microstructure of the peak aged samples likely contained semi-coherent η' as the dominant phase, which acts as strong impenetrable precipitate through which the

dislocations can move only by sharp changes in curvature of the dislocation line. Consequently, an accumulation of the dislocations occurs around the precipitates, which further raise the stress levels. The low elongation of the peak-aged condition (curve a in Figure 5-15-b) is attributed to the resultant higher stress during their plastic deformation combined with presence of internal casting defects, which act as stress raiser and promote the brittle fracture of the material. Curve c in in Figure 5-15-b illustrates the tensile response of the over-aged samples, in which the incoherent η phase likely is the dominant precipitate in the microstructure. These precipitates coarsen with time, which results in decrease of the YS. At this stage of AA, dislocations can no longer cut through the coarsened precipitates, but rather bypass them by leaving dislocation rings around the precipitates. The dislocation rings around the particles raise the stress and develop very high elastic strains in the precipitate. Precipitates support a significant fraction of the total applied load. The fracture of the precipitate or its debonding from the matrix determines the strength limit in defect-free over-aged alloys. However, in these cast samples, casting defects and grain boundary intermetallic precipitates play a more significant role on failure than fracture or debonding of the fine high strength matrix precipitates.

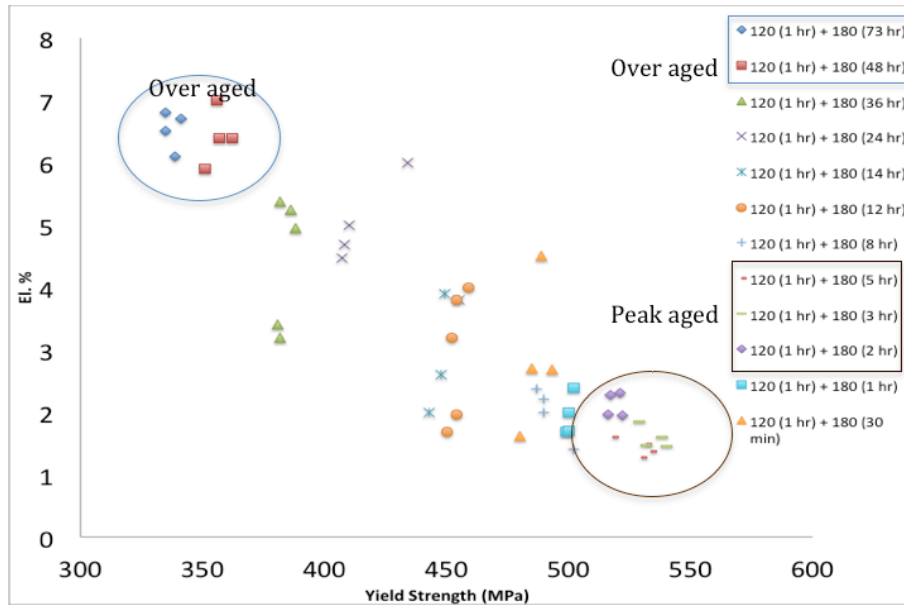
In order to better display the ageing response of the cast Al-6Zn-2Mg-2Cu alloy, the values of El.% are plotted versus the YS. Figure 5-16-a shows the tensile properties of the samples, which went through the ageing for 24 h. at 120 °C followed by 30 h. at 180 °C, while Figure 5-16-b belongs to the samples that experienced ageing for 1 h. at 120 °C followed by 73 h. at 180 °C.

The El.% versus YS plots enable the selection of heat treatment condition for desired

properties. For instance, when the desired properties lie into higher elongation values with intermediate YS, T64 (secondary aged) and T7 (over aged) heat treatment condition are more favorable, while in applications with the demand for higher YS, the heat treatment conditions close to T6 (peak age) may be selected.



a



b

Figure 5-15 El.% versus YS plots for shape cast Al-6Zn-2Mg-2Cu alloys, subjected to different ageing conditions: (a) 24 h at 120 °C plus 30 h. at 180 °C, (b) 1 h. at 120 °C plus 73 h. at 180 °C.

5.3.1 Shape casting a Camber link part using Al-6Zn-2Mg-2Cu alloys

A camber link pattern was used in order to make the sand mold and evaluate the feasibility of shape casting an automotive part using the validation Al-6Zn-2Mg-2Cu alloy. Table 5-7 presents the tensile properties of the sand mold shape cast Al-6Zn-2Mg-2Cu alloy in the NA condition. Average YS, UTS and El.% of the samples cut from part 1 were 317 MPa, 418 MPa and 7.8 %, respectively. Samples from part 2 show improved tensile properties with average YS, UTS and El.% of 336 MPa, 461 MPa, 10.7%, respectively. The YS of all the samples was higher than 300 MPa (performance criterion

set by the industrial partner). Moreover, the El.% of all samples is higher than 7% (performance criterion set by the industrial partner) with the exception of two samples in part 1 (1-3, 1-4) and a single sample in part 2 (2-1).

**Table 5-7 Tensile results of sand mold shape cast Al-6Zn-2Mg-2Cu alloys
(part 1 and 2)**

Part 1				
Specimen Name	UTS	Yield Strength	Elongation	Modulus
	MPa	MPa	%	GPa
1-1	421.42	319.06	8.40	73.16
1-2	434.20	328.24	7.89	73.78
1-3	404.53	322.70	5.94	77.78
1-4	392.57	319.03	4.16	73.83
1-5	445.77	327.21	9.28	75.06
1-6	435.21	312.19	10.00	74.06
1-7	383.98	290.54	7.98	72.08
1-8	428.53	324.04	7.93	79.22
averaged data	418.28	317.88	7.70	74.87
stdev	22.16	12.18	1.85	2.42
max	445.77	328.24	10.00	79.22
95%confidence	15.36	8.44	1.29	1.68

Part 2				
Specimen Name	UTS	Yield Strength	Elongation	Modulus
	MPa	MPa	%	GPa
2-1	441.78	344.89	5.38	81.27
2-2	471.05	347.17	9.29	79.72
2-3	478.91	350.70	11.91	81.38
2-4	483.59	352.66	10.68	81.34
2-5	462.78	339.80	10.76	77.19
2-6	437.96	304.27	15.24	73.84
2-7	448.94	327.32	10.78	78.5
2-8	464.94	340.95	10.38	77.48
2-9	458.53	317.60	12.38	76.69
averaged data	460.94	336.15	10.76	78.60
stdev	15.82	16.42	2.63	2.58
max	483.59	352.66	15.24	81.38
95%confidence	10.34	10.73	1.72	1.68

6 Conclusion

1. Grain refinement through the addition of TiBor has a strong influence on the hot tearing susceptibility of Al-Zn-Mg-Cu alloys during shape casting. No evidence of hot tearing was found in any of the 9 Taguchi alloys cast with the addition of TiBor. In contrast, evidence of hot tearing was found in all 9 of the Taguchi alloys cast without the addition of TiBor. The significant reduction in the hot tearing susceptibility is attributed to the grain refinement induced by the TiBor addition, which enables the sufficient feeding of the critical region by delaying the coherency point.

2. Depending on the chemical composition, several grain boundary intermetallic phases may form during solidification of Al– Zn–Mg–Cu alloys including η , S, T and Θ phases. Pandat simulation provides approximate information on the type and volume fraction of the grain boundary phases.

3. Taguchi experimental design method is straightforward and proved to be a powerful tool to study the effect of alloying elements on the mechanical properties of Al-Zn-Mg-Cu alloys. The Taguchi method narrowed down the number of required casting experiments, allowed for ANOVA to quantify the percentage contribution of the alloying elements on the mechanical properties of Al-Zn-Mg-Cu alloys and tested the significance of contribution from alloying elements. Cu was the alloying element that affected the variation of YS the most, followed by Zn with contribution of 59% and 28%, respectively. The effects from Mg and Ti on YS were insignificant.

4. The Taguchi method provided models to predict the YS, UTS, El.% values for Al-Zn-Mg-Cu alloys. According to the regression analyses, there were statistically meaningful

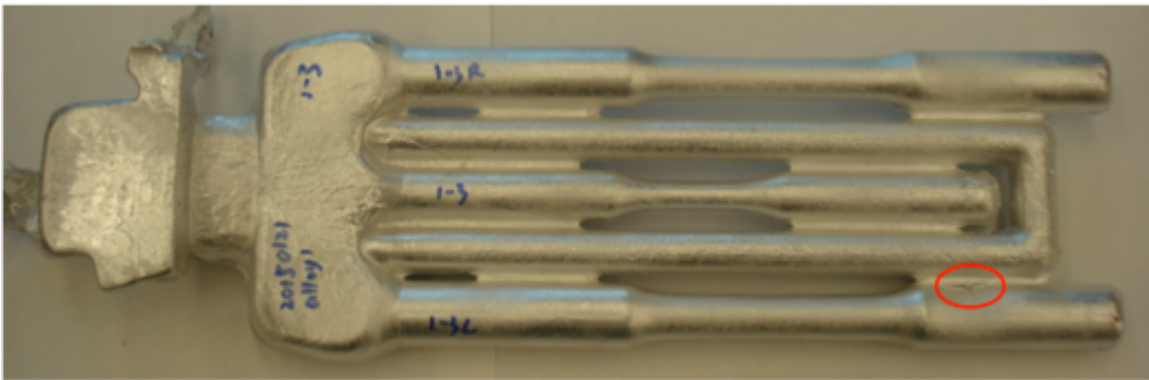
relationships between mechanical properties with Zn, Mg, Cu and Ti content. R-square values provided a measure of how well the observed experimental results are replicated by the model. The regression model for the prediction of YS revealed a more reliable prediction than regression model for UTS and El.%. The practical outcome of the proposed models could be used with acceptable accuracy at the preliminary stage of materials selection. The verification trials were performed on Al-6Zn-2Mg-2Cu alloys showed that predictions of the statistical models were in reasonable agreement with measured values.

5. The results suggest that secondary ageing is a useful type of heat treatment for achieving optimized mechanical properties for the shape cast Al-Zn-Mg-Cu alloys. A superior combination of YS and El.% was achieved for alloys 2, 5 and 7. The strength of the secondary-aged material (under-aged for 90 min. and then quenched to RT) was much higher than that in the naturally-aged material. The average YS for alloy 7 increased from 293 to 383 MPa (30% increase) and the increment of UTS was almost 9%, from 446 to 485 MPa.

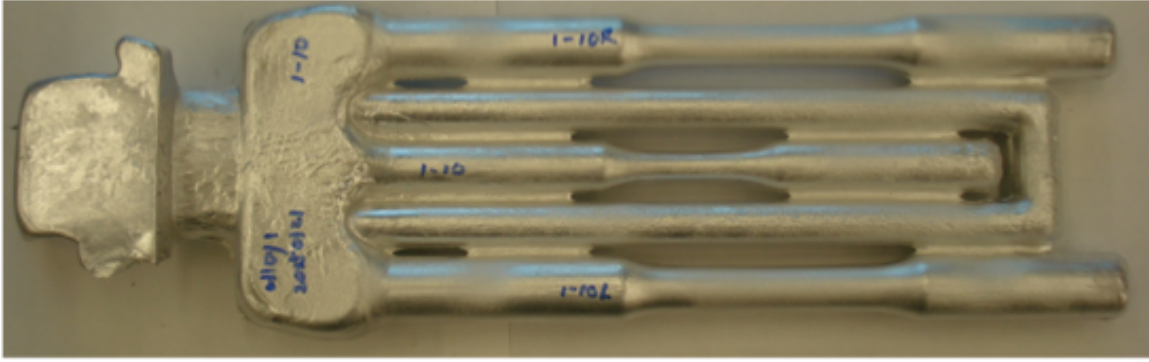
6. Based on the results of this study, it is feasible to reduce the solution treatment time at temperature of 475 °C to 3.5 h, retain the tensile properties and more importantly increases the energy efficiency of the heat treatment process to a significant extent.

7 Appendix A Visual inspection of castings

Castings of all 9 Taguchi designed alloys were examined before and after grain refinement (Figure 7-1 to 7-9).

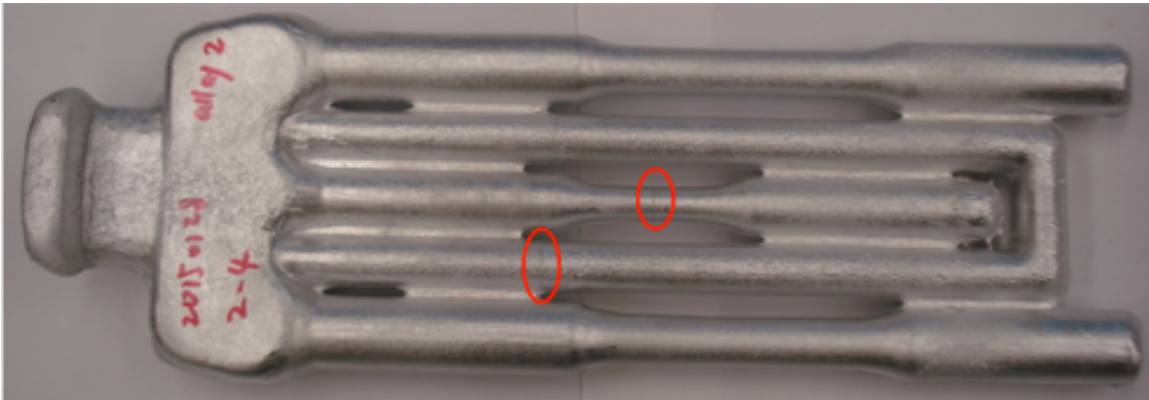


a

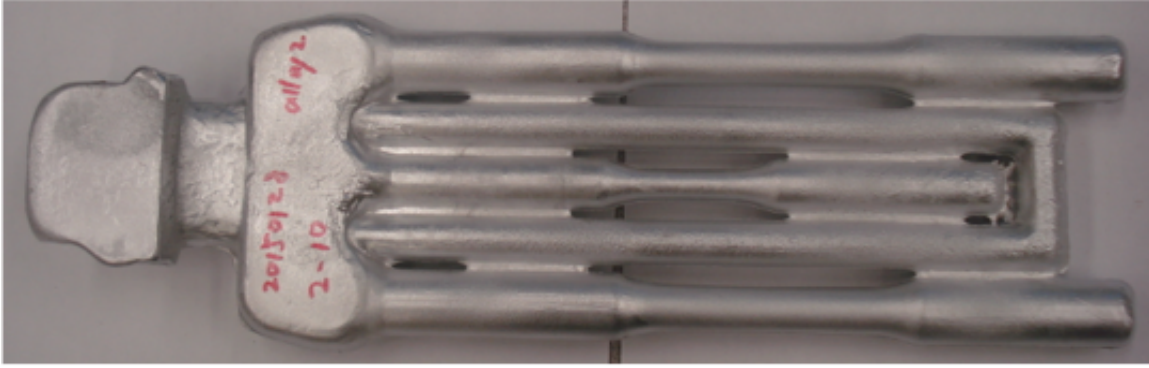


b

Figure 7-1 Image showing the appearance of the alloy castings (a) without the TiBor addition (Alloy 1) and (b) with the TiBor addition (Alloy 1). Red frames document the locations of visible cracks.

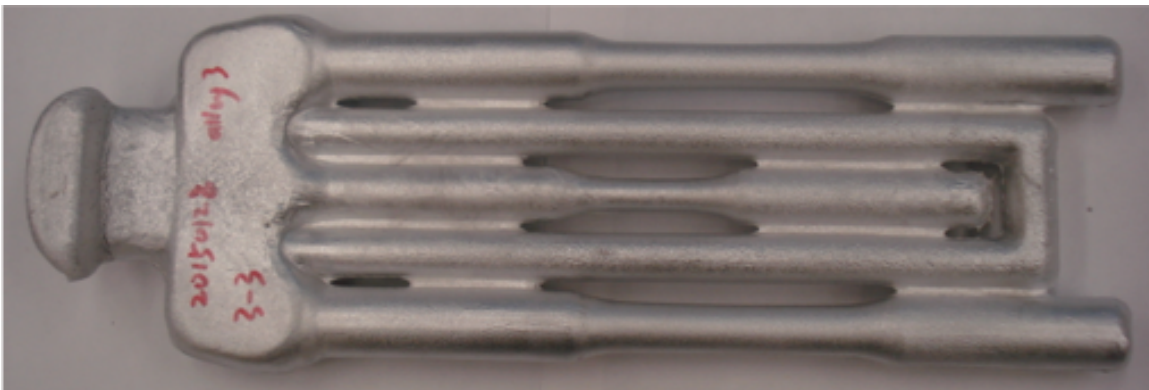


a



b

7- 2 Image showing the appearance of the alloy castings (a) without the TiBor addition (Alloy 2) and (b) with the TiBor addition (Alloy 2). Red frames document the locations of visible cracks.

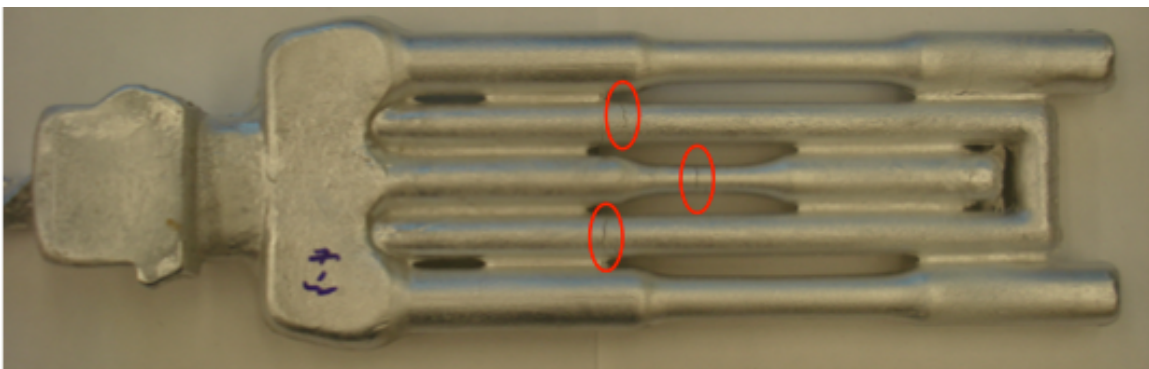


a

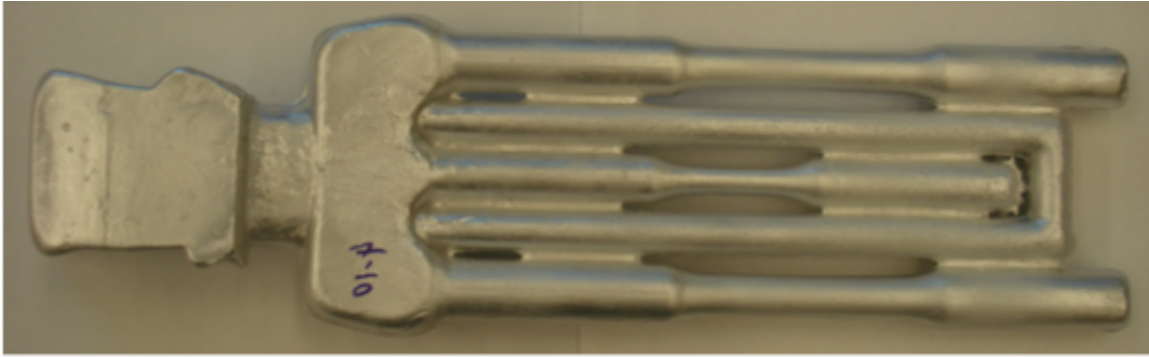


b

Figure 7-3 Image showing the appearance of the alloy castings (a) without the TiBor addition (Alloy 3) and (b) with the TiBor addition (Alloy 3). Red frames document the locations of visible cracks.

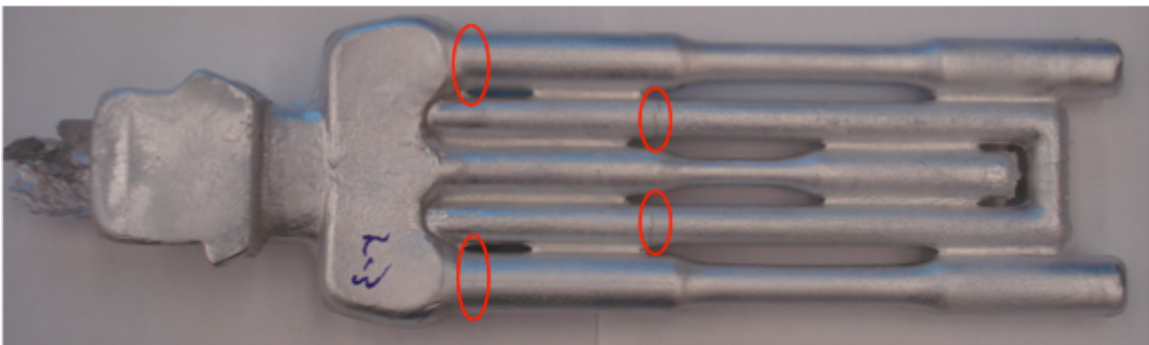


a

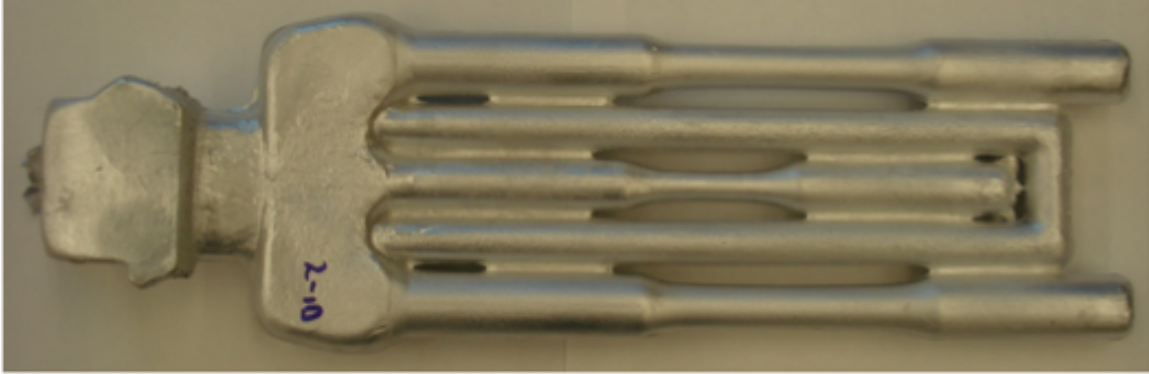


b

Figure 7-4 Image showing the appearance of the alloy castings (a) without the TiBor addition (Alloy 4) and (b) with the TiBor addition (Alloy 4). Red frames document the locations of visible cracks.

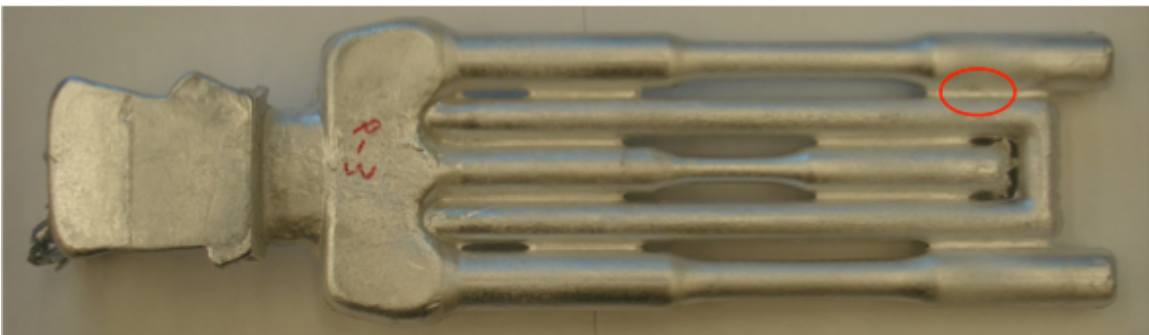


a



b

Figure 7-5 Image showing the appearance of the alloy castings (a) without the TiBor addition (Alloy 5) and (b) with the TiBor addition (Alloy 5). Red frames document the locations of visible cracks.

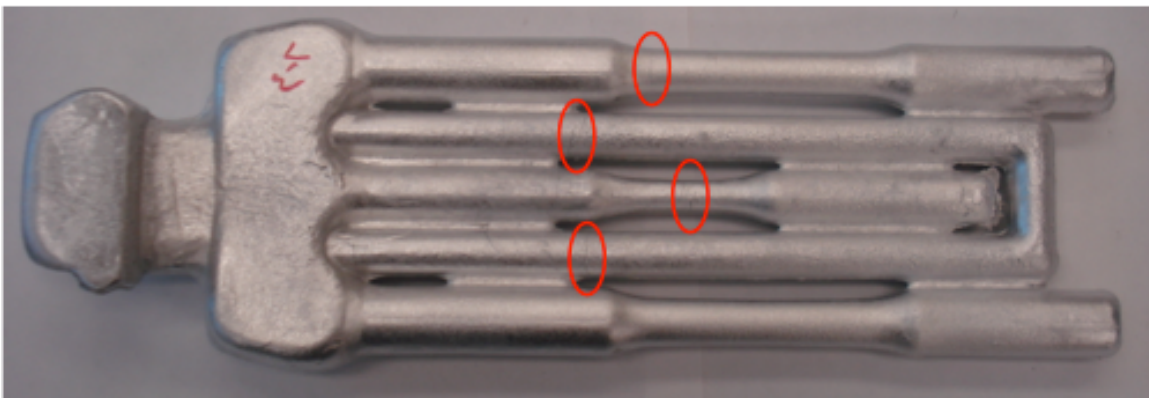


a



b

Figure 7-6 Image showing the appearance of the alloy castings (a) without the TiBor addition (Alloy 6) and (b) with the TiBor addition (Alloy 6). Red frames document the locations of visible cracks.



a



b

Figure 7-7 Image showing the appearance of the alloy castings (a) without the TiBor addition (Alloy 7) and (b) with the TiBor addition (Alloy 7). Red frames document the locations of visible cracks.

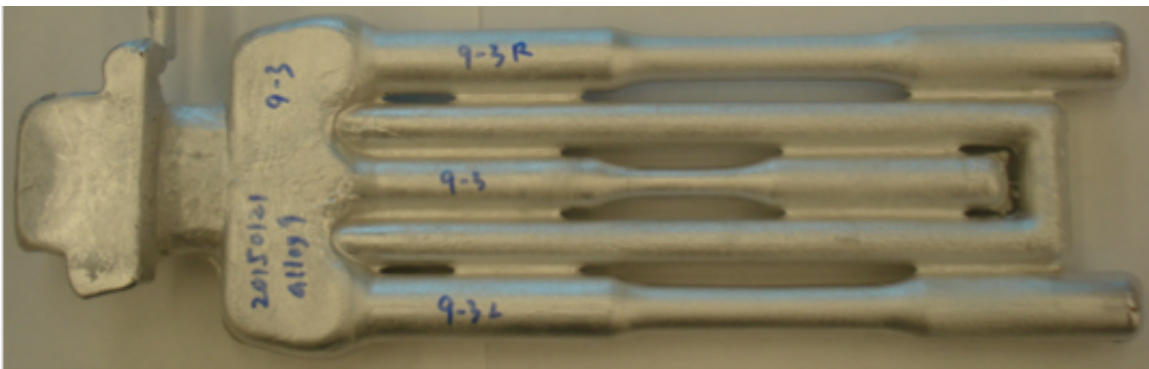


a



b

Figure 7-8 Image showing the appearance of the alloy castings (a) without the TiBor addition (Alloy 8) and (b) with the TiBor addition (Alloy 8). Red frames document the locations of visible cracks.



a

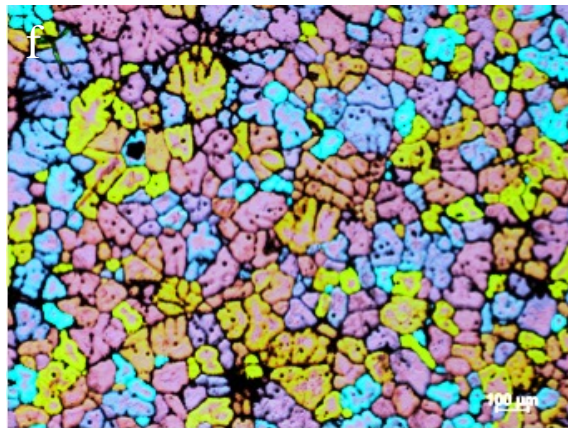
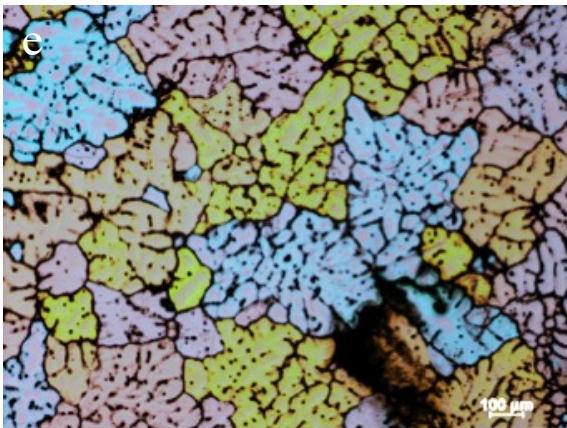
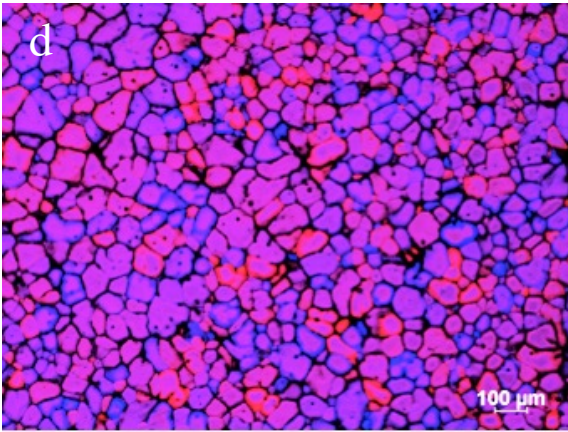
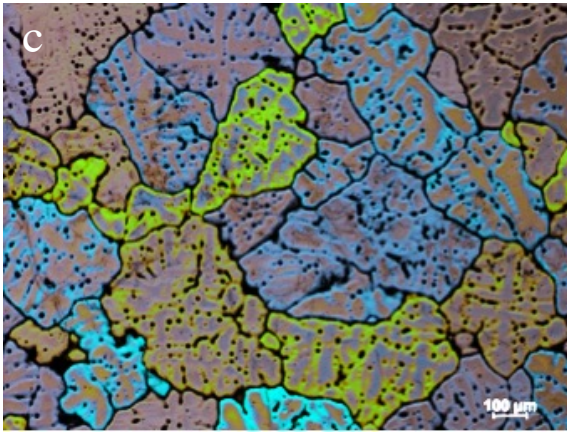
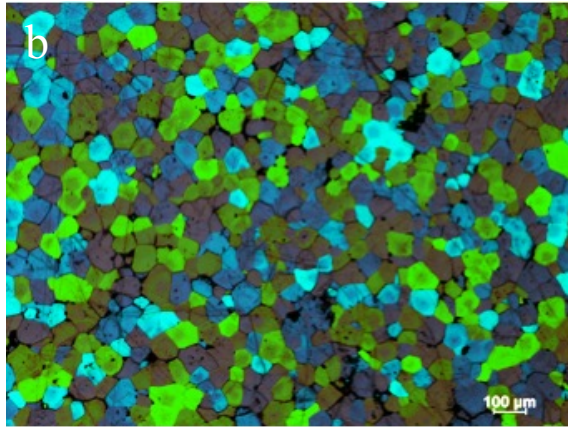
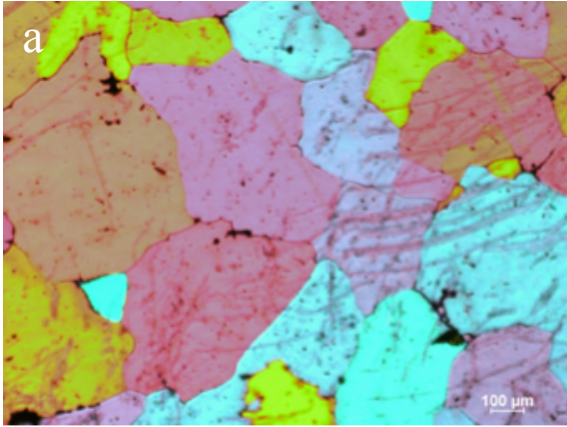


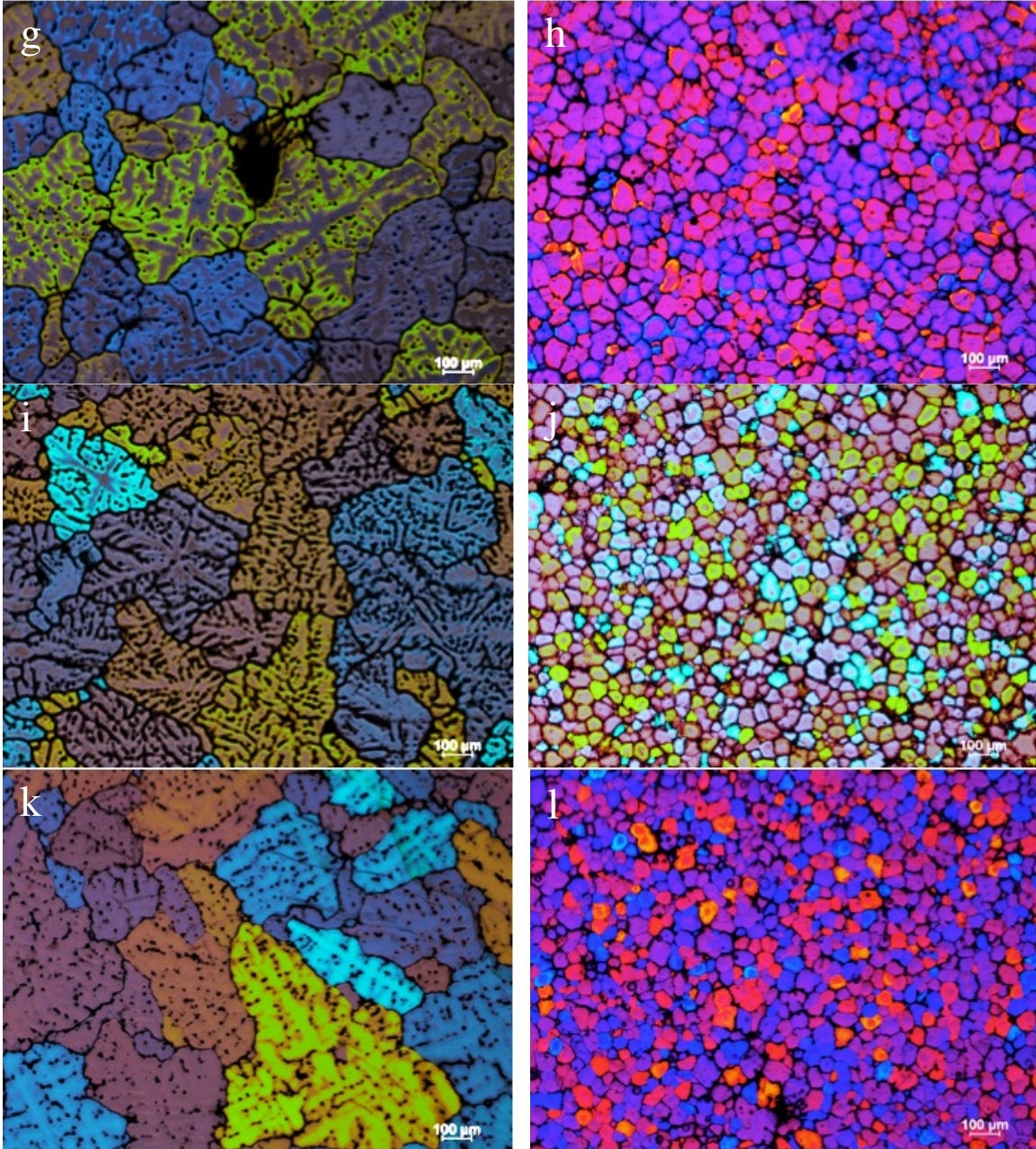
b

Figure 7-9 Image showing the appearance of the alloy castings (a) without the TiBor addition (Alloy 9) and (b) with the TiBor addition (Alloy 9). Red frames document the locations of visible cracks.

8 Appendix B Grain structure

The microstructure of 9 Taguchi designed alloys were studied for their grain structure before and after grain refinement (Figure 8-1).





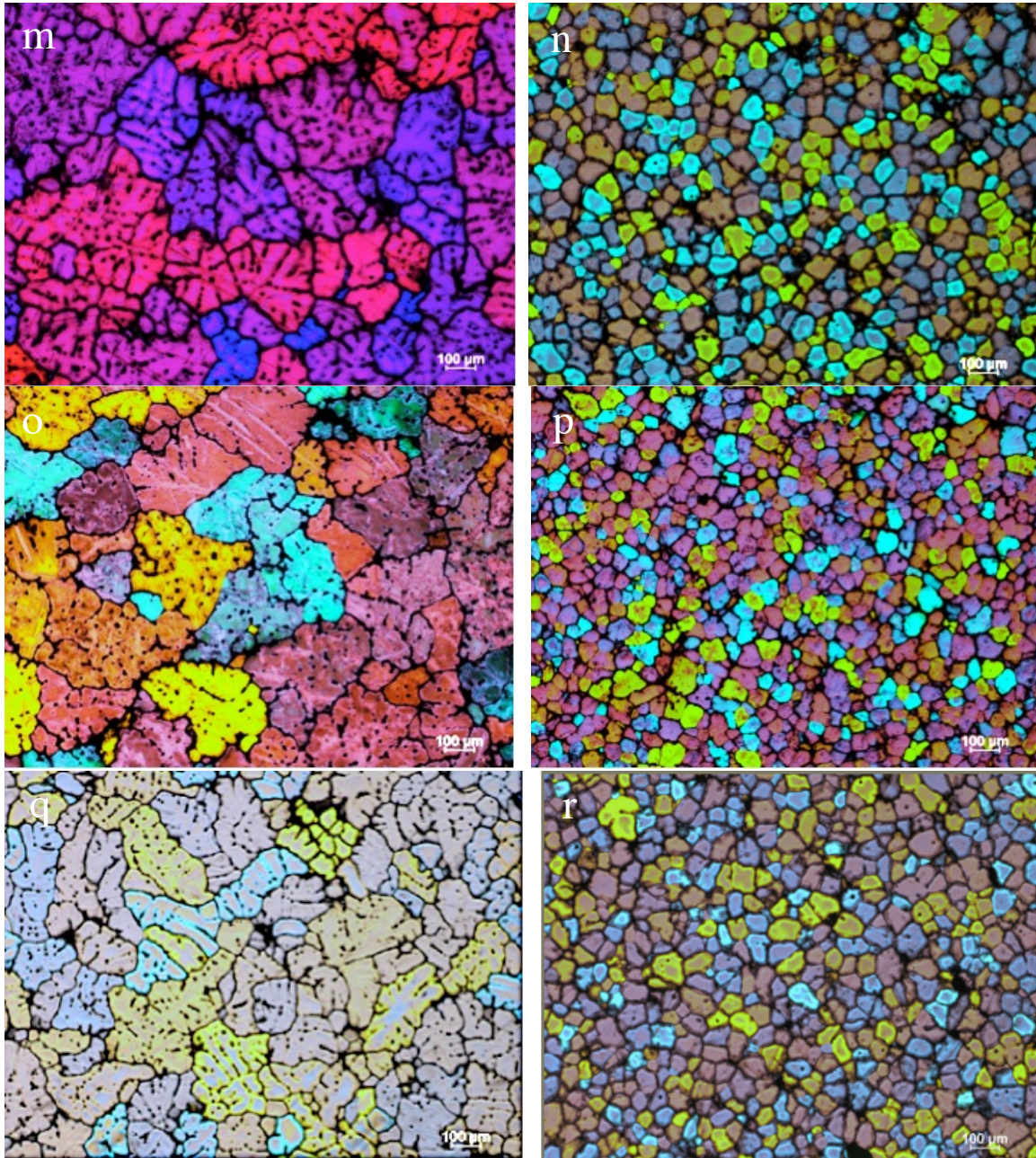


Figure 8-1 Typical grain structure of as-cast Al-Zn-Mg-Cu alloys before (images on the left) and after (images on the right) grain refinement: (a) and (b) alloy 1, (c) and (d) alloy 2, (e) and (f) alloy 3, (g) and (h) alloy 4, (i) and (j) alloy 5, (k) and (l) alloy 6, (m) and (n) alloy 7, (o) and (p) alloy 8, (q) and (r) alloy 9.

9 Appendix C Thermal analysis

Thermal analysis was used to measure the temperature of the sample during the heating in order to characterize the solidification and melting characteristics in terms of any phase transformations associated with endothermic and exothermic reactions. A Data Acquisition (DAQ) system controlled by LabVIEW software was used to record the temperature-time profiles. Once this data was collected, Easyplot software was used to obtain the first derivative curves to facilitate interpretation. Figure 9-1 displays a typical heating curve of the Al-3.5Zn-2Mg-1.2Cu alloy. The melting temperature (T_m) of each alloy was determined using the heating (T-t) curve.

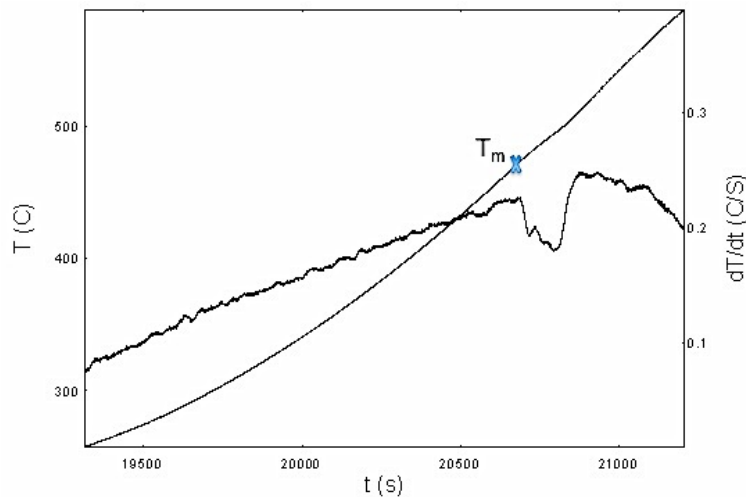
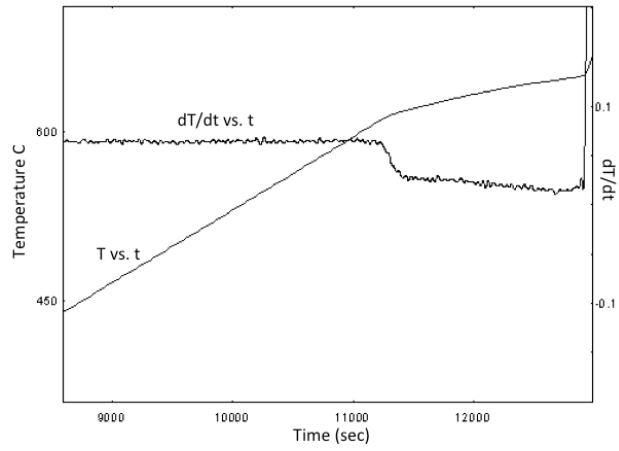


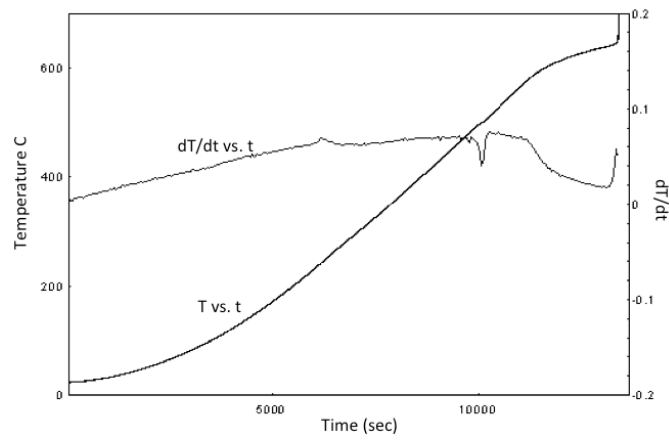
Figure 9-1 Typical heating (T-t) and first derivative (dT/dt) curves for the Al-3.5Zn-2Mg-1.2Cu alloy. T_m denotes the melting temperature of the sample.

Figure 9-2 presents the heating curves of the Taguchi designed alloys, which were used to

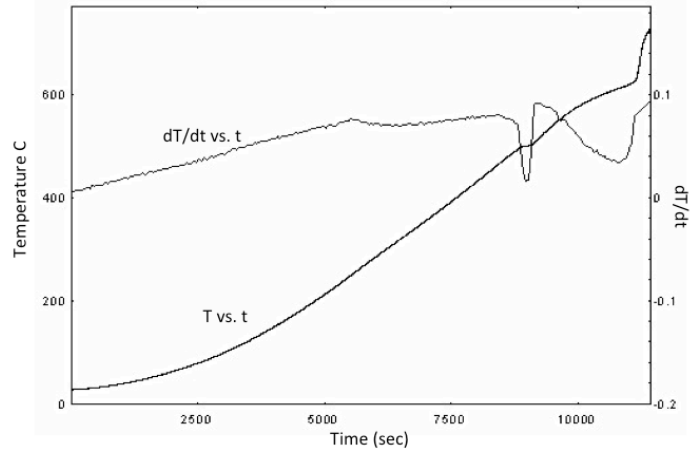
find their melting temperature.



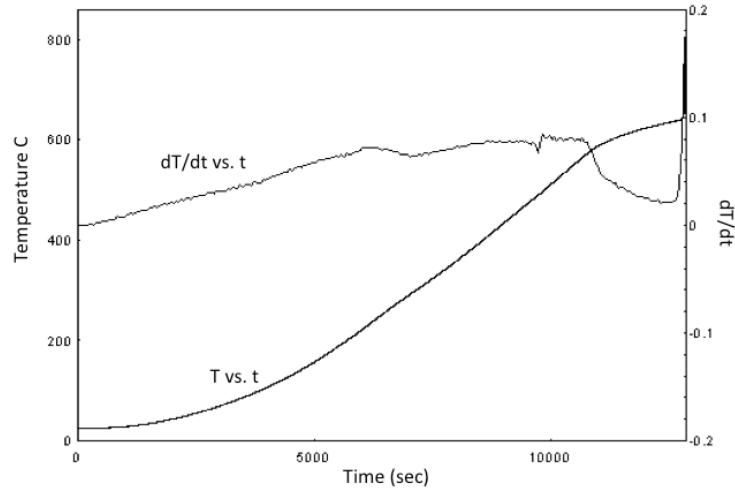
a



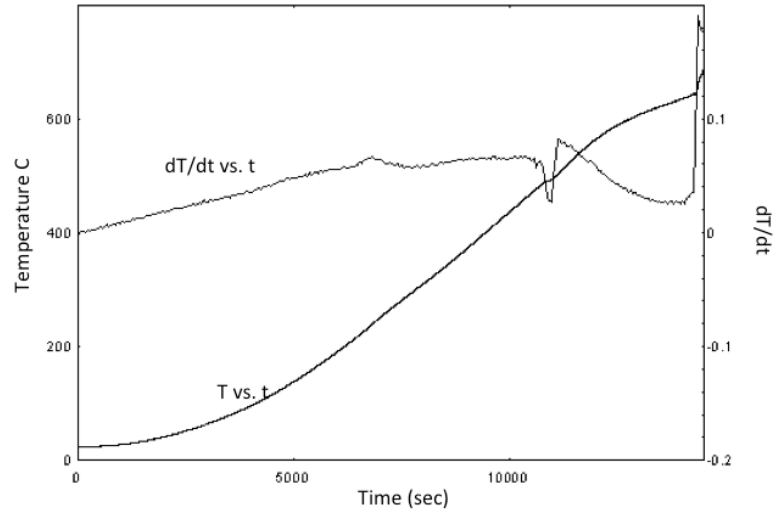
b



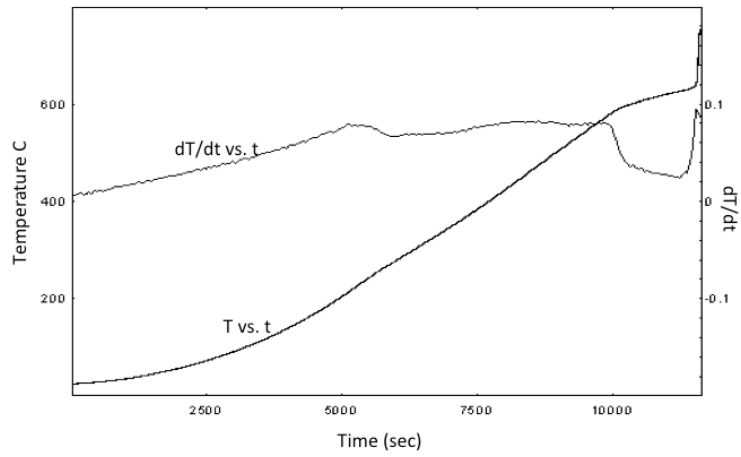
c



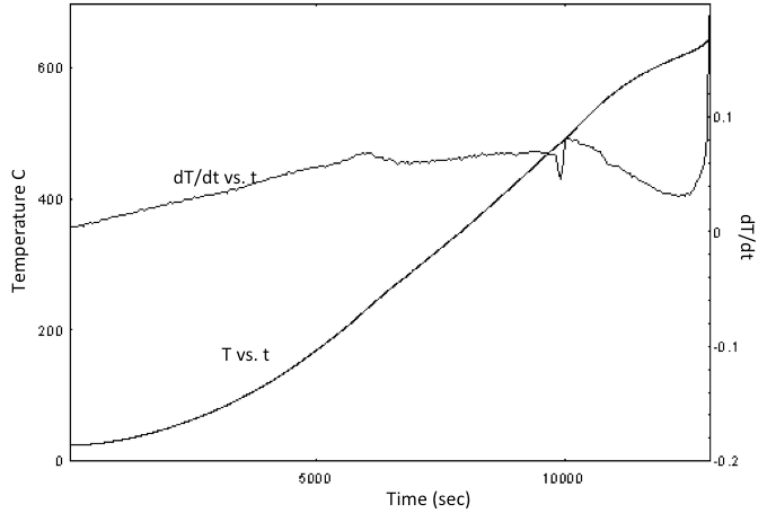
d



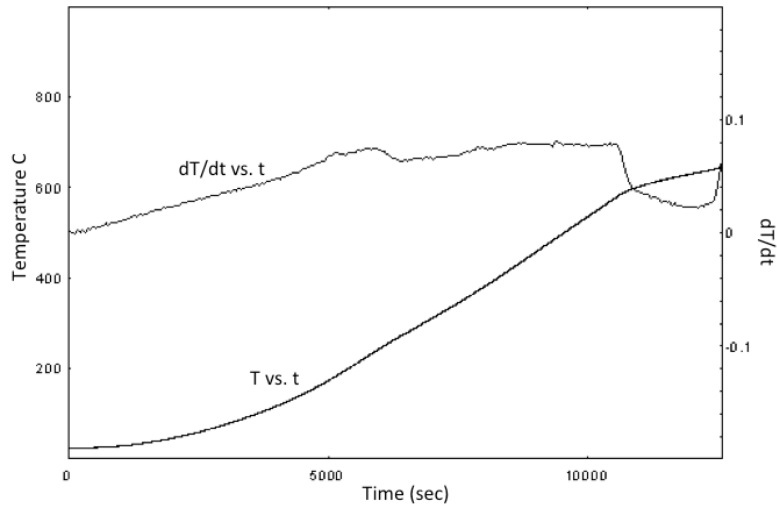
e



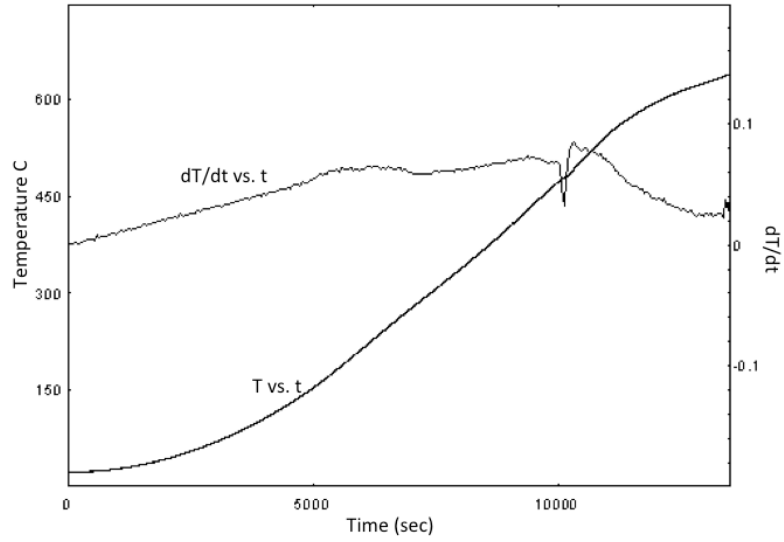
f



g



h

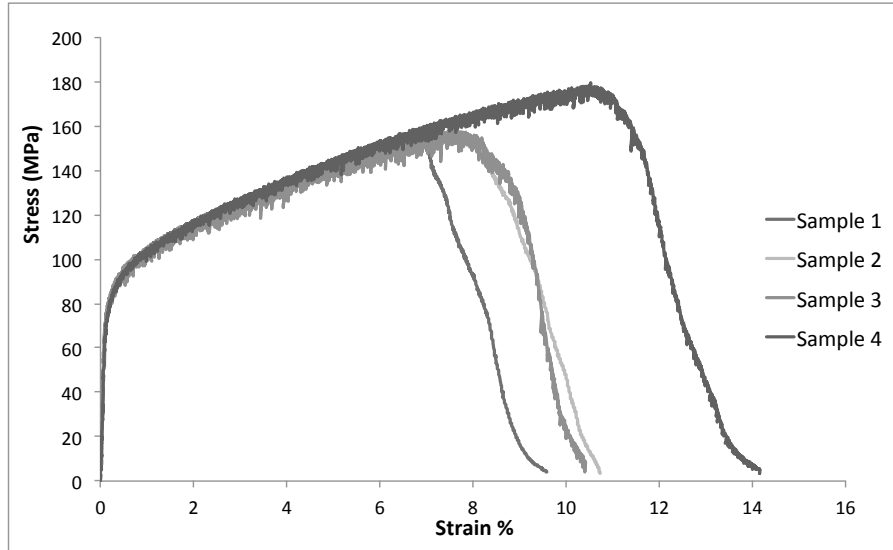


i

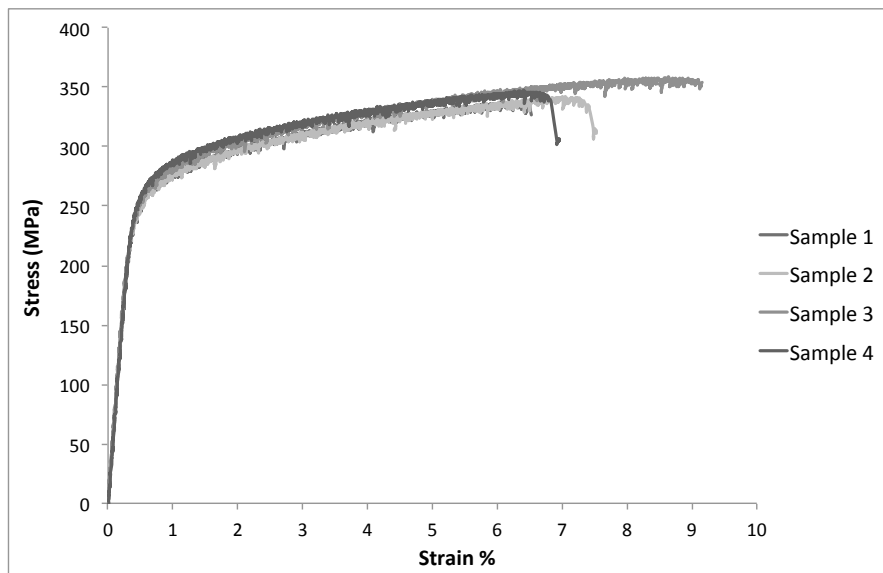
Figure 9-2 Thermal analysis of the 9 Taguchi designed alloys (Heating curves and their first derivative): (a) Alloy 1, (b) Alloy 2, (c) Alloy 3, (d) Alloy 4, (e) Alloy 5, (f) Alloy 6, (g) Alloy 7, (h) Alloy 8, (i) Alloy 9.

10 Appendix C Tensile properties of 9 alloys

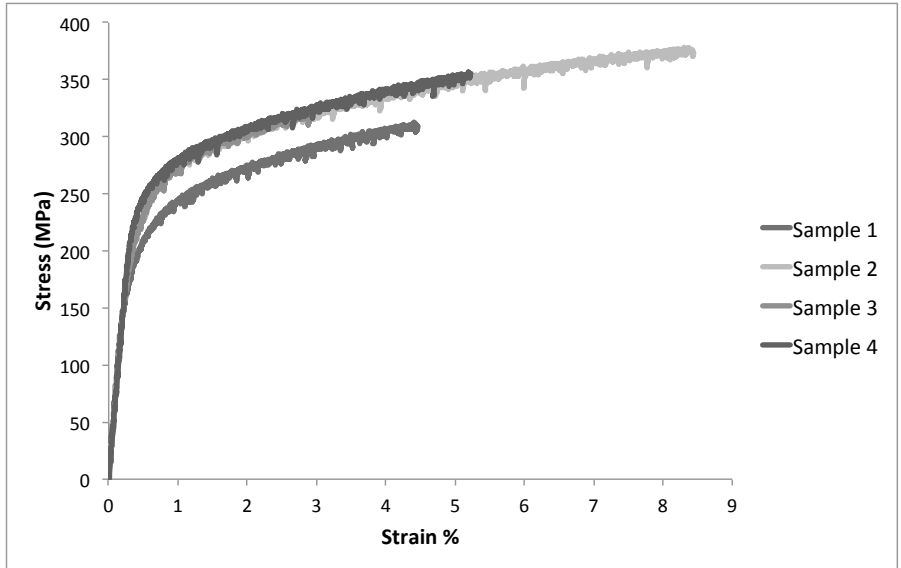
Figure 10-1 presents the tensile curves of the 9 Taguchi designed alloys.



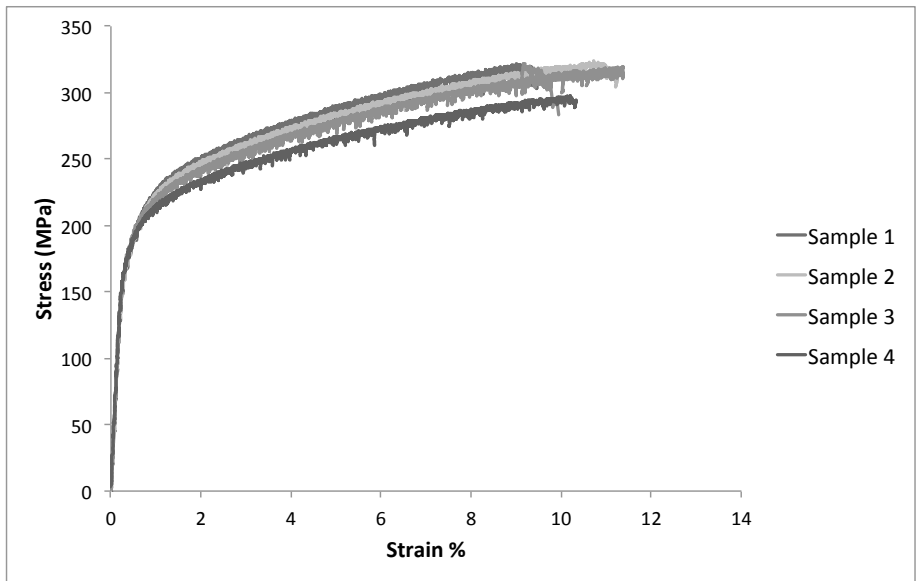
a



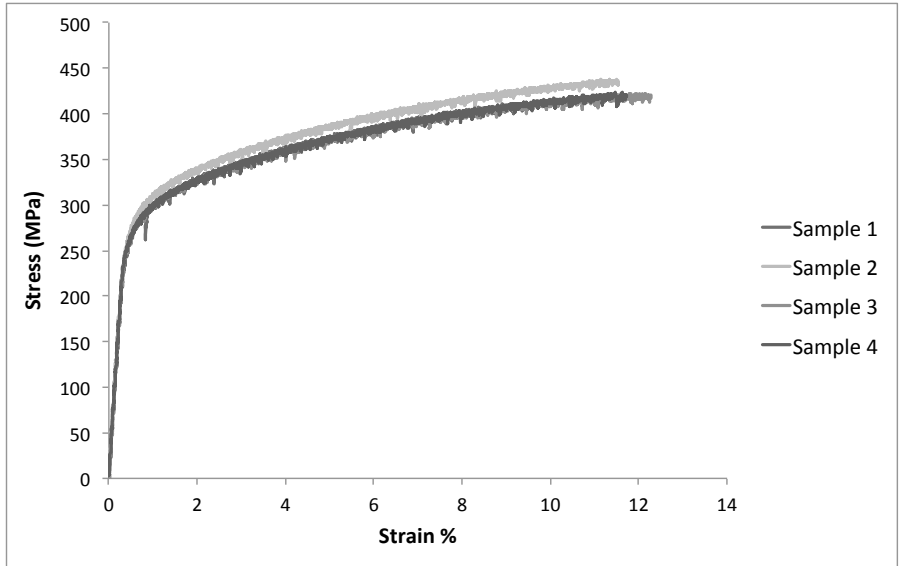
b



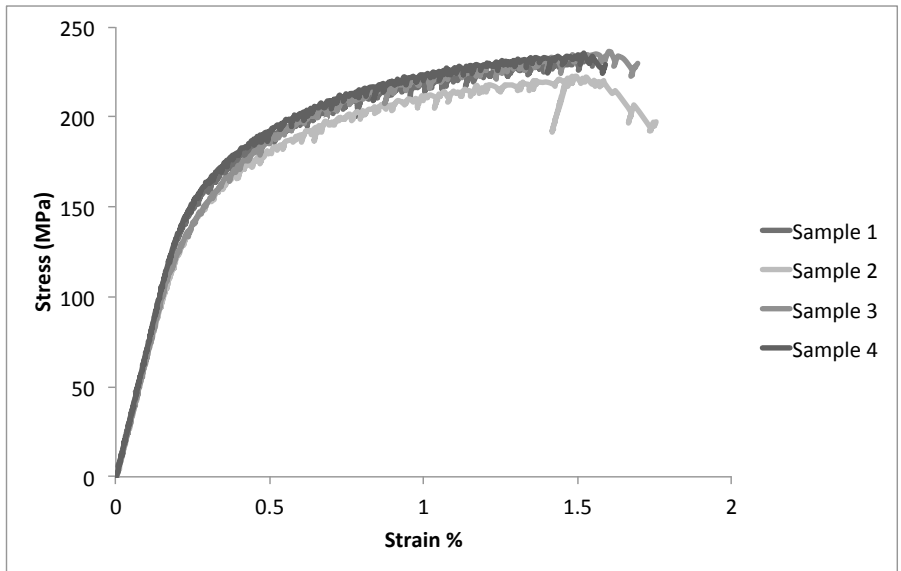
c



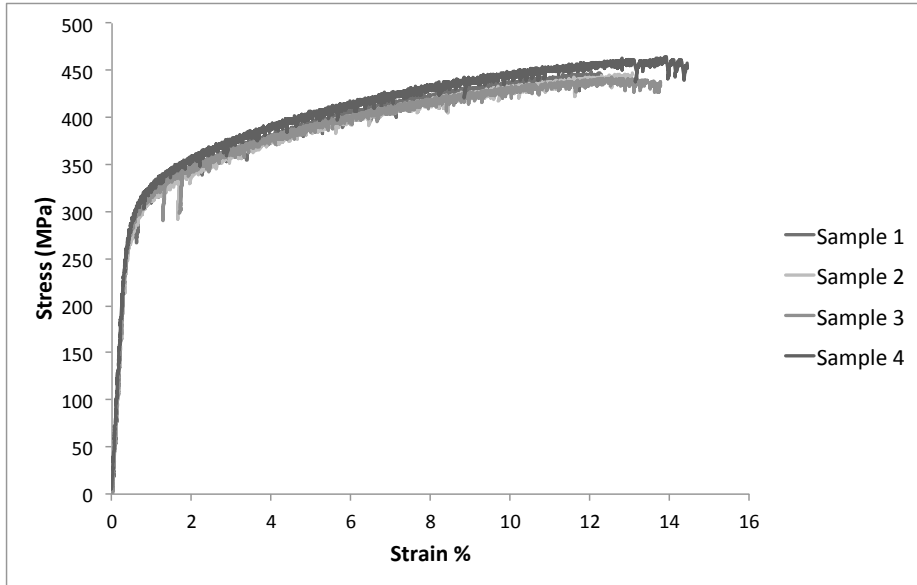
d



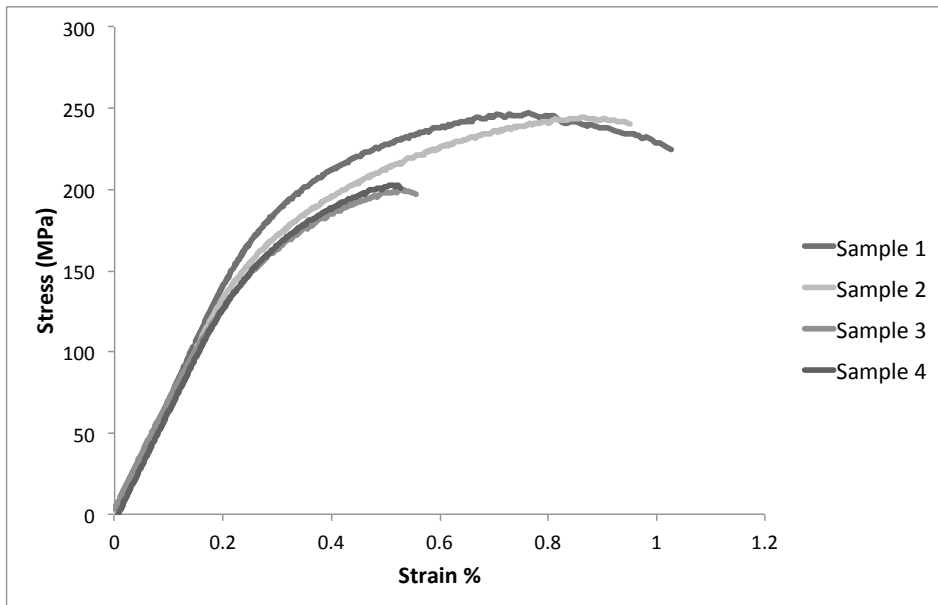
e



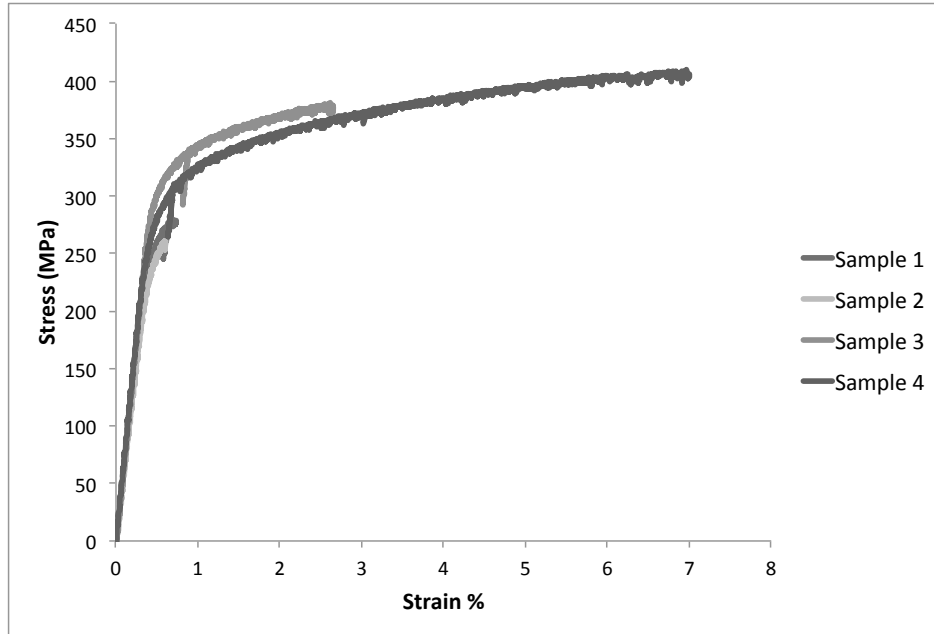
f



g



h



i

Figure 10-1 Tensile curves of the 9 Taguchi designed alloys: (a) Alloy 1, (b) Alloy 2, (c) Alloy 3, (d) Alloy 4, (e) Alloy 5, (f) Alloy 6, (g) Alloy 7, (h) Alloy 8, (i) Alloy 9.

The tensile properties including the YS, UTS, and El.% were measured. Table 10-1 gives the data of tensile properties and casting .

Table 10-1 List of tensile properties data for the Taguchi designed 9 alloys

	YS 1	YS 2	YS 3	YS 4	YS 5	YS 6	YS 7	YS 8	YS 9	YS 10	YS 11	YS 12
Alloy 1	90	88	88	88	81	85	114	113	64	85	116	89
Alloy 2	171	166	174	180	171	176	176	171	174	176	179	174
Alloy 3	253	207	238	240	210	194	194	203	252	249	250	207
Alloy 4	193	198	191	188	186	201	183	186	190	180	203	205
Alloy 5	284	271	280	248	267	270	266	266	267	277	272	272
Alloy 6	186	191	171	192	181	180	186	179	186	190	175	181
Alloy 7	301	300	297	297	292	295	295	289	295	290	295	287
Alloy 8	214	191	230	215	196	201	208	187	212	213	234	228
Alloy 9	319	321	276	309	249	288	277	272	260	317	322	296
	UTS 1	UTS 2	UTS 3	UTS 4	UTS 5	UTS 6	UTS 7	UTS 8	UTS 9	UTS 10	UTS 11	UTS 12
Alloy 1	159	157.5	173	192	175	178	193.5	182	185	203	198	153
Alloy 2	285	299	309	325	279	320	322	306	298	300	321	304
Alloy 3	356	309	315	313	305.7	234	243	312	387	372	378	315.37
Alloy 4	349	345	321	321	323	341	340	297	277	263	344	346
Alloy 5	438	411	442	411	391	417	397	407.4	407	429	422	427
Alloy 6	224	248	187	246	204	183	233	222	236	235	231	214
Alloy 7	464	462	455	442	444	449	460.5	443	454	447	456	389
Alloy 8	238	197	247	244	199	203	215.5	189	216	241	244	249
Alloy 9	411.6	416.9	307	401	255	318	282	279	261	398	381	409
	El.% 1	El.% 2	El.% 3	El.% 4	El.% 5	El.% 6	El.% 7	El.% 8	El.% 9	El.% 10	El.% 11	El.% 12
Alloy 1	10.4	10.7	14.9	18.6	16.8	14.9	11.39	8.97	10.25	11.24	11	9.5
Alloy 2	11	13	13.9	13.3	11	13.3	11.9	13.8	12.69	11.48	15.9	11.53
Alloy 3	5.22	3.5	2.89	2.5	3.7	0.9	0.95	4.5	9.6	8	8.4	4.4
Alloy 4	11.9	11.6	11.5	9.9	11.4	14.1	13	10.8	4	3.4	10	10.57
Alloy 5	11.5	9.4	14	11.1	7.8	10.4	9.2	10.2	10.2	11.5	10.6	11
Alloy 6	1.4	1.5	0.7	4.4	0.8	0.6	2.3	2.2	1.6	3.8	3.3	2.8
Alloy 7	14.4	13.2	15.5	13.78	13.4	12.29	15.37	14.54	13.9	13	15.3	6.8
Alloy 8	1.68	0.61	1.02	0.95	0.55	0.52	0.87	0.52	0.67	0.98	0.75	0.89
Alloy 9	5.09	5.41	1.5	4.4	0.65	1.07	0.69	0.7	0.6	4.48	2.6	7.1
	Q 1	Q 2	Q 3	Q 4	Q 5	Q 6	Q 7	Q 8	Q 9	Q 10	Q 11	Q 12
Alloy 1	311.6	311.9	349	382.4	358.8	354	352	324.9	336.6	360.6	354.2	299.66
Alloy 2	441.2	466.1	480.5	493.6	435.2	488.6	483.3	477	463.5	459	501.2	463.27
Alloy 3	463.7	390.6	384.1	372.7	390.9	227.1	239.7	410	534.3	507.5	516.6	411.89
Alloy 4	510.3	504.7	480.1	470.3	481.5	513.4	507.1	452	367.3	342.7	494	499.61
Alloy 5	597.1	557	613.9	567.8	524.8	569.6	541.6	558.7	558.3	588.1	575.8	583.21
Alloy 6	245.9	274.4	163.8	342.5	189.5	149.7	287.3	273.4	266.6	322	308.8	281.07
Alloy 7	637.8	630.1	633.5	612.9	613.1	612.4	638.5	617.4	625.5	614.1	633.7	513.88
Alloy 8	271.8	164.8	248.3	240.7	160.1	160.4	206.4	146.4	189.9	239.7	225.3	241.41
Alloy 9	411.6	416.9	307	401	255	318	282	279	261	398	381	409

Multiple linear regression analysis was used to derive equations, which relates chemical composition and properties. Using multiple linear regression analysis, the discrete experimental data is fit to a curve and a model is derived which represents the general trend of the data. Multiple regression models to predict mean El.%, UTS, YS and Q are given below:

$$\text{Mean El.\%} = 26.6 - 1.01 (\text{Zn \%}) - 7.48 (\text{Mg \%}) + 2.4 (\text{Cu \%}) - 11.9 (\text{Ti \%})$$

$$\text{Mean UTS} = 134 + 22.6 (\text{Zn \%}) - 4.7 (\text{Mg \%}) + 82 (\text{Cu \%}) - 136 (\text{Ti \%})$$

$$\text{Mean YS} = -86.9 + 32.2 (\text{Zn \%}) + 47.5 (\text{Mg \%}) + 45.5 (\text{Cu \%}) - 31.7 (\text{Ti \%})$$

$$\text{Mean Q} = 504.8 + 0.8 (\text{Zn \%}) - 82.7 (\text{Mg \%}) + 116.1 (\text{Cu \%}) - 366.9 (\text{Ti \%})$$

Minitab was used to measure the S/N ratios for the tensile properties and casting quality. Similar equations are obtained for prediction of S/N ratios. Table 10-2 shows the experimental and predicted values of the mean YS, UTS, El.% and Q. Moreover, the experimental and predicted values of the S/N ratio are also included in table 10-2.

Standard deviation is taken into account in order to place more emphasis on the observation with small variance and model the weighted mean values of YS, UTS, El.% and Q.

$$\text{Weighted Mean El.\%} = 26.3 - 0.89 (\text{Zn \%}) - 7.5 (\text{Mg \%}) + 2.09 (\text{Cu \%}) - 9.6 (\text{Ti \%})$$

$$\text{Weighted Mean UTS} = 137 + 24.2 (\text{Zn \%}) - 10.23 (\text{Mg \%}) + 83.86 (\text{Cu \%}) - 153 (\text{Ti \%})$$

$$\text{Weighted Mean YS} = -89.43 + 33.05 (\text{Zn \%}) + 47.5 (\text{Mg \%}) + 45.5 (\text{Cu \%}) - 35.2 (\text{Ti \%})$$

$$\text{Weighted Mean } Q = 518.5 + 3.8 (\text{Zn } \%) - 95.1 (\text{Mg } \%) + 118.5 (\text{Cu } \%) - 419 (\text{Ti } \%)$$

Statistical models were used to predict the mean and weighted mean values of YS, UTS, El.% and Q. Considering the YS values, alloy 7 (299 MPa), alloy 9 (297 MPa), alloy 5 (274 MPa) and alloy 3 (247 MPa) show the highest strength. The El.% values of alloy 7 (14%) and alloy 5 (11%) are promising. However, alloy 9 and alloy 3 show poor performance during plastic deformation and fail at low strain values of 3% and 6%, respectively.

Among the alloys with 1.2% Cu, alloy 2 and alloy 4 show high El.% values of 12% and 11%, respectively. However, their YS values are relatively low. The Cu free alloys show the inferior casting quality, specifically poor was observed by alloys 6 and alloy 8 with Q values of 289 MPa and 208 MPa. It is noted that casting an alloy with chemical composition of 6.5Zn-1.5Mg-2.4Cu-0.15Ti (Alloy 7) has resulted in the superior YS (299 MPa), UTS (456 MPa), El.% (14%) and Q (629 MPa) among the rest of Taguchi designed alloys. Second alloy in terms of casting quality is Cu containing alloy 5 with Q value of 575 MPa, followed by alloy 4 with Q value 465 MPa.

Table 10-2 Experimental and predicted means and S/N ratios of YS, UTS, El.% and Q.

	Mean YS	Predicted YS	Residual	S/N ratio	Predicted S/N ratio	Residual
Alloy 1	96.0	95.42	0.55	38.92	39.74	-0.82
Alloy 2	176.0	170.94	5.06	44.81	43.73	1.08
Alloy 3	247.0	246.45	0.55	46.90	47.72	-0.82
Alloy 4	189.0	192.77	-3.77	45.64	45.26	0.39
Alloy 5	274.0	276.86	-2.86	48.61	48.14	0.47
Alloy 6	182.8	188.52	-5.69	45.24	44.98	0.27
Alloy 7	299.2	298.70	0.47	49.38	49.67	-0.30
Alloy 8	213.7	210.36	3.30	46.41	46.51	-0.09
Alloy 9	296.8	294.45	2.39	49.22	49.39	-0.17
	Mean UTS	Predicted UTS	Residual	S/N ratio	Predicted S/N ratio	Residual
Alloy 1	185.6	198.87	-13.28	45	45.7	-0.7222
Alloy 2	301.1	282.82	18.31	50	48.7	1.27778
Alloy 3	353.5	366.78	-13.28	51	51.7	-0.7222
Alloy 4	316.5	306.85	9.65	50	49.4	0.61111
Alloy 5	421.8	427.63	-5.83	52	52.4	-0.3889
Alloy 6	228.5	215.80	12.70	47	46.9	0.11111
Alloy 7	456.1	451.66	4.44	53	53.1	-0.0556
Alloy 8	225.75	239.84	-14.09	47	47.6	-0.5556
Alloy 9	362	360.61	1.39	51	50.6	0.44444
	Mean El.%	Predicted El.%	Residual	S/N ratio	Predicted S/N ratio	Residual
Alloy 1	9.8	11.2	-1.34	21.2	24.5	-3.3
Alloy 2	11.8	9.3	2.46	22.0	16.9	5.0
Alloy 3	6.1	7.4	-1.34	6.1	9.4	-3.3
Alloy 4	10.5	10.4	0.09	17.2	17.1	0.1
Alloy 5	10.6	11.8	-1.23	20.2	20.3	0.0
Alloy 6	2.7	1.1	1.58	1.5	-1.5	3.0
Alloy 7	14.3	13.0	1.36	21.9	20.4	1.4
Alloy 8	0.8	2.2	-1.45	-2.9	-1.3	-1.6
Alloy 9	3.5	3.6	-0.13	0.4	1.8	-1.4
	Mean Q	Predicted Q	Residual	S/N ratio	Predicted S/N ratio	Residual
Alloy 1	333.1	361.6	-28.5	50.6	51.7	-1.09
Alloy 2	460.4	426.6	33.8	53.4	52.0	1.46
Alloy 3	463.2	491.7	-28.5	51.2	52.3	-1.09
Alloy 4	465.3	436.2	29.0	53.2	52.2	0.95
Alloy 5	575.1	600.3	-25.2	55.1	55.4	-0.31
Alloy 6	289.8	247.1	42.7	47.4	46.6	0.78
Alloy 7	629.4	609.9	19.5	55.7	55.7	0.07
Alloy 8	208.2	256.7	-48.5	45.8	46.8	-1.02
Alloy 9	426.6	420.8	5.8	50.3	50.0	0.25

11 Appendix D Tensile properties of validation alloys

Figure 11-1 presents the tensile curves of Al-6Zn-2Mg-2Cu alloys in different heat treatment conditions.

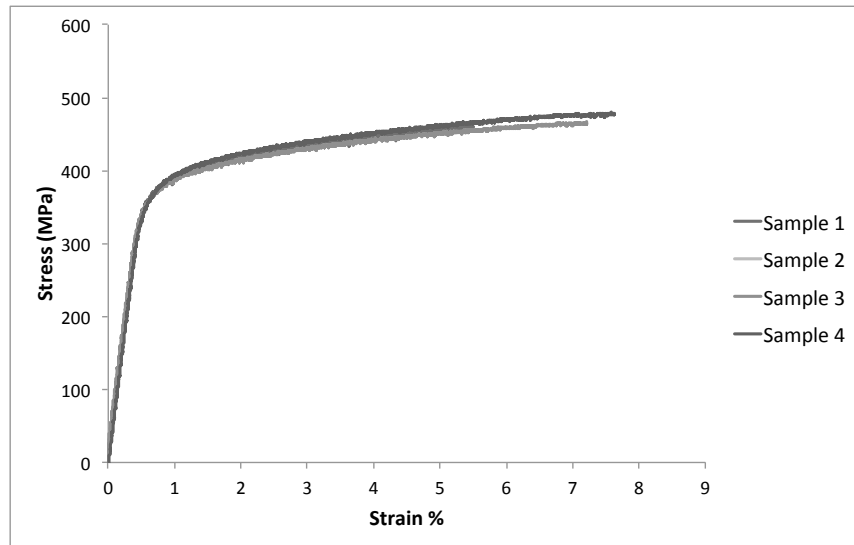


Figure 11-1 Tensile curves of the validation alloys: 15 min. at 120 °C + NA

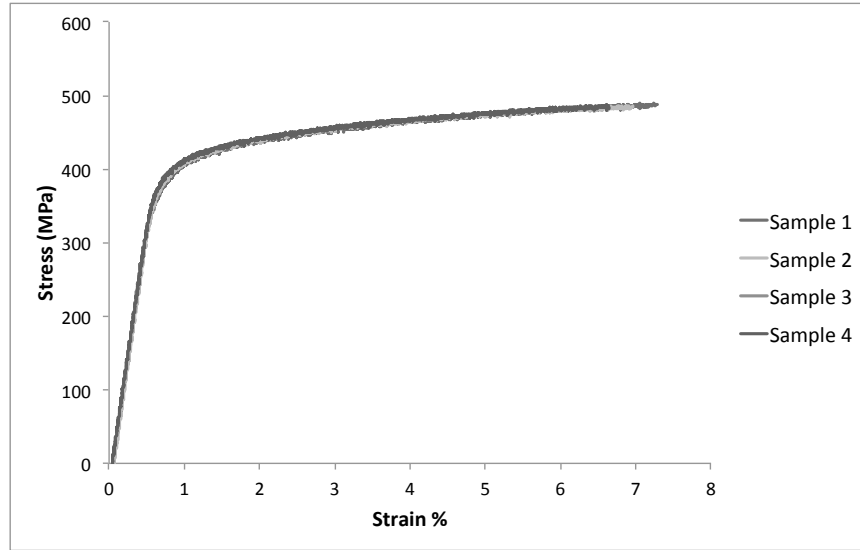


Figure 11-2 Tensile curves of the validation alloys: 1 h. at 120 °C + NA

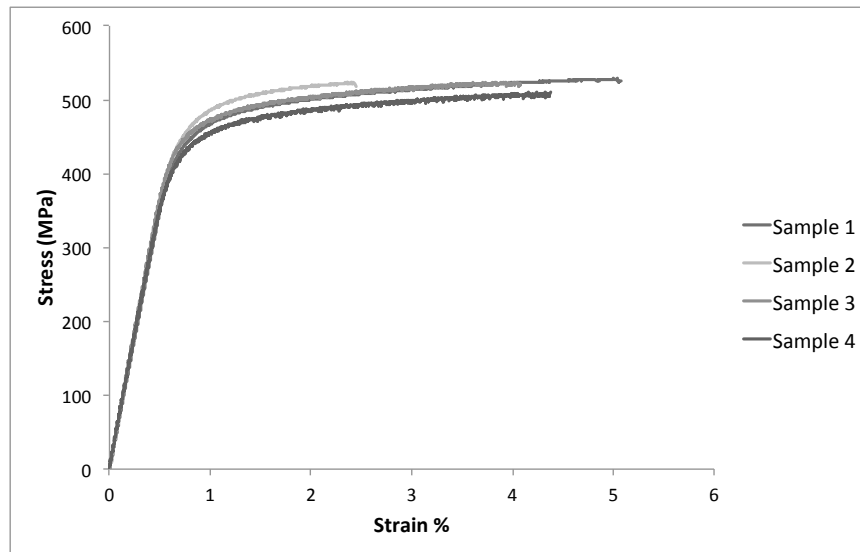


Figure 11-3 Tensile curves of the validation alloys: 12 h. at 120 °C + NA

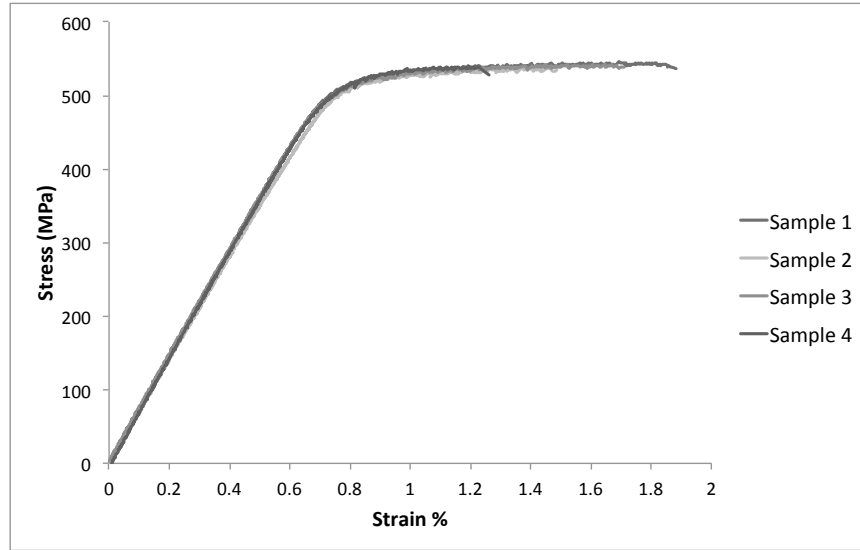


Figure 11-4 Tensile curves of the validation alloys: 24 h. at 120 °C + 5 h. at 180 °C + NA

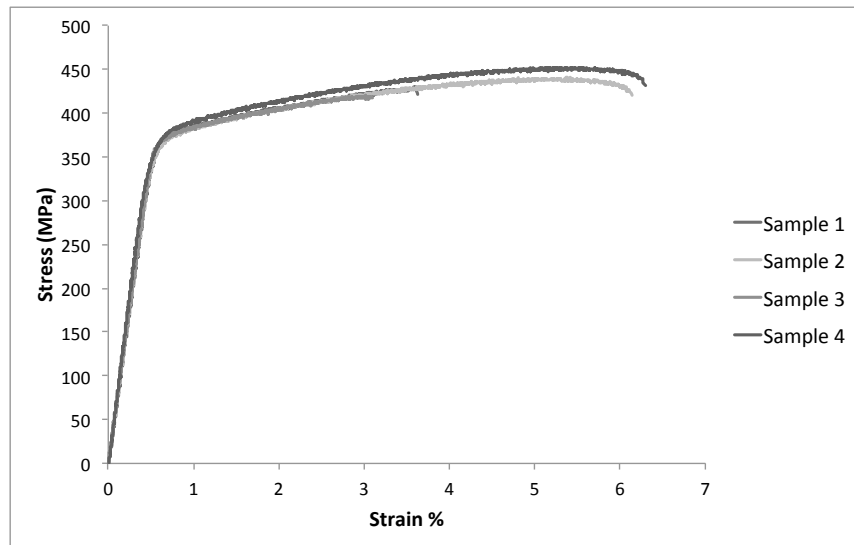


Figure 11-5 Tensile curves of the validation alloys: 24 h. at 120 °C + 30 h. at 180 °C + NA

12 References

- 1 S. Lin, A Study of Hot Tearing in Wrought Al Alloys, Master Thesis, 1999, Université du Québec à Chlcoutimi, Quebec.
- 2 S. Li, Hot tearing in cast aluminum alloys, PhD dissertation, 2010, Worcester polytechnic institute.
- 3 John Grandfield, D. G. Eskin, Ian Bainbridge, Direct-Chill Casting of Light Alloys: Science and Technology, Wiley-TMS, 2013.
- 4 D. Warrington, D. G. McCartney, Hot-Cracking in Al Alloys 7050 and 7010 – a Comparative Study, Cast Metals, 3(4) (1991) 202-208.
- 5 J.D. Robson, Microstructural evolution in Al alloy 7050 during processing, Materials Science and Engineering A, 382 (2004) 112–121.
- 6 X. M. Li, M. J. Starink, The Effect of Compositional Variations on the Characteristics of Coarse Intermetallic Particles in Overaged 7xxx Al Alloys, Materials Science and Technology, 17 (2001) 1324-1328.
- 7 C. Mondal, A.K. Mukhopadhyay, On the nature of T(Al₂Mg₃Zn₃) and S(Al₂CuMg) phases present in as-cast and annealed 7055 Al alloy, Materials Science and Engineering A, 391 (2005) 367–376.

8 L.F. Mondolfo, Aluminium Alloys: Structure and Properties, Butterworths, London, 1976, p. 842.

9 L. W. bin, P. Q. lin, Microstructural evolution of ultra-high strength Al-Zn-Cu-Mg-Zr alloy containing Sc during homogenization, Transaction of Nonferrous Metals Society of China, 21 (2011) 2127-2133.

10 E. Tillová, Structural analysis of heat treated automotive cast alloy, Journal of achievement in materials and manufacturing engineering, 47 (2011) 19-25.

11 U. A. Curle, Semi-solid rheocasting of grain refined Al alloy 7075, Transaction of Nonferrous Metal Society of China 20 (2010) 832-836.

12 B.L. Ou, J.G. Yang, M.Y. Wei, Effect of Homogenization and Aging Treatment on Mechanical Properties and Stress-Corrosion Cracking of 7050 Alloys, Metallurgical and Materials Transactions A, 38A (2007) 1760-1773.

13 C. Shi, J. Lai and X. Grant Chen, Microstructural Evolution and Dynamic Softening Mechanisms of Al-Zn-Mg-Cu Alloy during Hot Compressive Deformation, Materials, 7 (2014) 244-264.

14 W. Gaosong, Z. Zhihao, Effect of homogenizing treatment on microstructure and conductivity of 7075 Al alloy prepared by low frequency electromagnetic casting, China Foundry, 11 (2014) 39-44.

15 L. C. Mei, C. Z. Qian, Intermetallic phase formation and evolution during

homogenization and solution in Al-Zn-Mg-Cu alloys, *Science China*, 56 (2013) 2827–2838.

16 S.T. Lim, Y.Y. Lee, I.S. Eun, Microstructural Evolution during Ingot Preheat in 7xxx Aluminium Alloys for Thick Semiproduct Applications, *Materials Science Forum*, 519-521 (2006) 549–554.

17 A.R. Eivani, H. Ahmed, J. Zhou, and J. Duszczyk, Evolution of Grain Boundary Phases during the Homogenization of AA7020 Al Alloy, *Metallurgical and Materials Transactions A*, 40A (2009) 717-728.

18 S. R. Ghiaasiaan, Controlled diffusion solidification of 7xxx wrought alloys, PhD thesis, 2015, McMaster University, Hamilton, ON, Canada

19 C. Nowill, Investigation of the Quench and Heating Rate Sensitivities of Selected 7000 Series Al Alloys, Master thesis, 2007, WPI, NY, USA.

20 J. Buha, Secondary aging in an aluminium alloy 7050, *Materials Science and Engineering*, A 492 (2008) 1–10

21 L. K. Berg, GP-Zones in Al-Zn-Mg Alloys and Their Role in artificial aging, *Acta materialia*, 49 (2001) 3443–3451

22 P. Lejcek, Grain Boundary Segregation in Metals, 1st edition, Springer-Verlag Berlin Heidelberg, 2010.

23 D. Cristina, M. Hupalo, O. Cintho, Natural aging behavior of AA7050 Al alloy after

cryogenic rolling *Materials Science & Engineering A*, 593 (2014) 1–7

24 G. Sha, A. Cerezo, Early-stage precipitation in Al–Zn–Mg–Cu alloy (7050), *52* (2004) 4503–4516

25 L. Sobrin, Predictions of precipitation reaction mechanisms for 7xxx series Al alloys cast by CDS technique, Master Thesis, 2014, University of Windsor, Windsor, ON, Canada

26 A. Deschamps, Y. Bréchet, Influence of quench and heating rates on the aging response of an Al-Zn-Mg-(Zr) alloy, *Materials Science and Engineering A*, 251 (1998) 200-207.

27 L. Wu, M. Seyring, M. Rettenmayr and W. Wang, Characterization of precipitate evolution in an artificially aged Al-Zn-Mg-Sc-Zr alloy, *Materials Science and Engineering, A*, (2010) 1068-1073.

28 E. Sjolander and S. Seifeddine, The heat treatment of Al-Si-Cu-Mg casting alloys, *Journal of Materials Processing Technology*, 210 (2010) 1249-1259.

29 ZANG Jin-xin, ZHANG Kun, DAI Sheng-long, Precipitation behavior and properties of a new high strength Al–Zn–Mg–Cu alloy, *Trans. Nonferrous Met. Soc. China* 22(2012) 2638–2644.

30 Y. Li, L. Kovarik, High-resolution characterization of the precipitation behavior of an Al–Zn–Mg–Cu alloy, *Philosophical Magazine Letters*, 92 (2012) 166–178.

31 C. Chang, J. Yang, Optimization of Heat Treatment Parameters with the Taguchi Method for the A7050 Al Alloy, IACSIT International Journal of Engineering and Technology, 2 (2010) 269-272.

32 M. Easton, H. Wang, J. Grandfield, An Analysis of the Effect of Grain Refinement on the Hot Tearing of Al Alloys, Materials Science Forum, 28 (2004) 224-229.

33 M. Easton, J. Grandfield, The Effect of Grain Refinement and Cooling Rate on the Hot Tearing of Wrought Al Alloys, Materials Science Forum, 30 (2006) 1675-1680.

34 Dmitry G. Eskin, Physical Metallurgy of Direct Chill Casting of Aluminum Alloys, CRC Press; 1 edition, April 17, 2008.

35 Mark Easton, Cameron Davidson, David StJohn, Grain Morphology of As-Cast Wrought Aluminium Alloys, Proceedings of the 12th International Conference on Aluminium Alloys, Yokohama, Japan, September 5-9, 2010, 173-178

36 J. C. Lin, High strength, high stress corrosion cracking and castable Al-Zn-Mg-Cu-Zr alloys for shape cast product, US 20080066833 A1, 2008.